SIMULATION BASED ANALYSIS OF
THE MICRO PROPULSION WITH
ROTATING CORKSCREW MOTION OF FLAGELLA

by
MUSTAFA KOZ

Submitted to the Graduate School of Engineering and Natural Sciences
in partial fulfillment of
the requirements for the degree of
Master of Science

Sabanci University
August 2009

SIMULATION BASED ANALYSIS OF THE MICRO PROPULSION WITH ROTATING CORKSCREW MOTION OF FLAGELLA

APPROVED BY:

Dr. Serhat Yeşilyurt   ………………………….

(Thesis Supervisor)

Dr. Ali Koşar   ………………………….

Dr. Ayhan Bozkurt   ………………………….

Dr. Hasan Sait Ölmez   ………………………….

Dr. Volkan Patoğlu   ………………………….

DATE OF APPROVAL: 10/08/2009

SIMULATION BASED ANALYSIS OF
THE MICRO PROPULSION WITH
ROTATING CORKSCREW MOTION OF FLAGELLA

Mustafa Koz

EECS, MS Thesis, 2009

Thesis Supervisor: Serhat Yeşilyurt

ABSTRACT

In this work, a simulation based parametric analysis of a micro swimmer with a rotating helical tail is presented. The numeric model consists of micro swimmer positioned in a cylindrical micro channel. The flow induced by the rotating helical tail has a Reynolds number much smaller than 1 and it is solved by three dimensional, time dependent Navier Stokes equations subject to continuity. As a requirement of the changing orientation of the swimmer and its rotating helical tail in the micro channel, ALE description of the mesh is used in simulations. The obtained parametric results show the effect of input parameters; maximum amplitude, wavelength, length and rotation rate of the helical tail on the motion parameters, power requirement and power efficiency of the swimmer. The numeric results for swimming speeds are validated with the use of analytical predictions available in the literature. As another validation, the bacterium Vibrio Alginolyticus is modeled and the numeric results of it compared with the observational data available in the literature.

DÖNEN VİDA HAREKETİNE SAHİP KUYRUĞUN
YARATTIĞI MİKRO İTKİNİN
BENZETİM TABANLI PARAMETRİK ANALİZİ

Mustafa Koz

EECS, Yüksek Lisans Tezi, 2009

Tez Danışmanı: Serhat Yeşilyurt

Anahtar Kelimeler: Mikro yüzücü, mikro itki, dönen helis kuyruk, güç, verimlilik

ÖZET

Bu çalışmada, dönen helis kuyruk kullanan mikro yüzücünün benzetim tabanlı parametrik analizi sunulmuştur. Sayısal modeller mikro yüzücünün içine konumlandırıldığı silindirik bir mikro kanaldan oluşur. Dönen helis kuyruğun oluşturduğu akış 1'den çok daha küçük bir Reynolds sayısına sahiptir ve bu akış, üç boyutlu, zamana bağlı ve kütlenin korunuma dayanan Navier Stokes denklemleri ile çözülmüştür. Mikro kanal içinde yönü değişen yüzücünün ve onun dönen helis kuyruğunun bir gereksinimi olarak benzetimlerde biçimi bozulan örgü yöntemi kullanılmıştır.

Elde edilen parametrik sonuçlar, girdi değişkenleri olan, helis kuyruğun azami genliğinin, dalga boyunun, uzunluğunun ve dönme hızının yüzücünün hareket parametrelerine, güç gereksinimine ve güç verimliliğine olan etkisini ortaya koymuştur. Yüzme hızları için elde edilen sayısal sonuçlar literatürde mevcut olan analitik tahminler ile teyit edilmiştir. Diğer bir teyit ise Vibrio Alginolyticus bakteri modeline ait sayısal sonuçların, literatürde mevcut olan ve gözlemsel deneyler ile elde edilen sonuçlar ile karşılaştırılmasıyla gerçekleşmiştir.

"So, how do you go about teaching them something new? By mixing what they know with what they don't know. Then, what they see vaguely in their fog/something they recognize, they think 'Ah, I know that.' And then it's just one more step to, 'Ah, I know the whole thing.' And their mind thrusts forward into the unknown and they begin to recognize what they didn't know before and they increase their powers of understanding."

-Picasso, in *Life with Picasso* by Francoise Gilot and Carlton Lake (Nelson, London, 1965), p. 66

ACKNOWLEDGEMENTS

First of all, I would like to thank my thesis supervisor, Dr. Serhat Yeşilyurt for giving me the opportunity to work on a novel project continuously since my late senior year in B.Sc. His support and welcome to my new ideas to the project thought me to how to push my limits further and further. Hopefully, this thesis will not be the end of my journey in this subject but will propel me to the deeper grounds of it.

I also would to thank my thesis jury: Ali Koşar, Ayhan Bozkurt, Hasan Sait Ölmez and Volkan Patoğlu for enabling me to switch between disciplines and catch priceless details with their great support.

TABLE OF CONTENTS

LIST OF TABLES

LIST OF FIGURES

LIST OF SYMBOLS

Latin

A	Area
A	Drag coefficient
B	Amplitude function
C	Resistance Coefficient
D	Torque coefficient
F	Force vector
F	Force magnitude
I	Identity matrix
J	Rotational moment of inertia matrix
J	Rotational moment of inertia value
L	Length
M	Mass
Ms	Maximum mesh element size
P	Pressure
R	Transformation matrix
R	Radius of geometry
S	*Skew symmetric operator*
TR	Time ramp function
U, V, W	velocity vector components in body frame
U	Fluid velocity vector in body frame
X	Body frame, Stationary reference frame
X, Y, Z	Body frame - Stationary reference frame coordinates
$Xlim$	Micro channel geometric limits in the x axis.
Zn	Mesh Zone
f, f	Driving frequency
m	Sharpness coefficient of the geometric ramp function
n	Surface normal vector
n	Surface normal component magnitude
r	Radial distance
t	Time

u	Space velocity vector, ALE velocity vector
u, v, w	velocity vector components in space frame
x	Space frame, ALE frame
x, y, z	Coordinates in space frame, Coordinates in ALE frame

Greek

Δ	Difference quantity
Σ	Stress Tensor, Total quantity
Ω	Deforming domain
Π	Power
α	*The orientation angle of the swimmer in xy plane*
β	*The orientation angle of the swimmer in any plane perpendicular to xy plane*
δ	Dirac delta function
η	Efficiency
θ	Rotation angle
λ	Wave length
μ	Viscosity
ρ	Density
τ	Torque
ω	Angular rotation of swimmer

Subscripts

av	Time averaged quantity
app	Applied quantity
b	Swimmer body parameter
ch	Channel geometry
cyl	Cylinder parameter
cm	Center of mass
dm	Dummy
eff	Effective quantity
end	End point
in	Input

int	Initial value
longt	Longitudinal component
m	Mesh parameter
norm	Normal component
orient	A parameter specifically related with the orientation of the swimmer
out	Output
par	Partial contribution
rot	Rotational quantity
sd	Sub domain parameter
srf	Surface parameter
st	Start point
sw	Swimmer parameter
tl	Swimmer tail parameter
X, Y, Z	Coordinates in body frame
x, y, z	Coordinates in space frame
0	Maximum possible value

Number Groups

Re	Reynolds Number

LIST OF ABBREVIATIONS

ALE   Arbitrary Lagrangian Eulerian

CW   Clock Wise

CCW   Counter Clock Wise

DOF   Degrees Of Freedom

EGR   Element Growth Rate

MEMS   Micro Electro Mechanical System

ODE   Ordinary Differential Equations

PARDISO   Parallel Sparse Direct Linear Solver

SBT   Slender Body Theorem

RFT   Resistive Force Theorem

2D   Two Dimensional

3D   Three Dimensional

CHAPTER 1

INTRODUCTION

1.1   The Definition and Application Areas of a Micro Swimmer

A micro swimmer is designed to be a self-powered and self-propelling device with dimensions on the order of microns. The micro swimmer swims in vivo applications to reach areas that are currently inaccessible by catheters. It travels through blood vessels, the spinal canal, the urethra or the alimentary system [1]. However, a micro swimmer can only swim in stationary or low velocity bio fluids [2]. After reaching the desired region, the micro swimmer can perform clinical tasks by being minimally invasive to the environment it works in. Hence, the patient trauma due to clinical tasks can be reduced [2,3]. The intended clinical tasks can be exemplified as MIS, highly localized drug delivery, eye surgery, biopsy and screening for diseases, like cancer diagnosis, at their very early stages [1,2]. A complete list of the proposed applications is given below in Table 1.

Condition	Capability
Tumors	To treat tumors that cannot be accessed via conventional surgery, e.g. Deep in the brain
Arteriosclerosis	To remove fatty deposits from the walls of arteries
Arterial damage	To deliver a payload of an adhesive to the site of a damaged cranial artery
Blood clots	To break clots in to smaller pieces before they have a chance to break free and move to cause serious damage
Detached retina	Surgical repairs
Liver and kidney stones	Destruction of stones
Parasites	Destruction or removal of parasites
Others	Transmit images
	Delivery of drugs to specific locations
	In situ biosensing and diagnostics

Table 1: A list of intended applications of a micro robot [1]

The research on micro swimmers also leads the way to a research on rotary micro actuators [4] and with the use of it, biologically inspired micro pumps. The numerical works

[5,6] show that a rotating helical rod inside a micro channel can stand as an alternative to the previously available micro pump designs [7].

1.2   Application Examples

The macro scale biomimetic swimmer designs cannot be applied to micro scales because they make use of inertial forces instead of viscous forces. (The explanation of why a swimmer should make use of viscous forces in micro scale is given in Sec 1.4.1.) Therefore previous designs which are mostly fin driven [2], cannot be applied to micro scales [2].

Some designs propose the use of external magnetic fields to rotate a small ferromagnetic screw [2], an artificial micro swimmer as in Fig. 1 [1] or a real bacterium [8] inside the fluid. On the one hand, the main advantage of this design is having a continuous external power and not requiring a power controller. On the other hand, the main disadvantage is speed limitation [2].
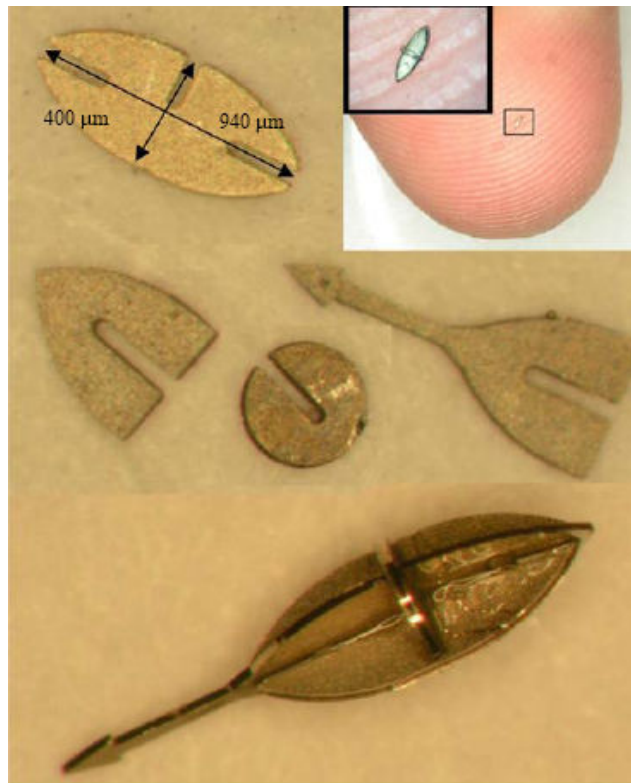
Figure 1: A micro robot by ETH, Zurich [1]

As an alternative to external powering presented above, there is an on board powering option which is still in the development process. A nano generator in Fig. 2 has been developed by Georgia Institute of Technology [1]. This nano generator converts the

mechanical energy available in the fluid into the electrical energy with the use of piezo electric, nano wires [1]. A prototype has generated 1 nA when it is excited with ultra sound [1]. According to the calculations of the developers of this design, nano generators with power densities of 4 W/cm^3 can be achieved [1].
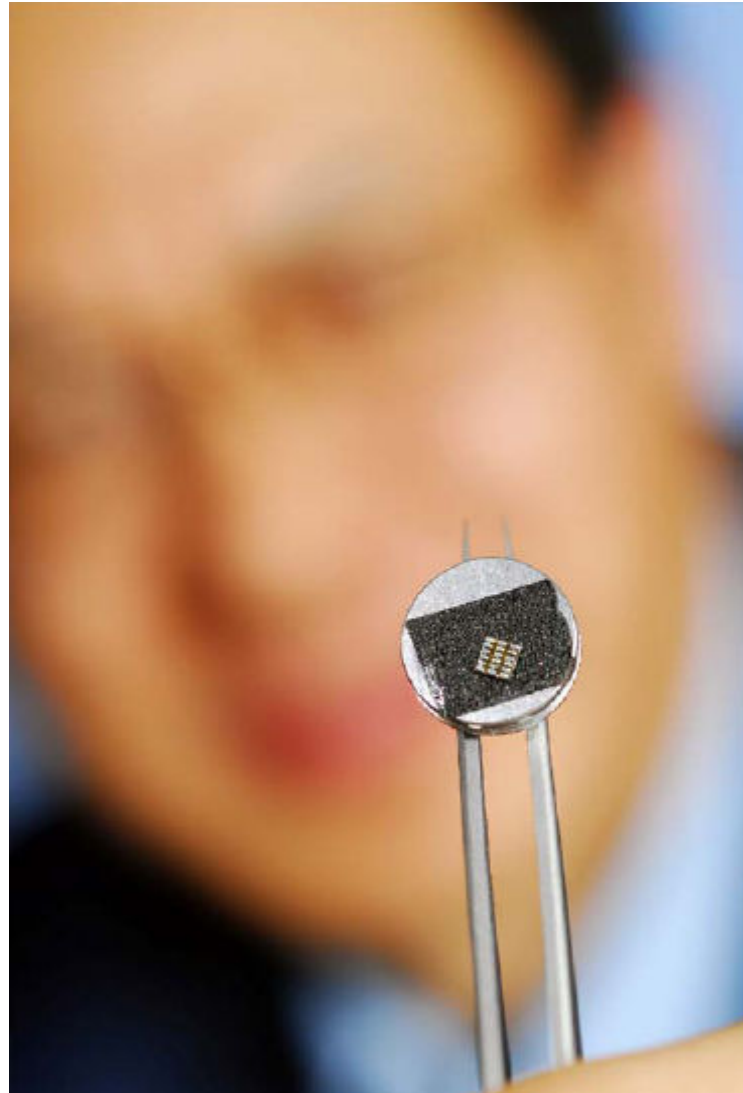
Figure 2: A nano generator developed by Georgia Institute of Technology [1]

A rotary micro actuator in Fig. 3 with sizes of a sand grain has been developed as a result of the collaboration between the Micro/Nanophysics Research Laboratory at Australia's Monash University and Carnegie Mellon University in the USA [1]. This motor is made of piezoelectric materials and actuated at ultrasonic frequencies [1]. The motor is designed to rotate a flagellum [1]. At the early stages of experiments, the flagellum will be made of human hair but will be replaced with Kevlar later [1]. The motor will either be powered via wireless transmission of energy or the storage of energy in super capacitors [1].
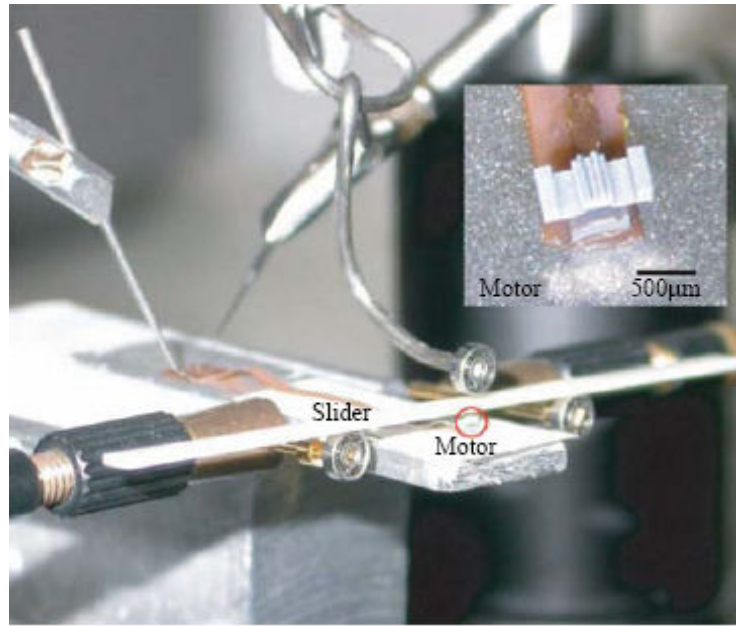
Figure 3: A micro rotary motor developed by Monash and Carnegie Mellon universities

1.3 Micro Organisms

1.3.1 Propulsion of Micro Organisms

The propulsion technique of a swimmer needs to be chosen according to the ratio of inertial forces to the viscous forces. The swimmer technique should rely on the dominating force type. In order to quantify the ratio, dimensionless Reynolds number is used:

$$\text{Re} = \frac{\rho v L}{\mu} \tag{1}$$

'ρ', 'v' and 'μ' are the density, mean velocity and dynamic viscosity of the fluid respectively. 'L' is the characteristic length that the fluid is going through or around. If Reynolds number is bigger than 1, this means that inertial forces are dominating the viscous forces. If it is smaller than 1, the domination is the other way around.

When viscous forces dominate inertial ones, the time dependent terms of Navier-Stokes equations can be omitted. Therefore, reciprocal motions of a swimmer, such as the opening and closing of the 'scallop' or flapping a fish's fin, become ineffective because of not being

able to create any net force [1, 3]. So, there is need of continuous relative motion between the swimmer and fluid to swim when Re<1.

This thesis focuses on the relative motion which is generated by a rotating helical tail with respect to a spherical body [9]. This rotary motion is rare in the nature and attracts the attention of biologists and engineers [4]. It is observed that prokaryotic bacteria have this kind of rotary motion at their flagella. Hence, the details of the prokaryotic bacteria are given in the next section and used as the originating base for numeric analysis.

1.3.2 An Overview to Micro Organisms

For Escherichia coli (E. coli) bacterium to swim, it is reported that it has up to six helical flagella which are left handed and almost rigid [2, 10, 11, 12]. Flagella are connected separate motors and they bundle when they rotate in counter-clockwise (CCW) direction as viewed from behind the cell. This is the "run" mode, that the cell moves steadily forward by being pushed from the behind [12, 13]. However, the flagella become separated in case of a rotation in clockwise (CW) direction [9, 12]. This is the "tumble" mode that results nearly no net displacement but an erratic movement of the cell for changing swimming direction [13]. In order to achieve a rotation in both directions, there is an embedded, reversible and rotary motor with 45 nm diameter, inside the cell wall [10,14]. The helical flagellum connected to the motor with a short proximal hook [13]. The flagellum has an approximate length of 10 μm, thickness of 20 nm, wavelength of 2.5 μm and amplitude of 0.5 μm [2, 10-14]. According to the experimental observation of Chatopadhyay, the helical flagellum length can vary from 3 μm to 6 μm [14]. The rotation frequency of it is on the order of 100 Hz and even surpasses the value of 1000 Hz with a power requirement on the order of 10^{-15} W. [10-14]. There is a linear decrease of the torque with the increasing rotation frequency [11]. Swimming speed and rotation rate are linearly related [11]. Moreover, when the motor rotates the flagellum (rotor) in one direction, the cell body (stator) rotates in opposite direction with a slower rate. This counter rotation of the cell body is observed to be about 10 Hz when the helical flagellum is tethered to a glass slide [9]. Lighthill stated that the counter rotation of cell body reduces the swimming speed [12]. The ellipsoid cell body has a much larger mass which is around 1 pico grams [10] and also, rotational inertia due to its approximate diameter and length of 1 μm and 2 μm respectively [10, 12]. The mentioned characteristic lengths and velocities corresponds to a Reynolds number about 10^{-4} which is small enough to neglect the time dependent terms in the Navier-Stokes equations. However, in order to be very accurate

about the motion of a micro organism, the Brownian motion should be taken into account [11, 12].

1.4 Objectives and Major Challenges of This Work

Building a micro robot is major challenge because of requiring different kinds of knowledge from various disciplines and technologies, such as silicon micro technology and MEMS nano technology and MEMS, micro-electronics, bioengineering, materials science, electromagnetism and hydrodynamics [1]. By the collaboration of the disciplines listed above, the following questions in Table 2 are tried being answered:

Power	How to power the robot
Propulsion	How to move it around the body
Steering and Location	How to control it and monitor its position
Insertion and Removal	How to introduce it into the body and remove or dispose of it when its job is done

Table 2: The major questions to build a micro robot [1]

This work tries to answer the "propulsion" question. Therefore, a "micro swimmer" is under the focus rather than a "micro robot". For answering the propulsion question, this work intends to reproduce the motion of a generic micro swimmer with simulations as close as possible to the reality. By this way, measurements which are challenging or even impossible in real life observations, can be done with simulations.

Currently, observations of micro organisms available in literature cannot currently provide the three dimensional (3D) trajectory. Moreover, precise and separate measurements for the rotation of a cell body and helical flagellum are very challenging with the equipments currently available for the researchers. Lastly, force and torque measurements on a micro organism cannot be taken with sensors but only can only be estimated with drag and torque coefficients which take swimming and rotation velocity as inputs.

By making use of numerical simulations, in addition to a 3D trajectory, all kinematic and dynamic parameters of a micro swimmer can be obtained as close to reality as possible. By obtaining these parameters, net power output of the motor and propulsive efficiency can be calculated.

In order to validate the accuracy of the numerical simulations, previous works available in the literature are used as a reference point to compare with and build on.

1.4.1 Propulsion

The propulsion of microorganisms in a viscous fluid with propagated bending waves is first proved by Sir Geoffrey Taylor [15]. However, this proof was only valid for the waves with small amplitudes which do not reflect the values from the real bacteria. Following Taylor, Hancock derived the mathematical formulation for the propulsion of sinusoidal propagated bending waves with amplitudes surpassing the limiting 1/3 value for the ratio between peak-to-peak amplitude to wavelength [16]. He achieved that by treating every small element of a thin filament as part a straight rod with a certain velocity. The longitudinal and normal components of the velocity are multiplied with the corresponding resistance constants which were driven empirically by Johnson and Brokaw by exploiting the linearity of Stokes equation [3]. Each force element on the small element is integrated for the whole filament. This net force should be balanced with the drag force created by the unknown swimming velocity. This velocity can be found by using the ratio of normal and longitudinal resistance coefficients which is 2 for an infinitesimally thin filament [17]. For a one-to-one comparison with a sea urchin spermatozoon, the sperm head is included in the calculations mentioned above. With the updated calculations, the resulting swimming velocity quite agreement with the value that Gray measured [17].

Lighthill and Dresdner reexamined the effect of radius and amplitude on resistance coefficients presented in the work of Gray and Hancock [17]. Their reexamination mostly changed the individual values of longitudinal and normal resistance coefficients while keeping their ratio almost constant [17].

The resistive force theory was first verified by a comparison with a sea urchin spermatozoon [1818]. However, its use was extended to organisms with helical flagella by Holwill and Burge [17]. Carlson first used the resistive force theory to find the energy required for a sperm cell to swim against a viscous fluid [17]. Later than Carlson, Brokaw put the resistive theory formulations in a simpler form to derive the sperm swimming speed and energy expenditure [17]. However, the required energy values calculated by Brokaw and Carlson were based on the longitudinal resistance coefficients originally proposed by Hancock and when these coefficients were updated by Lighthill and Dresdner in 1976 and 1980, the required energy values decreased 35% [17].

Resistive force theory can be applied for a fluid only perturbed by the infinitesimal thin filament but not by any other objects [17]. Therefore, resistive force theory can only be applied to bacteria with a single flagellum of which existence were observed by Robert and

Doyle [19] For this reason, if a flagellum with a small amplitude drags a large cell or multiple flagella rotate together, the resistive force theory cannot be applied. There are some numerical methods applied for finding out the bundling of multiple flagella [17].

As an alternative to resistive force theory, Lighthill's slender body theory [12] assumes a fluid flow going around a slender swimmer and calculates the resistive coefficients according to that. Childress proved Lighthill's slender body theorem for an infinitely long flagellum [20]

The trajectory of bacteria with a rotating single flagellum was analytically driven to be helical with small amplitude [21]. Publications based on simulations [19] and observations [22] also verified the analytical predictions of helical trajectory.

In the work of Brennen and Winet from 1977 [23], they stated that the former analytical solutions of RFT and SBT are based on (Re=0) assumption which neglects the small contribution of inertial effects. Therefore, they pointed out the possibility of visible inertial effects in the far field [23]. They have also given a review of slender body and resistive force theorem [23]. Moreover, they mentioned the effect of wall effects on slender body motions [23]. The major contribution of Brennen Winet, is the 2D observations which tabulate the details of micro organisms such as the cilia/flagella number, geometric properties and actuation frequencies [23].

In 1995, Magariyama two dimensionally observed the swimming of Vibrio alginolyticus cells [24]. These cells have single and helically shaped flagellum. They derived a roughly linear relation between swimming speed and flagellum rotation rate [24]. The ratio of swimming speed and flagellum rotation rate was presented as the slip rate which is an indirect demonstration of efficiency. Moreover, the motor torque characteristic of the cell was presented [24].

In 2001, Magariyama extended the scope of their previous work from 1995, by observing a cell called Salmonella typhimurium with multiple flagella [25].

In addition to Magariyama's work from 1995, a similar observation of Vibrio alginolyticus, has been made by Goto in 2001 [4]. Additionally, they made a boundary element analysis to predict the values obtained from observations numerically.

In 2005, Goto and co writers published a journal based on boundary element method to show the effect of boundaries on the swimming motion of a singly flagellated bacterium [31].

In the observational work of Chattopadhyay from 2006, they measured the force required the force to hold a swimming cell still, separate the angular velocities of the flagella

and cell body as a function of induced flow velocity [14]. They find a strong agreement with their results and resistive force theory [14].

In 2009, Chattopadhyay has extended their work published in 2006, by observing the swimming motion of single flagellated cells namely V. alginolyticus, C. crescentsus and E. coli minicell [26]. The observed swimming speed and rotation rates for the flagella and cell bodies are compared with analytical predictions of slender body and resistive force theorems [26].

1.4.2   Energy Requirement

A typical cell rotates its helical filament around 1000 Hz which corresponds to an energy requirement on the order of femto Watts [11]. This required energy is the value that is obtained as the net output from the motor and it can only be used with 1-3% efficiency to propel the cell. This efficiency range is predicted theoretically for a rigid helical coil and in the observational work of Chattopadhyay [14], propulsion efficiency for an E. coli cell is obtained to be 2%.

1.4.3   Mesh Issue

In the area of fluid dynamics, strong distortions in the continuum can occur in fluid-fluid or fluid-structure interactions. It is vital to choose a kinematical description of the continuum which can balance taking large deformations into account and keeping the resolution of the material interfaces as high as possible [27].

There are two conventional methods to describe the continuum kinematics which are namely the Lagrangian description and Eulerian description. This thesis uses a midway between these methods which is called arbitrary Lagrangian-Eulerian description (ALE). By using the ALE description, the strengths of two methods are tried to be combined while their weaknesses are tried to be eliminated.

In Lagrangian description, which is depicted in Fig. 4, each mesh node follows the initially associated material particle during its motion [27, 28]. This description is most suitable for structural mechanics [27, 28]. However, when large deformations occur, the Lagrangian description cannot provide high resolution at the interfaces without remeshing [27, 28].

Figure 4 shows that the Eulerian description lets a material particle to displace freely and at the same time, keeps the mesh nodes immobile [27, 28]. On the one hand, the strength of this description is the convenience of handling particles with large displacements without the need of remeshing [27, 28]. On the other hand, the precise tracking of material particles and so, the interfaces of materials cannot be achieved [27, 28].

In Figure 4, the ALE description, the mesh nodes can either exactly follow material particles as in the Lagrangian description, stay immobile as in the Eulerian description or follow the material particle to a certain extent [27, 28]. Hence, larger deformations of material particles can be handled than the Lagrangian description can [27, 28]. Moreover, the handled large deformations have more resolution than the Eulerian description can provide [27, 28].
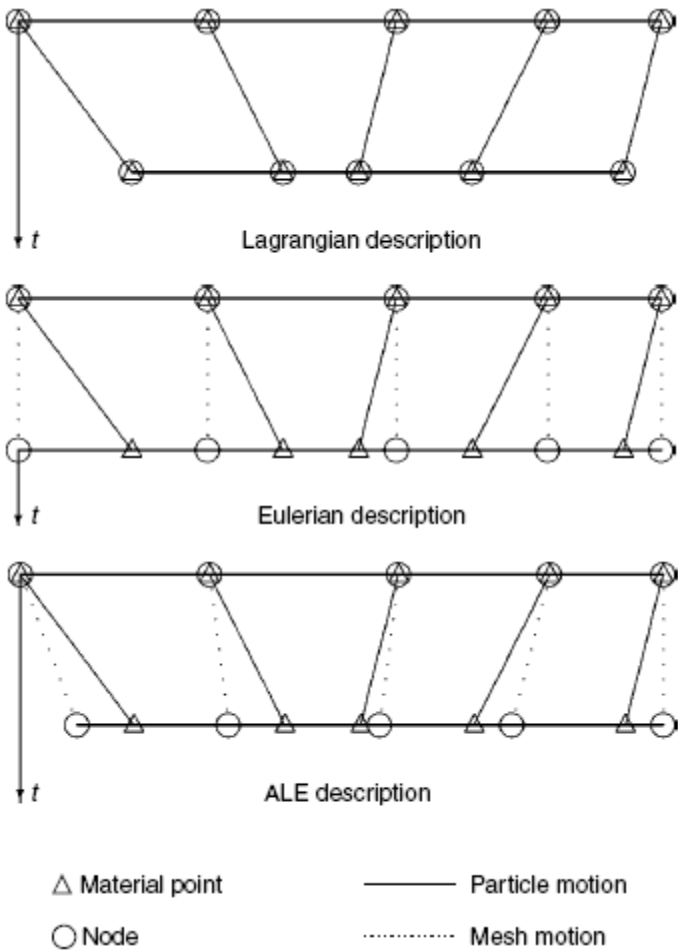
Figure 4: Application examples of Lagrangian, Eulerian and ALE descriptions [27]

1.5 The Originality of This Work

This work provides simulations of 3D motion of micro swimmers which are governed by Navier-Stokes equations. Therefore, the inertial effects at the far field [23] can affect the swimmer motion. Moreover, the 3D trajectory provides valuable insight to the 2D observations. Hence, a concept micro swimmer can be developed with maneuvering capability. Additionally, once the simulations are proved to be correct with respect to observations, than assumptions and simplifications can be made more efficiently.

CHAPTER 2

METHODOLOGY

2.1 Rigid Body Motion of the Micro Swimmer

2.1.1 Frames

There are two frames used in the models. They are named as body and space frames. Both frames are depicted in Fig. 5 with the micro channel and micro swimmer. The space frame is expressed with x coordinates and fixed where middle point of the micro channel longitudinal axis is. The x axis of the space frame coincides with the longitudinal axis of the micro channel. The body frame is expressed with X coordinates and it is fixed to the axes intersection of the ellipsoid micro swimmer body. Moreover, the X axis of the body frame is aligned with the longitudinal axis of the micro swimmer helical tail as depicted in Fig 6666.
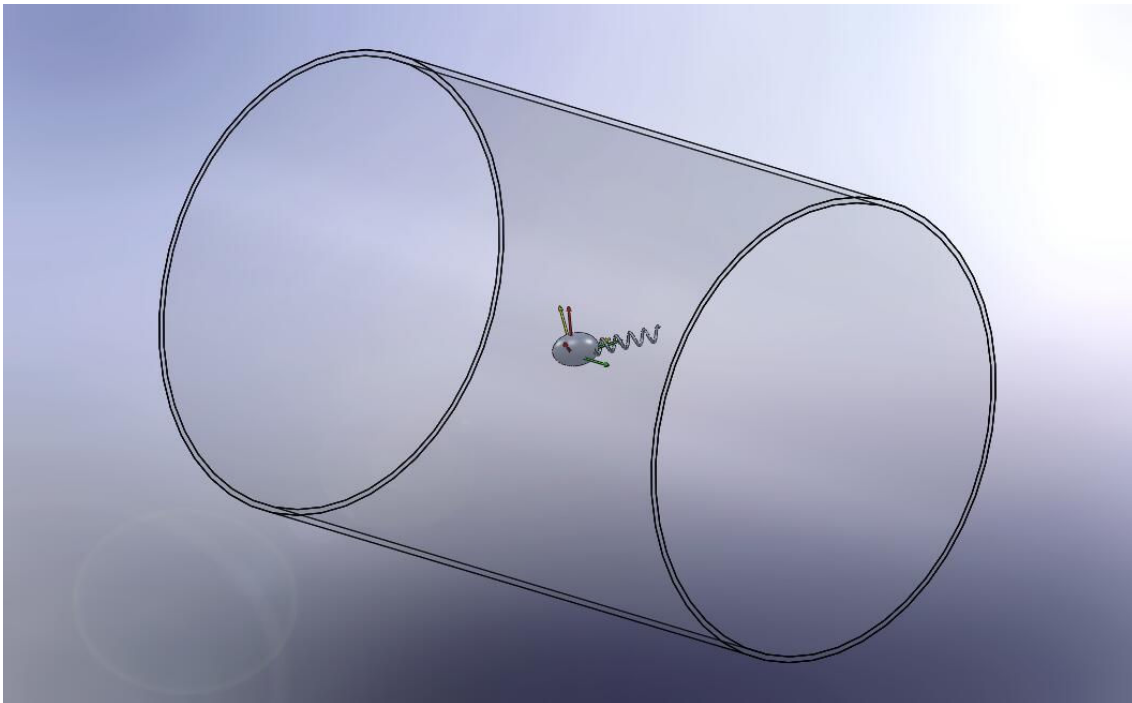
Figure 5: Micro channel with space and body frames.

The body frame only rotates with respect to the space frame. The orientation of micro swimmer is expressed with α and β angles as seen in Figure 6,7 and 8. At the initial condition,

α and β angles are 0 and 90 degrees respectively. In this initial condition, all axes of space and body frames are aligned. Hence, the transformation matrices from space to body $\mathbf{R}_X^x$ and body to space $\mathbf{R}_x^X$ are identity matrices at the initial condition.

$$\mathbf{R}_X^x(0) = \mathbf{R}_x^X(0) = \begin{bmatrix} 1 & 0 & 0 \\ 0 & 1 & 0 \\ 0 & 0 & 1 \end{bmatrix} \tag{2}$$

As the simulation runs, the transformation matrix is updated according to the formulas below [29,30]:

$$\dot{\mathbf{R}} = S\big(\boldsymbol{\omega}(t)\big)\mathbf{R}(t) \tag{3}$$

$$S(\boldsymbol{\omega}) = \begin{bmatrix} 0 & -\omega(1) & \omega(2) \\ \omega(1) & 0 & -\omega(3) \\ -\omega(2) & \omega(3) & 0 \end{bmatrix} \tag{4}$$

Due to the fact that COMSOL cannot perform matrix inversions, $\mathbf{R}_x^X$ and $\mathbf{R}_X^x$ matrices are calculated individually. The lengthy matrix multiplications result the following matrices to be time integrated in the next step.

$$\dot{\mathbf{R}}_x^X(t) = \begin{bmatrix} \mathbf{R}_x^X(1,2)\omega_z - \mathbf{R}_x^X(1,3)\omega_y & \mathbf{R}_x^X(1,3)\omega_x - \mathbf{R}_x^X(1,1)\omega_z & \mathbf{R}_x^X(1,1)\omega_y - \mathbf{R}_x^X(1,2)\omega_x \\ \mathbf{R}_x^X(2,2)\omega_z - \mathbf{R}_x^X(2,3)\omega_y & \mathbf{R}_x^X(2,3)\omega_x - \mathbf{R}_x^X(2,1)\omega_z & \mathbf{R}_x^X(2,1)\omega_y - \mathbf{R}_x^X(2,2)\omega_x \\ \mathbf{R}_x^X(3,2)\omega_z - \mathbf{R}_x^X(3,3)\omega_y & \mathbf{R}_x^X(3,3)\omega_x - \mathbf{R}_x^X(3,1)\omega_z & \mathbf{R}_x^X(3,1)\omega_y - \mathbf{R}_x^X(3,2)\omega_x \end{bmatrix} \tag{5}$$

$$\dot{\mathbf{R}}_X^x(t) = \begin{bmatrix} \mathbf{R}_X^x(1,2)\omega_Z - \mathbf{R}_X^x(1,3)\omega_Y & \mathbf{R}_X^x(1,3)\omega_X - \mathbf{R}_X^x(1,1)\omega_Z & \mathbf{R}_X^x(1,1)\omega_Y - \mathbf{R}_X^x(1,2)\omega_X \\ \mathbf{R}_X^x(2,2)\omega_Z - \mathbf{R}_X^x(2,3)\omega_Y & \mathbf{R}_X^x(2,3)\omega_X - \mathbf{R}_X^x(2,1)\omega_Z & \mathbf{R}_X^x(2,1)\omega_Y - \mathbf{R}_X^x(2,2)\omega_X \\ \mathbf{R}_X^x(3,2)\omega_Z - \mathbf{R}_X^x(3,3)\omega_Y & \mathbf{R}_X^x(3,3)\omega_X - \mathbf{R}_X^x(3,1)\omega_Z & \mathbf{R}_X^x(3,1)\omega_Y - \mathbf{R}_X^x(3,2)\omega_X \end{bmatrix} \tag{6}$$

Their time integrals give the final transformation matrices:

$$\mathbf{R}_x^X(t) = \int_{t=0}^{t} \dot{\mathbf{R}}_x^X dt \tag{7}$$

$$\mathbf{R}_X^x(t) = \int_{t=0}^{t} \dot{\mathbf{R}}_X^x dt \tag{8}$$

However, the applied method for obtaining the transformation matrices has a weakness. Since all terms of the transformation matrix are time integrated, there is a possibility of numeric error accumulation which may not enforce an orthogonal transformation matrix.

Direct transformations between space and body frames can be done by using 3x3 rotation matrices.

$$\begin{bmatrix} x \\ y \\ z \end{bmatrix} = \mathbf{R}_x^X \begin{bmatrix} X \\ Y \\ Z \end{bmatrix} \tag{9}$$

$$\begin{bmatrix} X \\ Y \\ Z \end{bmatrix} = \mathbf{R}_X^x \begin{bmatrix} x \\ y \\ z \end{bmatrix} \tag{10}$$
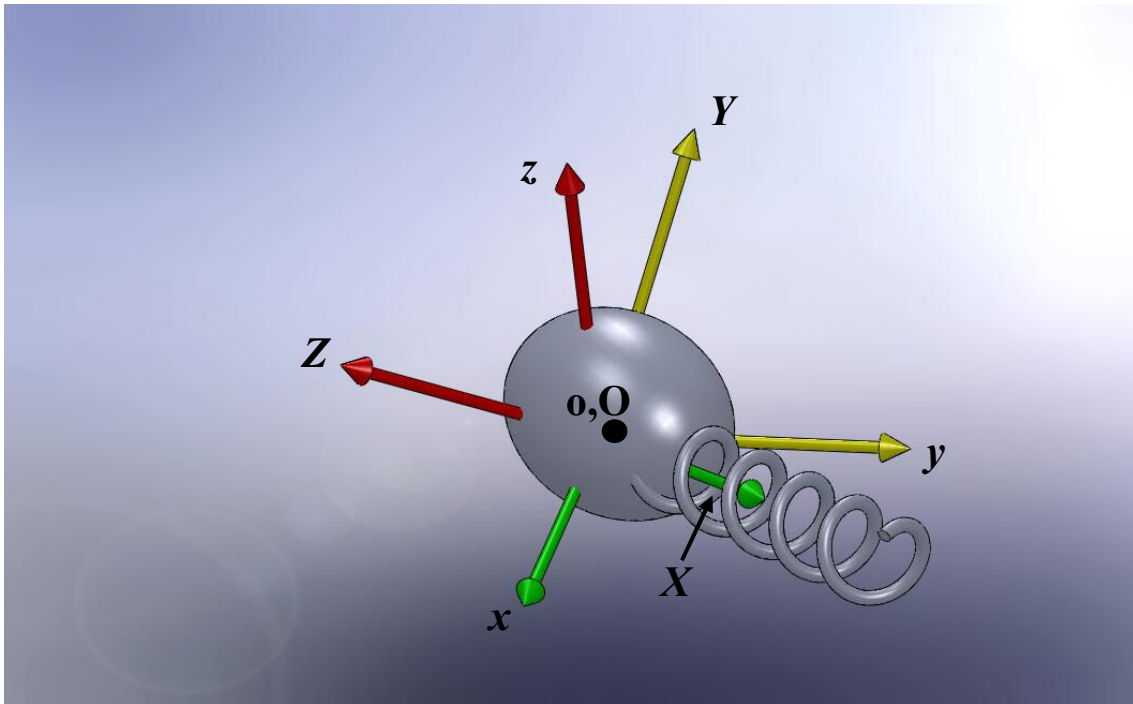
Figure 6: Trimetric view of micro swimmer with space and body frames.
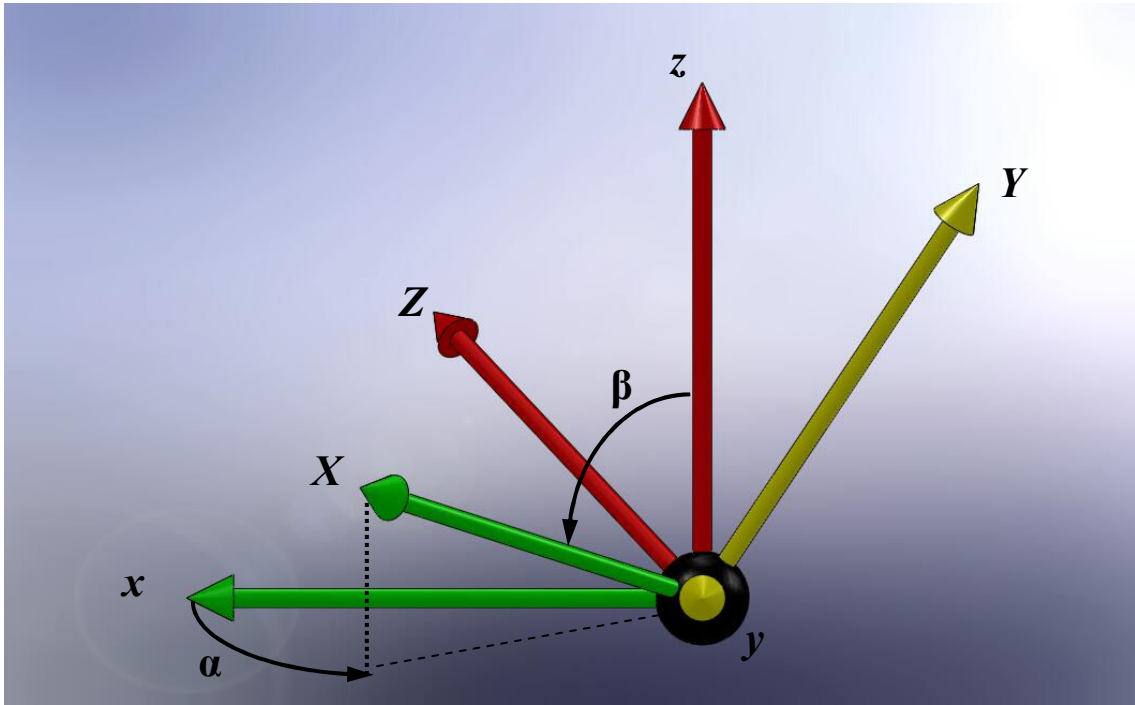
Figure 7: Side view of space and body frames.
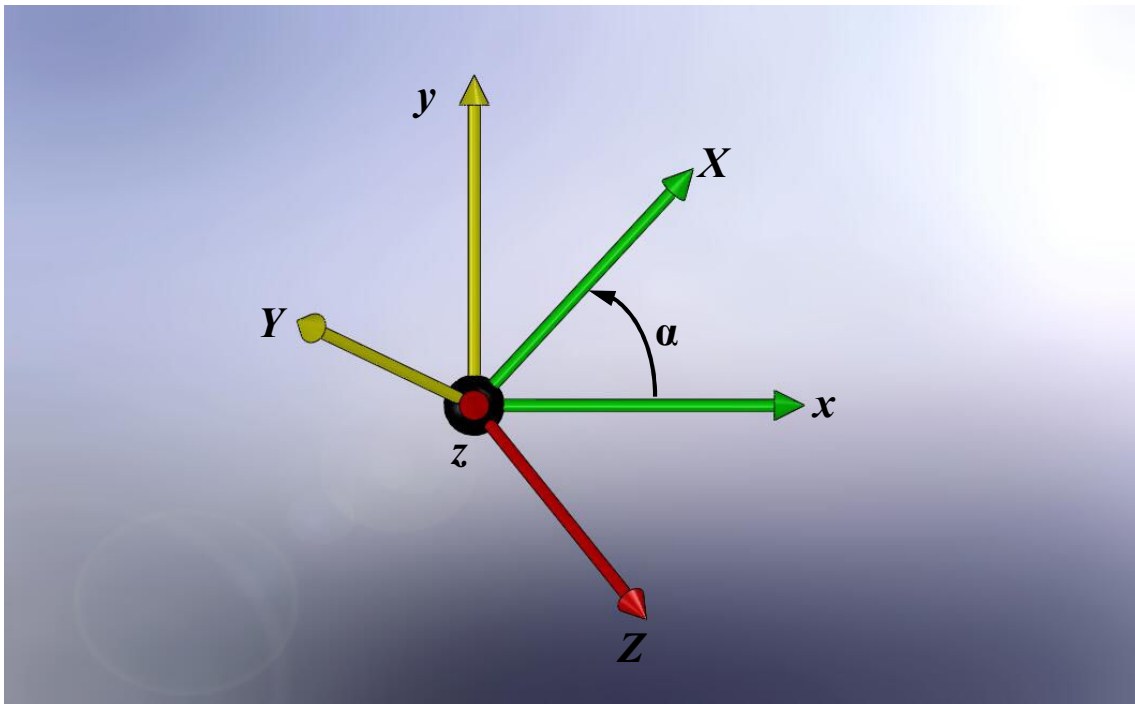
Figure 8: Top view of space and body frames.
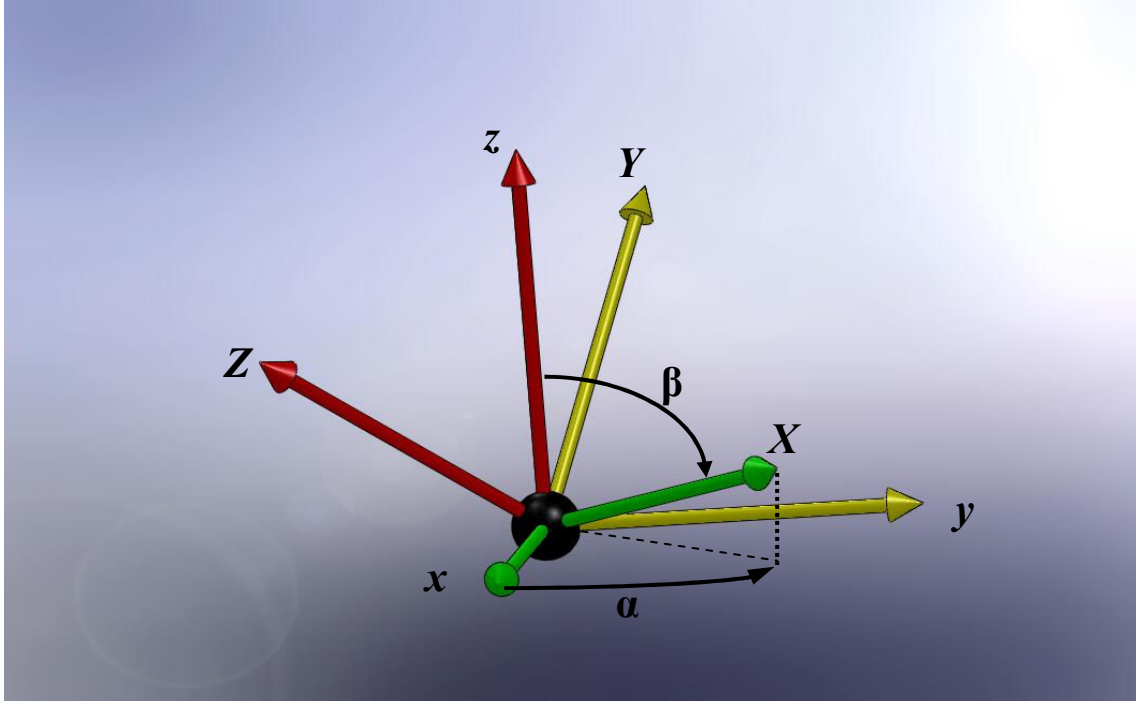
Figure 9: Trimetric view of space and body frames

2.1.2   Geometric Properties

In Figures 10, 11 and 12, it is demonstrated that all modeled micro swimmers in this work are positioned in the same cylindrical micro channel with a radius of 10 microns and a length of 60 microns. The smaller cylinder in the micro channel is a dummy sub domain used for numerical purposes which will be explained in detail in the Section 2.4.2.

The micro swimmer in Fig. 13 consists of an ellipsoid body and a helical tail. The ellipsoid body has a major axis length of L_b and two equal minor axis lengths of R_b. The helix tail has maximum amplitude of B_0, radius of R_{tl} and a wavelength of λ. The longitudinal axis length of the helix tail is L_{tl} and this value corresponds to a total helix length, l_{tl}:

$$l_{tl} = \sqrt{B^2 + \left(\frac{\lambda}{2\pi}\right)^2} \frac{2\pi L_{tl}}{\lambda} \tag{11}$$

For the modeling of Vibrio Alginolyticus (V. Alginolyticus) bacterium and an arbitrary micro swimmer with variable dimensions, there are two different drawings used in this thesis. All dimensional and physical constants for each drawing are presented in Table 3 and 4.

Vibrio alginolyticus			
L_b	4.6 μm	$Xlim_0$	-30 μm
R_b	0.35 μm	$Xlim_1$	-3 μm
R_{tl}	0.016 μm	$Xlim_2$	7 μm
$R_{ch,dm,cyl}$	2.5 μm	$Xlim_3$	30 μm
$L_{ch,dm,cyl}$	10 μm	M_{sw}	1.178 pg
R_{ch}	10 μm	ρ	1000 kg/m^3
L_{ch}	60 μm	μ	0,001 Pa.s

Table 3: Geometric and physical properties of the objects and fluid used in V.

alginolyticus model.

Parametric Swimmer			
L_b	2 μm	$Xlim_0$	-30 μm
R_b	0.5 μm	$Xlim_1$	-2 μm
R_{tl}	0.05 μm	$Xlim_2$	4 μm
$R_{ch,dm,cyl}$	2.5 μm	$Xlim_3$	3 μm
$L_{ch,dm,cyl}$	6 μm	M_{sw}	1.035 pg
R_{ch}	10 μm	ρ	1000 kg/m^3
L_{ch}	60 μm	μ	0,001 Pa.s

Table 4: Geometric and physical properties of the objects and fluid used in parametric

swimmer models.
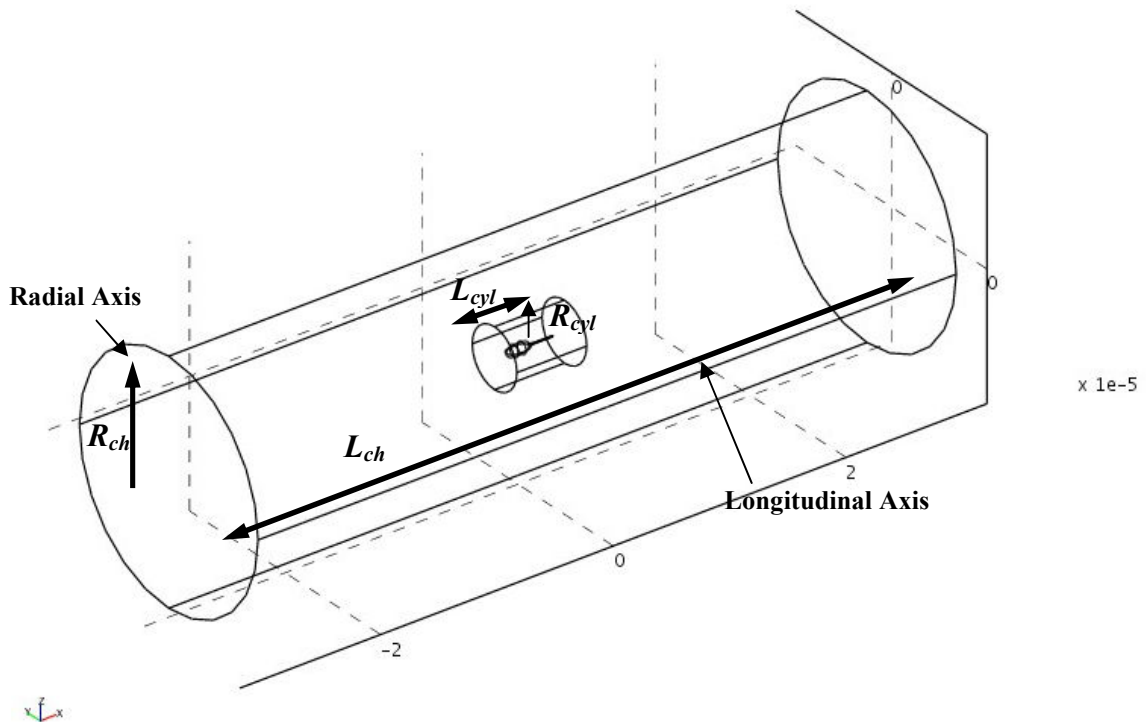
Figure 10: Trimetric view of micro channel and swimmer with parametric dimensions
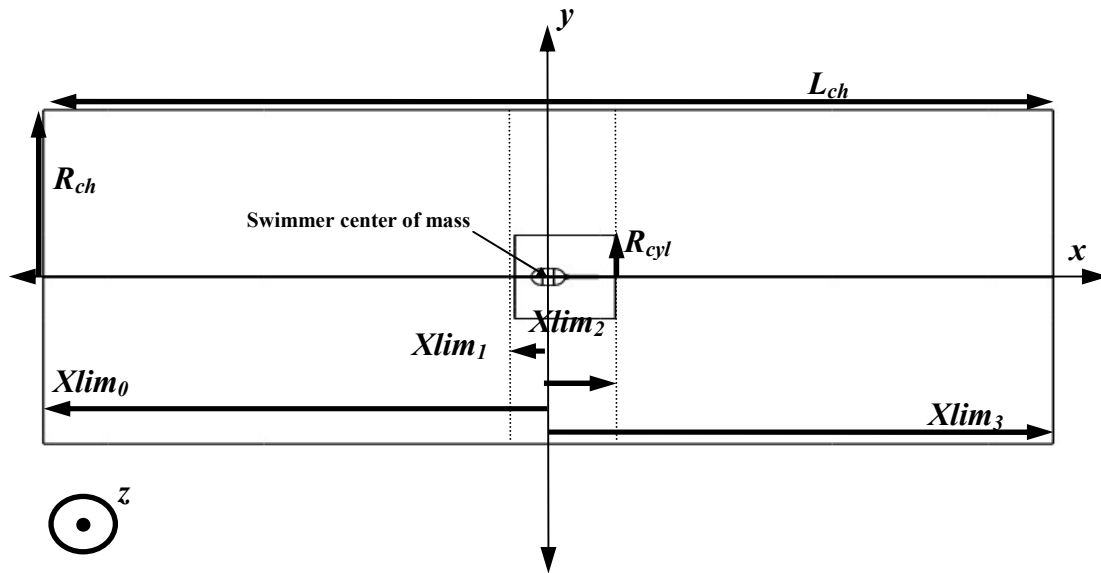
Figure 11: Side view of micro channel and swimmer with parametric dimensions
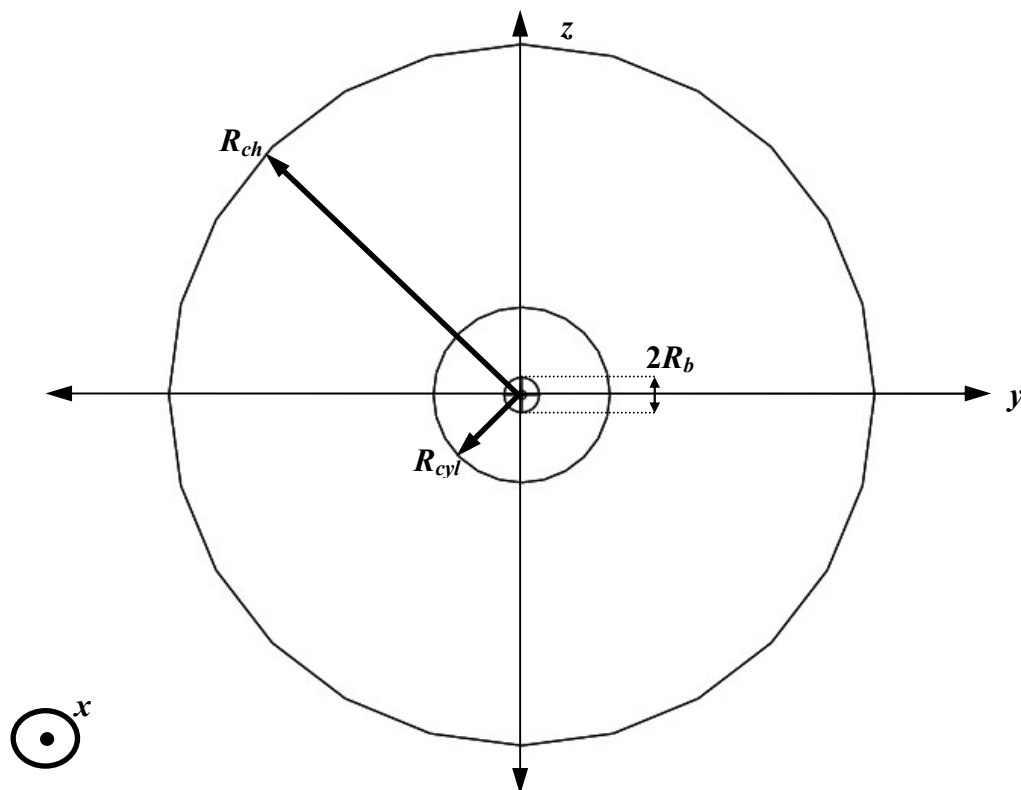
Figure 12: Cross section view of micro channel and swimmer with parametric dimensions
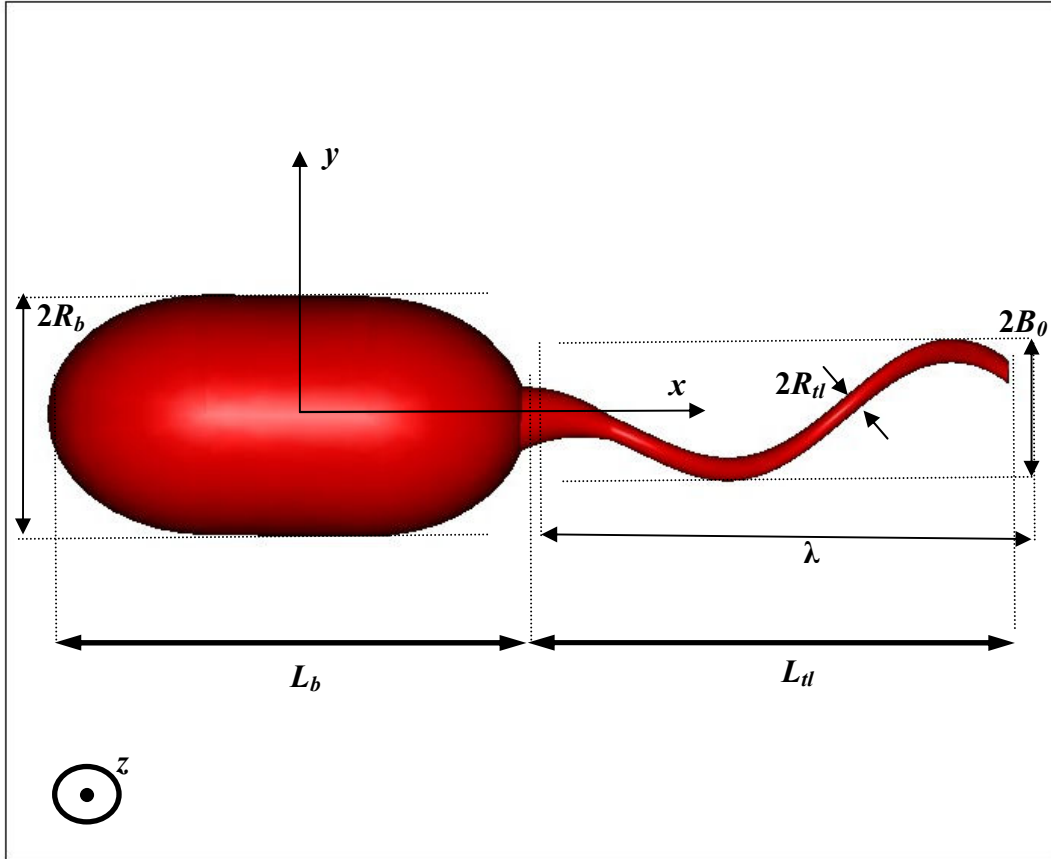
Figure 13: Side view of micro swimmer with parametric dimensions

2.1.3 Mass and Rotational Inertia

In all mass and rotational inertia (moment of inertia) calculations, the homogenous mass density (ρ) of the micro swimmer is taken the same with water which is the fluid used in the micro channel. So, the micro swimmer becomes neutrally buoyant and buoyancy effects are excluded from the equations of motion.

The mass ratio between the swimmer body and helix tail is high enough $M_b / M_{tl} \cong 66$ for the reference parametric swimmer (Reference parametric swimmer will be explained in detail in Section 2.5) to allow the assumption of swimmer body center of mass can represent the whole swimmer center of mass. The details of the mass and volume calculations of the body and the tail separately are given in appendix.

In addition to mass calculation, mass density of the micro swimmer is used in the calculations of micro swimmer rotational inertia in the body frame. The four calculated values are: the rotational inertia of body, $J_{X,b}$ and tail, $J_{X,tl}$ separately, in the X axis; and the full rotational inertia matrix of the whole swimmer, $\boldsymbol{J_{sw}}$. It is critical to know that the rotational inertia values are calculated in the body frame. The details and the validation of the inertia calculations; and the inertia matrices for all swimmers used in this work are given in Appendix A.

2.1.4 Forces

The software package, COMSOL calculates stress tensors, $\sum_x$, $\sum_y$ and $\sum_z$ as in Eq. 12. They are reaction forces per area on the fluid applied by the swimmer surface. Therefore, in the equations of motion their signs will be used accordingly. For a point on swimmer surface, the surface normal vectors are denoted with n_x, n_y and n_z vector magnitudes. Moreover, these stress tensors are calculated in space frame with input parameters: dynamic viscosity (μ), fluid velocity (u, v and w) and pressure (P) which are again calculated in the same frame (The verifications of these statements above are given in Appendix B).

$$
\begin{bmatrix} \Sigma_x \\ \Sigma_y \\ \Sigma_z \end{bmatrix} = \begin{bmatrix} \left(2\mu\dfrac{\delta u}{\delta x}-P\right)n_x + \mu\left(\dfrac{\delta v}{\delta x}+\dfrac{\delta u}{\delta y}\right)n_y + \mu\left(\dfrac{\delta w}{\delta x}+\dfrac{\delta u}{\delta z}\right)n_z \\ \mu\left(\dfrac{\delta v}{\delta x}+\dfrac{\delta u}{\delta y}\right)n_x + \left(2\mu\dfrac{\delta v}{\delta y}-P\right)n_y + \mu\left(\dfrac{\delta v}{\delta z}+\dfrac{\delta w}{\delta y}\right)n_z \\ \mu\left(\dfrac{\delta u}{\delta z}+\dfrac{\delta w}{\delta x}\right)n_x + \mu\left(\dfrac{\delta v}{\delta z}+\dfrac{\delta w}{\delta y}\right)n_y + \left(2\mu\dfrac{\delta w}{\delta z}-P\right)n_z \end{bmatrix} \tag{12}
$$

The stress tensors can also be mapped to body frame for rotational acceleration calculations because of having rotational inertia values defined in body frame. The transformation of the stress tensors from space frame to body frame is achieved with the use of $\mathbf{R_X^x}$ matrix as written in Eq 13.

$$
\begin{bmatrix} \Sigma_X & \Sigma_Y & \Sigma_Z \end{bmatrix}' = \mathbf{R_X^x}\begin{bmatrix} \Sigma_x & \Sigma_y & \Sigma_z \end{bmatrix}' \tag{13}
$$

2.1.5 Translational Motion of the Micro Swimmer

Swimmer body center of mass $x_{cm}(t)$, which will be referred as the "position of the micro swimmer", is initially located at the middle point of the micro channel longitudinal axis as it is seen in Fig 11. The swimmer has no initial velocity or acceleration in any direction.

$$\begin{bmatrix} \mathbf{x}_{cm}(0) \\ \dot{\mathbf{x}}_{cm}(0) \\ \ddot{\mathbf{x}}_{cm}(0) \end{bmatrix} = \begin{bmatrix} 0 \\ 0 \\ 0 \end{bmatrix} \tag{14}$$

For the fact that the translational motion of the swimmer is expressed in the space frame, the net forces on the micro swimmer are calculated by integrating the related stress tensors expressed space frame over the whole swimmer surface. Then, the translational acceleration vector is found by using the net forces.

$$\mathbf{F_x} = \begin{bmatrix} F_x & F_y & F_z \end{bmatrix}' = \begin{bmatrix} \int\limits_{A=A_{sw}} \Sigma_x dA & \int\limits_{A=A_{sw}} \Sigma_y dA & \int\limits_{A=A_{sw}} \Sigma_z dA \end{bmatrix}' \tag{15}$$

$$\dot{\mathbf{u}}_{cm} = -\mathbf{F_x} / M_{sw} \tag{16}$$

Translational accelerations are time integrated to obtain the velocity and position in the space frame. A 2D depiction of the terms used in the equations is presented in Fig 14.

$$\mathbf{u}_{cm}(t) = \dot{\mathbf{x}}_{cm}(t) = \begin{bmatrix} u_{cm}(t) & v_{cm}(t) & w_{cm}(t) \end{bmatrix}' \tag{17}$$

$$\mathbf{x}_{cm}(t) = \begin{bmatrix} x_{cm}(t) & y_{cm}(t) & z_{cm}(t) \end{bmatrix}' \tag{18}$$
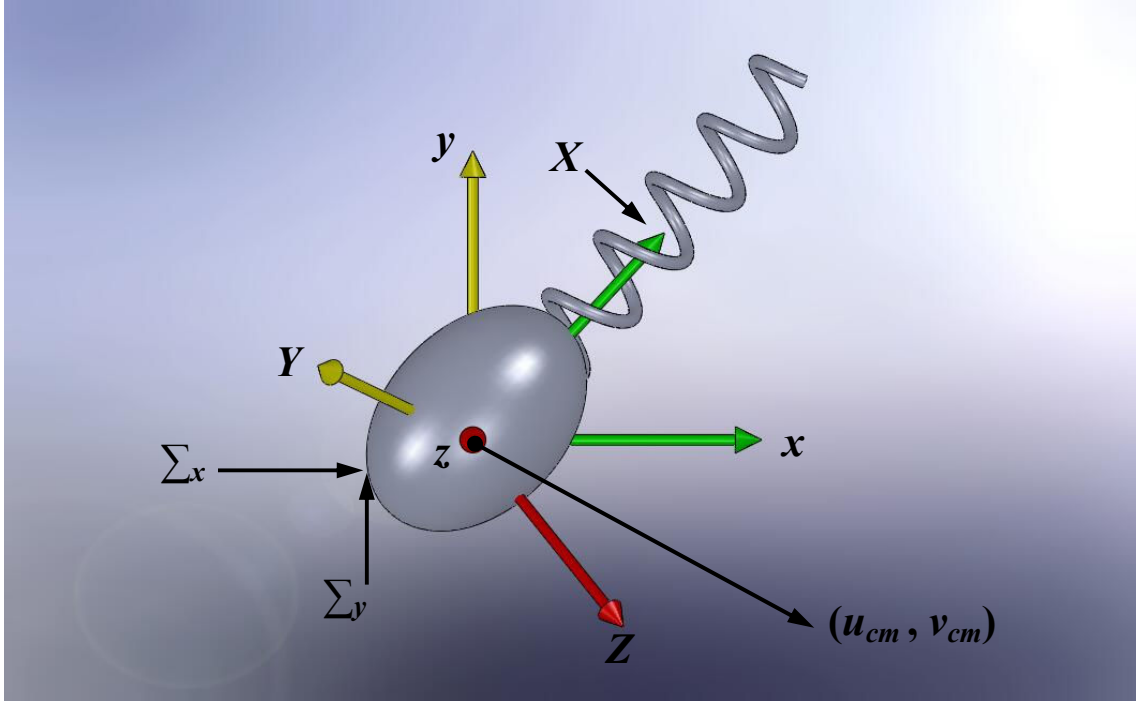
Figure 14: A 2D example of translational motion calculation.

2.1.6 Rotational Motion of the Micro Swimmer

The rotational motion of the swimmer can be calculated by first, finding the rotational acceleration. The rotational velocity and acceleration of the swimmer in space and body frames are initially zero.

$$\begin{bmatrix} \boldsymbol{\omega}_{\mathbf{X}} \\ \dot{\boldsymbol{\omega}}_{\mathbf{X}} \end{bmatrix} = \begin{bmatrix} 0 \\ 0 \end{bmatrix} \tag{19}$$

$$\boldsymbol{\omega}_{\mathbf{X}}(t) = \begin{bmatrix} \omega_X(t) & \omega_Y(t) & \omega_Z(t) \end{bmatrix}' \tag{20}$$

$$\begin{bmatrix} \boldsymbol{\omega}_{\mathbf{x}} \\ \dot{\boldsymbol{\omega}}_{\mathbf{x}} \end{bmatrix} = \begin{bmatrix} 0 \\ 0 \end{bmatrix} \tag{21}$$

$$\boldsymbol{\omega}_{\mathbf{x}}(t) = \begin{bmatrix} \omega_x(t) & \omega_y(t) & \omega_z(t) \end{bmatrix}' \tag{22}$$

In Figure 15, the rotational velocity of the micro swimmer body is depicted with ω_X. The applied rotational velocity of the swimmer tail relative to the head is denoted with ω_{app}. This value can be interpreted as the rotation frequency of an imaginary motor of which stator

is connected to the swimmer body and rotor is connected to the swimmer tail. The ω_X and ω_{app} sum give the rotation of the tail relative to the working fluid, ω_{eff}.
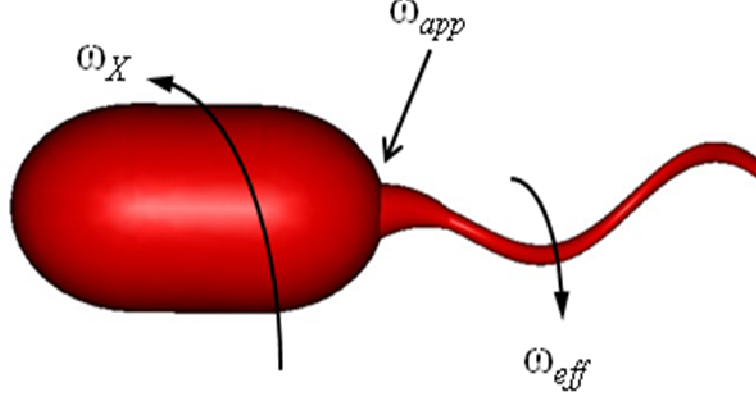
Figure 15: The body, motor and tail rotation of the micro swimmer.

For finding the rotational acceleration of the swimmer, the net torque values should be calculated on body frame in order to use the constant rotational inertia values which were calculated on the body frame. So firstly, the stress tensors mapped to the body frame (Eq. 13) and position coordinates in the body frame needs (Eq. 10) to be used.

Each stress tensor is multiplied with the corresponding position vector for a point on the swimmer surface and then, this multiplication is integrated on the whole swimmer surface giving the net torques in the body frame:

$$
\boldsymbol{\tau_X} = \begin{bmatrix} \tau_X & \tau_Y & \tau_Z \end{bmatrix}' = \begin{bmatrix} \displaystyle\int_{A=A_{sw}} [\Sigma_Z Y - \Sigma_Y Z]dA \\ \displaystyle\int_{A=A_{sw}} [\Sigma_X Z - \Sigma_Z X]dA \\ \displaystyle\int_{A=A_{sw}} [\Sigma_Y X - \Sigma_X Y]dA \end{bmatrix} \tag{23}
$$

The net torque is the only parameter for rotational accelerations in Y and Z direction. However, for the rotational acceleration of the swimmer body in the X direction, rotational momentum of the swimmer is another parameter which needs to be conserved. If there were no fluidic forces, the rotational acceleration of the swimmer body would be:

$$\dot{\omega}_{app}J_{X,tl} = \dot{\omega}_X J_{X,b} \Rightarrow \dot{\omega}_X = \frac{\dot{\omega}_{app}J_{X,tl}}{J_{X,b}} \tag{24}$$

When the fluid torque is put in the equation, the full rotational acceleration vector becomes:

$$\begin{bmatrix} \dot{\omega}_X \\ \dot{\omega}_Y \\ \dot{\omega}_Z \end{bmatrix} = \begin{bmatrix} \dot{\omega}_{app}J_{X,tl} \Big/ J_{X,b} \\ 0 \\ 0 \end{bmatrix} + \tau_{\mathbf{X}} \mathbf{J}_{\mathbf{X},sw}^{-1} \tag{25}$$

The rotational accelerations given in Eq. 25 are calculated in the body frame. However, the ODE (Ordinary Differential Equations) module of the COMSOL starts to integrate numerical values from the initial orientation of the micro swimmer when body frame is aligned with space frame. Afterwards, all body axes on the swimmer change orientation due to the rotational motion of the micro swimmer. Therefore, the calculated rotational accelerations should be transformed into the space frame for integration.

$$\dot{\boldsymbol{\omega}}_{\mathbf{x}} = \mathbf{R}_{\mathbf{x}}^{\mathbf{X}} \dot{\boldsymbol{\omega}}_{\mathbf{X}} \tag{26}$$

$$\boldsymbol{\omega}_{\mathbf{x}} = \int \dot{\boldsymbol{\omega}}_{\mathbf{x}} dt \tag{27}$$

The angular velocities in the space frame can also be expressed in the body frame as in Eq. 28:

$$\boldsymbol{\omega}_{\mathbf{X}} = \mathbf{R}_{\mathbf{X}}^{\mathbf{x}} \boldsymbol{\omega}_{\mathbf{x}} \tag{28}$$

With the use of $\boldsymbol{\omega}_{\mathbf{x}}$ and $\boldsymbol{\omega}_{\mathbf{X}}$ vectors, $\mathbf{R}_{\mathbf{X}}^{\mathbf{x}}$ and $\mathbf{R}_{\mathbf{x}}^{\mathbf{X}}$ transformation matrices and so, the body frame orientation with respect to space frame is updated by using the Equations 5-8. However, updating the micro swimmer mesh nodes will be presented in the Section 2.4.4.

2.1.7 Actuation & Rotation of the Helical Tail

The motion of the micro swimmer is actuated by its rotating helical tail. Therefore, the velocity induced on the tail due to its rotation needs to be formulated. The partial velocity of a point on the rotating helical tail boundary is calculated by taking the time derivative of the helix position formula. The helix position formula deforms a straight rod into a helix form by introducing displacements. The initial coordinates of the straight rod is given below:

$$\mathbf{X}_{tl}(0) = \left[X \quad r_{tl} \frac{Y_{tl}}{\left(Y_{tl,srf}^2 + Z_{tl,srf}^2\right)} \quad r_{tl} \frac{Z_{tl}}{\left(Y_{tl,srf}^2 + Z_{tl,srf}^2\right)} \right]' \tag{29}$$

As in the Eq. 30 each point, at an instant, on the same cross section of the straight rod perpendicular to its longitudinal axis is subjected to the same magnitude and direction of deformation. However, deformations only vary along the longitudinal axis and with time.

$$\mathbf{dX}_{tl} = \begin{bmatrix} 0 \\ B(X)Tr(t)\cos(\omega_{app}t + \theta_X - \dfrac{2\pi(X - X_{tl,st})}{\lambda}) \\ B(X)Tr(t)\sin(\omega_{app}t + \theta_X - \dfrac{2\pi(X - X_{tl,st})}{\lambda}) \end{bmatrix} \tag{30}$$

As Turner, Ryu and Berg reported in their work, there is a proximal hook connecting the helical tail and cell body together [1313]. Moreover, this hook is reported to be relatively short according to the tail length. However, there is no specific detail available in the literature for the length of the proximal hook. In this work, the proximal hook is modeled with function $B(X)$. It is specified along the helix tail and a geometric ramp function which is an exponential bridge by imposing zero displacement condition at the tail-swimmer body intersection; and the maximum displacement condition at the tip of the tail. The sharpness of the function can be adjusted by the m coefficient.

$$B(X) = B_0 \exp\left(\frac{-((X - X_{tl,st}) - X_{tl,end})}{mL_{tl}} \right) \tag{31}$$

The helix tail amplitudes in the experimental works available in the literature are effective values which directly affect bacteria swimming speeds. Due to the fact that $B(X)$ function output value decreases as the calculated point gets closer to the tail and body

intersection. Moreover, the function steepness with respect to X axis is not high enough to assume that the effective amplitude value equals to the maximum amplitude value. Therefore, according to the $B(X)$ function, an effective amplitude value, B_{eff} is calculated.

$$B_{eff} = \frac{\int\limits_{X=X_{tl,st}}^{X_{tl,end}} B_{tl}(X)dX}{L_{tl}} = B_0 \frac{\int\limits_{X_{tl,st}}^{X_{tl,end}} \exp\left(\frac{-(X-X_{tl,end})}{mL_{tl}}\right)dX}{L_{tl}}$$

$$= B_0 \frac{L_{tl} - L_{tl}m + L_{tl}me^{\left(\frac{-1}{m}\right)}}{L_{tl}} = B_0\left(1 - m + me^{\left(\frac{-1}{m}\right)}\right) \tag{32}$$

The $Tr(t)$ function is a time-dependent time ramp function which has a linearly increasing output in duration of $1/\omega_{app}$ seconds from 0 to 1. After one period, $1/\omega_{app}$ seconds, is completed the function constantly give output value 1. This ramp function lets the accelerations in the model increase continuously instead of sudden jumps.

$$Tr(t) = \begin{cases} (t \leq \omega_{app}^{-1}) & t\omega_{app} \\ t > \omega_{app}^{-1} & 1 \end{cases} \tag{33}$$

In result, the deformations added to the initial coordinates of the straight rod deform the original cylindrical shape into the helix shape rotating with respect to time.

$$\mathbf{X}_{tl} = \mathbf{X}_{tl,int} + \mathbf{dX}_{tl} \tag{34}$$

In order to derive the partial velocity contribution of the rotating helical tail, time derivative of $\mathbf{X}_{tl}$ is taken.

$$\mathbf{U}_{par}\left(\mathbf{X}_{tl}, t\right) = \mathbf{U}_{par,tl}\left(\mathbf{X}, t\right) = (\omega_X + \omega_{app})B(X)\begin{bmatrix} 0 \\ -\sin\left(\omega_{app}t + \theta_X - \frac{2\pi(X-X_{tl,st})}{\lambda}\right) \\ \cos\left(\omega_{app}t + \theta_X - \frac{2\pi(X-X_{tl,st})}{\lambda}\right) \end{bmatrix} \tag{35}$$

2.2 Motion of the Fluid Surrounding the Micro Swimmer

2.2.1 Navier-Stokes Equations

The micro channel is filled with water of which constant physical properties are given in Tables 3 and 4. The 3D, isothermal and time-dependent fluid domain is governed by the modified Navier-Stokes equation which is subjected to continuity.

$$\rho\left(\frac{\partial \mathbf{U}}{\partial t} + (\mathbf{U} - \mathbf{u}_m) \cdot \nabla \mathbf{U}\right) = -\nabla P + \mu \nabla^2 \mathbf{U} \;\; \text{in} \;\; \Omega(t) \tag{36}$$

$$\nabla \cdot \mathbf{U} = 0 \;\; \text{in} \;\; \Omega(t) \tag{37}$$

Equation 36 is distinguished from the original Navier-Stokes equation by the term $\mathbf{u}_m$ which is the velocity of the Arbitrary-Lagrangian Eulerian (ALE) deformation of the fluid domain. In Eq. 38 the mathematical definition of $\mathbf{u}_m$ is given as the time derivative of the time-dependent fluid domain position. ALE concept was explained in details in Section 1.4.3.

$$\mathbf{u}_m(\mathbf{x}_{\Omega(t)}, t) \equiv \frac{d\mathbf{x}_{\Omega(t)}}{dt}\bigg|_{\Omega(0)} \tag{38}$$

2.2.2 Boundary Conditions

According to $\alpha(0)$ and $\beta(0)$ angles, the initial orientation and so, the major swimming axis of the micro swimmer corresponds to the longitudinal axis of the cylindrical channel. This fact and the micro channel circular cross section, as shown in Fig. 12, minimize the channel boundary effects on the micro swimmer. According to the numeric work of Goto etal [31], the swimmer should swim from a distance to boundary with approximately 10 times the diameter of the cell not to be affected by the boundary. When the boundary distance to swimmer diameter ratios of the swimmers in Tables 3 and 4 are compared with the criteria put forward by the Goto etal [31], their magnitudes are under the critical value and they are sufficiently symmetric to simulate a swimming trajectory as if the simulation is run in a fluid domain with no boundaries.

In Figure 16, the channel inlet and outlet are specified as zero pressure and in Figure 17, the rest of the channel walls have no-slip boundary condition.
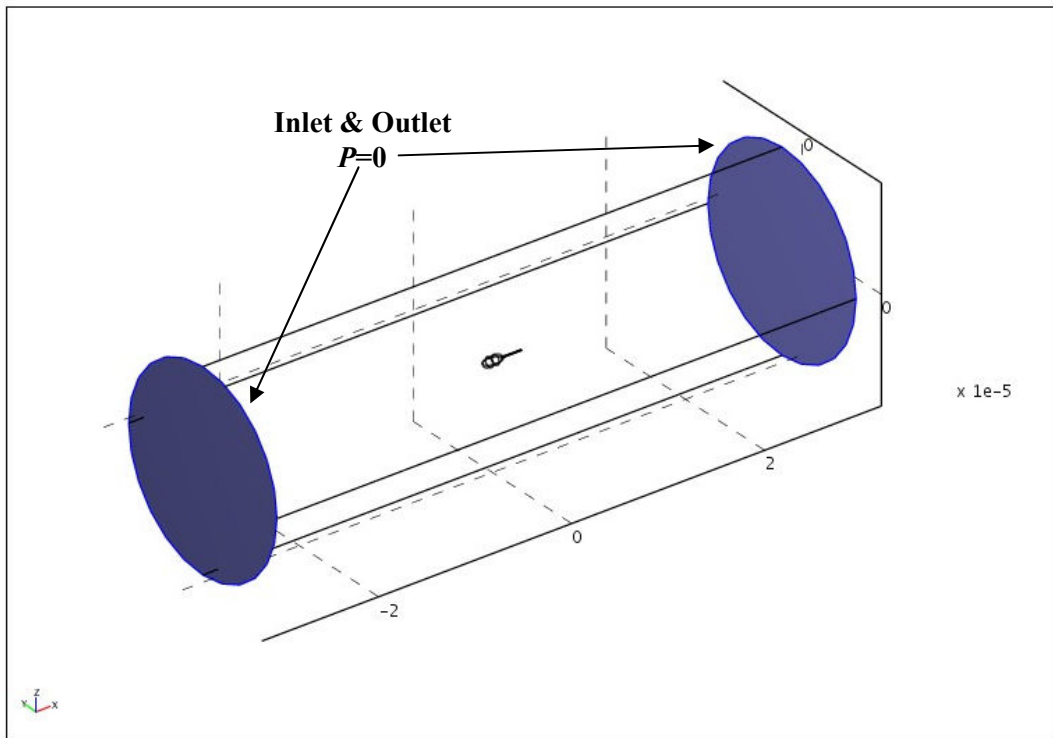
Figure 16: The specification of boundary conditions on micro channel inlet and outlet.
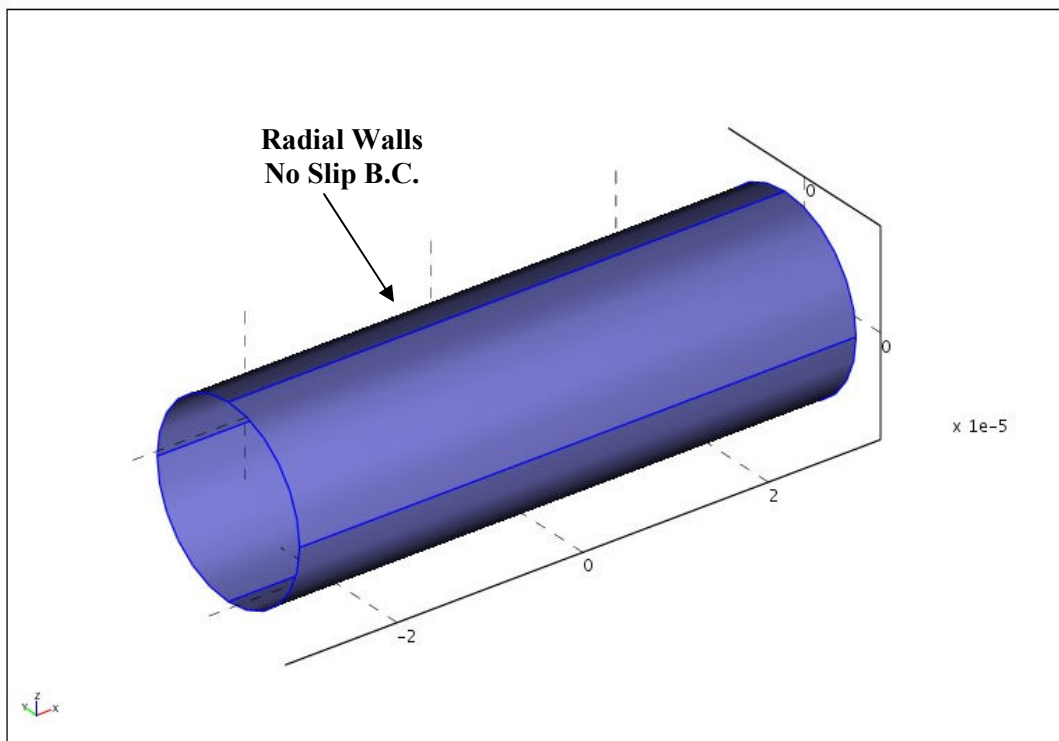
Figure 17: The specification of boundary conditions on micro channel radial walls.

The micro swimmer will translate and rotate according to the equations of motion. Translational velocity of the swimmer center of mass can be directly added to the velocity of any point on the swimmer. However, rotational velocities need to be expressed as linear velocity vectors on the moving and no-slip boundaries of the micro swimmer. In addition to the linear velocities defined on the micro swimmer boundaries due to the rigid body motion, the tail boundaries will need to include the rotating helical tail velocities.

In order to specify linear surface velocities on the swimmer, the radial position vectors on all three coordinate planes in the body frame need to be defined beforehand. The radial positions are named according to the perpendicular axis going through the related plane.

$$r_X = \sqrt{Y^2 + Z^2}, \; r_Y = \sqrt{X^2 + Z^2} \text{ and } r_Z = \sqrt{X^2 + Y^2} \tag{39}$$

For any point on the swimmer body, the partial linear boundary velocity induced by the rotational velocity in the X axis becomes:

$$\mathbf{U}_{par}\left(\mathbf{X}_b, t\right) = \mathbf{U}_{par,b}\left(X, t\right) = \omega_X r_X \begin{bmatrix} 0 \\ -(Z/r_X) \\ (Y/r_X) \end{bmatrix} \tag{40}$$

Moreover, the rotations of the body in Y and Z axes induce boundary velocities not only on the tail but on the whole swimmer surface. For any point on the swimmer surface, linear velocities induced by the swimmer rotation in the Y and Z axes are defined by:

$$\mathbf{U}_{par}\left(\mathbf{X}_{sw}, t\right) = \mathbf{U}_{par,sw}\left(X, t\right) = \omega_Y(r_Y) \begin{bmatrix} (Z/r_Y) \\ 0 \\ -(X/r_Y) \end{bmatrix} + \omega_Z(r_Z) \begin{bmatrix} -(Y/r_Z) \\ (X/r_Z) \\ 0 \end{bmatrix} \tag{41}$$

However, all the boundary velocities above are specified in body frame and in COMSOL settings, boundary velocities are specified in space frame. The verification of the COMSOL boundary velocity settings are presented in Appendix C. Hence, boundary velocities in body frame need to be expressed to space frame. For any point on the swimmer, the boundary velocity in space frame is calculated with the use of $\mathbf{R_x^X}$ matrix:

$$[u \quad v \quad w]' = \mathbf{R_x^X}[U \quad V \quad W]' \tag{42}$$

So the linear velocity on the swimmer body and tail becomes:

$$\begin{bmatrix} u_b \\ v_b \\ w_b \end{bmatrix} = \mathbf{R}_1^2 \left(\mathbf{U}_{par,sw} + \mathbf{U}_{par,b} \right) + \mathbf{u}_{cm} = \begin{bmatrix} u_{par,b} + u_{par,sw} + u_{cm} \\ v_{par,b} + v_{par,sw} + v_{cm} \\ w_{par,b} + w_{par,sw} + w_{cm} \end{bmatrix} \tag{43}$$

$$\begin{bmatrix} u_{tl} \\ v_{tl} \\ w_{tl} \end{bmatrix} = \mathbf{R}_x^X \left(\mathbf{U}_{par,sw} + \mathbf{U}_{par,tl} \right) + \mathbf{u}_{cm} = \begin{bmatrix} u_{par,tl} + u_{par,sw} + u_{cm} \\ v_{par,tl} + v_{par,sw} + v_{cm} \\ w_{par,tl} + w_{par,sw} + w_{cm} \end{bmatrix} \tag{44}$$

2.3 Post Processing

In addition to swimming motion, the micro swimmers in this work are also analyzed with their power requirements and power efficiency values.

2.3.1 Power Requirement

The time averaged power input, $|{<}\Pi_{in}{>}|$ of a rotating rigid body which is a helical tail in this case, is given in the equations below:

$$\Pi_{in}(t) = \tau(t)_{X,tl} \, \omega_{eff}(t) = \int\limits_{A=A_{tl}} \left(\Sigma_Z(t) W(t) + \Sigma_Y(t) V(t) \right) dA \tag{45}$$

$$\left| \left\langle \Pi_{in} \right\rangle \right| = \left| \frac{\sum\limits_{t=\omega_{app}^{-1}}^{2\omega_{app}^{-1}} \Pi_{in}(t)}{\omega_{app}^{-1}} \right| \tag{46}$$

The power output definition can be made as different alternatives. In the first case, power output is defined as the work done while the swimmer is translating in the x axis.

48

$$\Pi_{out,x}(t) = F_{x,b}(t)u_{cm}(t) = \left(\int\limits_{A=A_b} \Sigma_x(t)dA \right) u_{cm}(t) \qquad (47)$$

$$\left| \left\langle \Pi_{out,x} \right\rangle \right| = \left| \frac{\displaystyle\sum_{t=\omega_{app}^{-1}}^{2\omega_{app}^{-1}} \Pi_{out,x}(t)}{\omega_{app}^{-1}} \right| \qquad (48)$$

By putting aside the power needed to swim in the x axis, the power needed to swim in y and z directions can be calculated together:

$$\Pi_{out,y,z}(t) = \left[F_{y,b}(t)v_{cm}(t) + F_{z,b}(t)w_{cm}(t) \right]$$
$$= \left[\left(\int\limits_{A=A_b} \Sigma(t)_y \, dA \right) v(t)_{cm} + \left(\int\limits_{A=A_b} \Sigma(t)_z \, dA \right) w(t)_{cm} \right] \qquad (49)$$

$$\left| \left\langle \Pi_{out,y,z} \right\rangle \right| = \left| \frac{\displaystyle\sum_{t=\omega_{app}^{-1}}^{2\omega_{app}^{-1}} \Pi_{out,y,z}(t)}{\omega_{app}^{-1}} \right| \qquad (50)$$

The total time averaged power to translate in the space frame becomes:

$$\left| \left\langle \Pi_{out} \right\rangle \right| = \left| \left\langle \Pi_{out,x} \right\rangle \right| + \left| \left\langle \Pi_{out,y,z} \right\rangle \right| \qquad (51)$$

2.3.2 Propulsive Efficiency

Propulsive efficiency is defined by Chattopadhyay etal [14] and Magariyama etal [24] as the ratio of the propulsive power output to rotary power input. Moreover, propulsive efficiency for a rigid helix has also been derived analytically [14]. In order to have a direct comparison, in addition to time averaged propulsive efficiency, $|\langle\eta_x\rangle|$; two other efficiencies, $|\langle\eta_{y,z}\rangle|$ and $|\langle\eta_{x,y,z}\rangle|$ are defined in the following equations:

$$\left| \left\langle \eta_x \right\rangle \right| = \left| \frac{\left\langle \Pi_{out,x} \right\rangle}{\left\langle \Pi_{in} \right\rangle} \right| 100 \qquad (52)$$

$$\left|\left\langle \eta_{y,z} \right\rangle\right| = \left|\frac{\left\langle \Pi_{out,y,z} \right\rangle}{\left\langle \Pi_{in} \right\rangle}\right| 100 \qquad (53)$$

$$\left|\left\langle \eta_{x,y,z} \right\rangle\right| = \left|\frac{\left\langle \Pi_{out} \right\rangle}{\left\langle \Pi_{in} \right\rangle}\right| 100 \qquad (54)$$

2.4 Numerical Model

2.4.1   Mesh Requirements

The micro swimmer in the micro channel is modeled only as the fluid filling the volume between the micro swimmer and channel. So, the micro swimmer itself is not modeled from a structural perspective. However, only hydrodynamic interactions between the swimmer and the working fluid are modeled. The fluid domain is represented by a moving and deforming mesh which possesses an empty sub domain representing the micro swimmer. For the fact that Navier-Stokes equation does not need to be solved in the micro swimmer domain it can be left empty to gain processing power. Hence, the initial drawing of the fluid domain is given in Fig 10.

The straight rod attached to the ellipsoid swimmer body is the geometric form of the helical tail in the initial condition. By specifying deformations on the straight rod surface, the rod deforms into a helix tail as time passes by. However, the mesh points neighboring the ones on the helix surface should keep up with the displacements which are dependent on time and mesh point position. Moreover, the micro swimmer changes orientation by rotating in the Y and Z directions and these rotations, such as in the helix deformation case, create differential mesh displacements on the neighboring mesh nodes.

The procedure mentioned above forces the mesh nodes to break their connection or deform with a critical magnitude. This requirement forces the model meshed with very small mesh elements. The element sizes depend on the mesh deformation magnitude which is

induced by the swimmer rotation and helical tail amplitude. The required element size is found trial and error until the solutions converge.

In order to create an open boundary effect around the micro swimmer and to minimize channel inlet and outlet effects the micro channel needs to be drawn with a very large scale relative to micro swimmer. The channel inlet and outlet are drawn with a distance which is 10-30 times for the parametric swimmers with a 6-2 μm tail length. In addition to minimizing the inlet and outlet effect, the radial boundaries of the micro channel has been drawn with a minimum value of 10 for the ratio between channel radius and swimmer diameter as Goto's work [31] required creating an open boundary effect. Hence, a micro channel completely filled with small mesh elements would increase the degrees of freedom that would drastically decrease computing efficiency.

2.4.2   Mesh Sub Domains

In order to increase computing efficiency, a secondary and a smaller cylinder has been drawn around the micro swimmer introducing a channel dummy sub domain much smaller than the micro channel. The purpose of this channel dummy cylinder is being filled with mesh elements small enough to compensate the differential mesh displacements on the helix tail and swimmer body. Moreover, the small mesh elements in the channel dummy cylinder do not decrease the computation performance as much as it would in a case of high quality meshed micro channel.

In Figures 18 and 19 there are four sub domains which are serving certain purposes and are subject to certain constraints. The first sub domain, namely the micro channel is fixed to space frame. Moreover, the micro channel longitudinal axis and the *x* axis are aligned. The following sub domains do not correspond to real rigid bodies and they only have numeric modeling purposes. The second sub domain, namely the channel dummy cylinder is a secondary volume drawn in the micro channel to encapsulate the micro swimmer. It is meshed with smaller elements than the ones in rest of the micro channel. It is fixed to space frame and its longitudinal axis is aligned with the *x* axis. As the third sub domain, the swimmer dummy cylinder is introduced. This sub domain is fixed with the body frame and it encapsulates the micro swimmer with very small geometric tolerances. It has three degrees of rotation freedom relative to the space frame. Moreover, its longitudinal axis is always aligned with *X* axis. The last and the fourth sub domain is the tail dummy cylinder which only encapsulates the helical tail. This cylinder longitudinal axis is aligned with *X* axis and as time passes by the cylinder slices which are perpendicular to *X* axis displace in *Y* and *Z* direction with the mesh nodes

residing at the same slice. The sub domains encapsulate each other from the formerly mentioned to the latter.
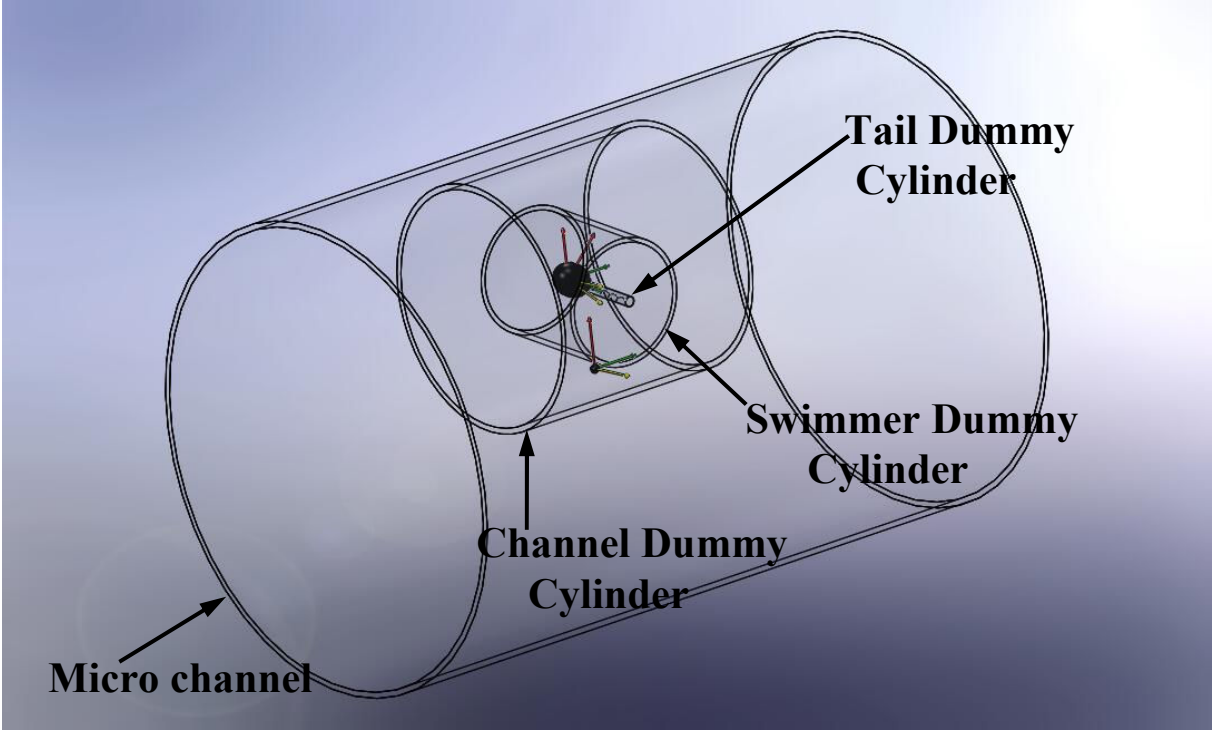
Figure 18: Trimetric view of micro channel and swimmer with arbitrary sub domains
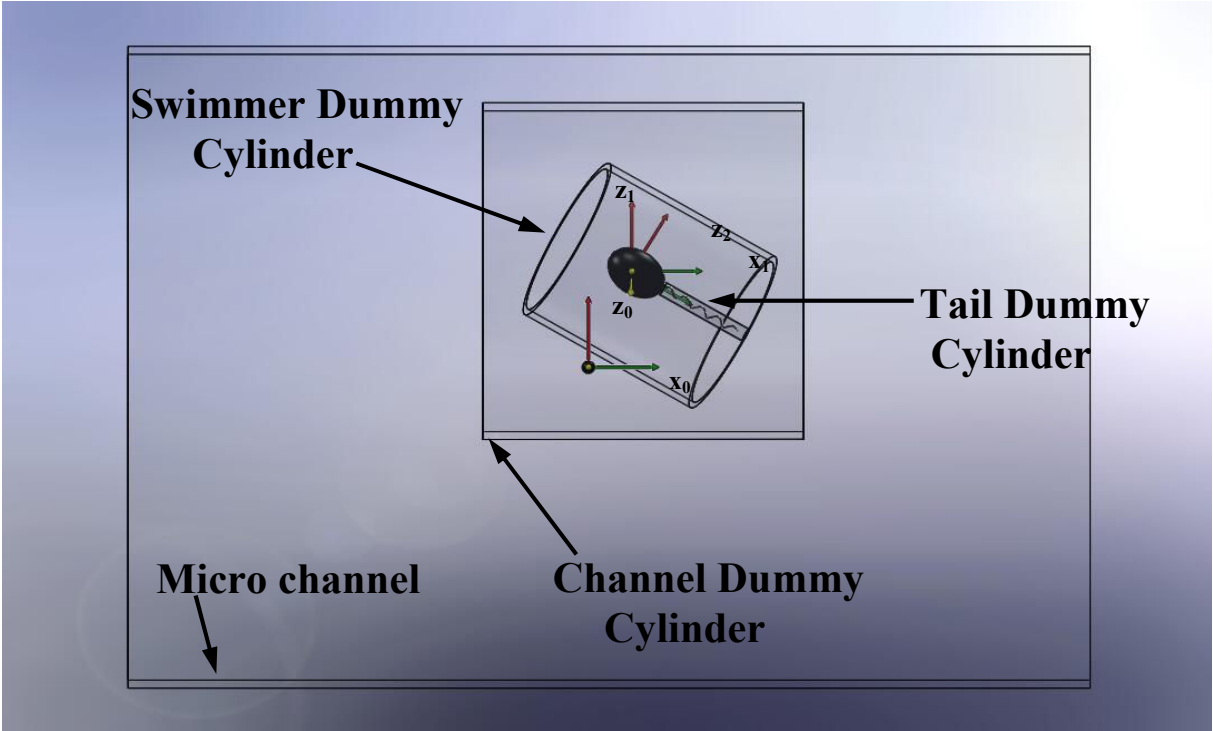
Figure 19: Side view of micro channel and swimmer with arbitrary sub domains.

2.4.3 Mesh Zones

This simulation based work handles the mesh deformations with an ALE mesh description which combines the strengths of Lagrangian and Eulerian descriptions. Their strength has been explained in detail in Section 1.4.3. For this fact, the mesh nodes closer to the origins of mesh displacements, which are structure–fluid interfaces, are specified to have Lagrangian mesh displacements. However, the mesh nodes residing further distances, are specified to have Eulerian mesh displacements.

Mesh nodes move according to zones which keep the unity of the mesh. The zones are displacement restrictors which have function output values to be multiplied with the displacement of every mesh nod in the domain. The output values of these functions can vary between zero and unity. In short, the output values are unity for the smallest available dummy sub domain which encloses the nodes with the same deformation pattern. The other mesh nodes, which are excluded by this dummy sub domain, receive an output value closer to zero with respect to an increasing distance to the dummy sub domain. Therefore, the mesh can deform in a way that it can actually take the exact desired form on the boundaries of the modeled geometry which is moving due to rigid body dynamics. At the same time, the mesh absorbs the displacement originating from the moving geometry so that external constraint boundaries do not need to displace in the perpendicular direction to them. However, as long as the mesh is constraint in the direction perpendicular to external boundary surfaces, the mesh nodes are allowed to glide tangentially to surfaces.

The zones are defined according to the initial positions of mesh nodes. Even the nodes displace during the simulation, the effect of a zone on each mesh point stays the same. Therefore, all mathematical formulations use the initial coordinates, $\mathbf{x}(0)$ of each point.

According to the criterion given above, there are two types of mesh zones namely longitudinal and radial mesh zones. A longitudinal mesh zone regulates the displacements in the x axis of any frame. In the radial axis which is perpendicular to longitudinal x axis, the deformations in the y and z axes are regulated by radial zones.

The longitudinal mesh zone is only dependent on the position coordinate in the longitudinal axis. Therefore, the output of this zone is valid for the whole cross section

perpendicular to longitudinal axis. The generic output of a longitudinal mesh zone versus longitudinal axis generates a trapezoid as it is depicted in Fig. 20.

The longitudinal mesh zone used in all models, $Zn_{x,rot}$ regulates the displacements in the x axis which are induced by a rotation of the micro swimmer about the y or z axis. Since the displacement is in the x axis and the zone regulates the displacement induced by the swimmer rotation, the sub script of Zn is chosen as x,rot. For the fact that the longitudinal axis of the micro channel lays on the x axis, the mesh nodes cannot pass throughout the inlet and outlet. However, any displacement in the x direction can be accompanied by the same displacement of other mesh nodes residing at the same cross section with the former mesh node. Therefore, the mesh points displace with the same magnitude in the x direction by simply mimicking the actuated mesh node if they are residing at the same cross section perpendicular to the micro channel longitudinal axis. This means that mesh nodes residing on the radial channel walls glide on their boundaries. The mathematical formulation of the criteria is given in Eq. 55 and the plot of it is given in Fig. 20:

$$Zn_{x,rot} = \begin{cases} x(0) \le X\lim_2 & \min\left\{ \begin{array}{c} 1 \\ \dfrac{x(0) - X\lim_0}{X\lim_1 - X\lim_0} \end{array} \right. \\ X\lim_2 < x(0) \le X\lim_3 & 1 - \dfrac{x(0) - X\lim_2}{X\lim_3 - X\lim_2} \end{cases} \qquad (55)$$
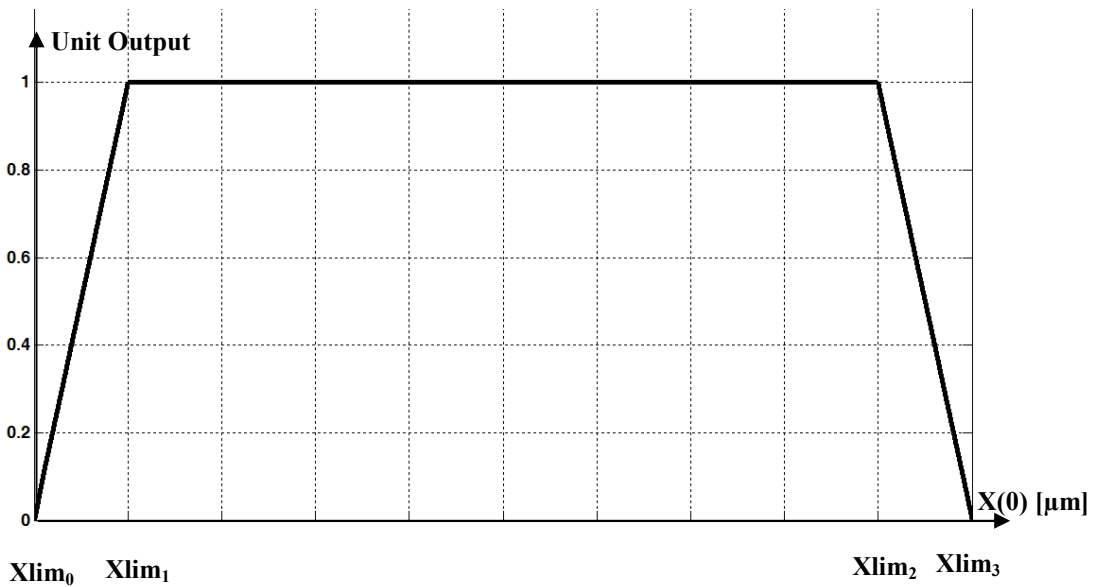
Figure 20: The output for the longitudinal mesh zone, $Zn_{x,rot}$.

As in the Fig. 20, the longitudinal mesh zone expressed in the space frame, completely allows the x displacement of channel dummy cylinder which is in between the x limits of $Xlim_1$ and $Xlim_2$. The mesh nodes which are out of this range translate with a decreasing percentage as they get closer to inlet or the outlet. The application of the zone is depicted in Fig. 21. However, swimmer and tail dummy cylinders are not depicted for convenience.
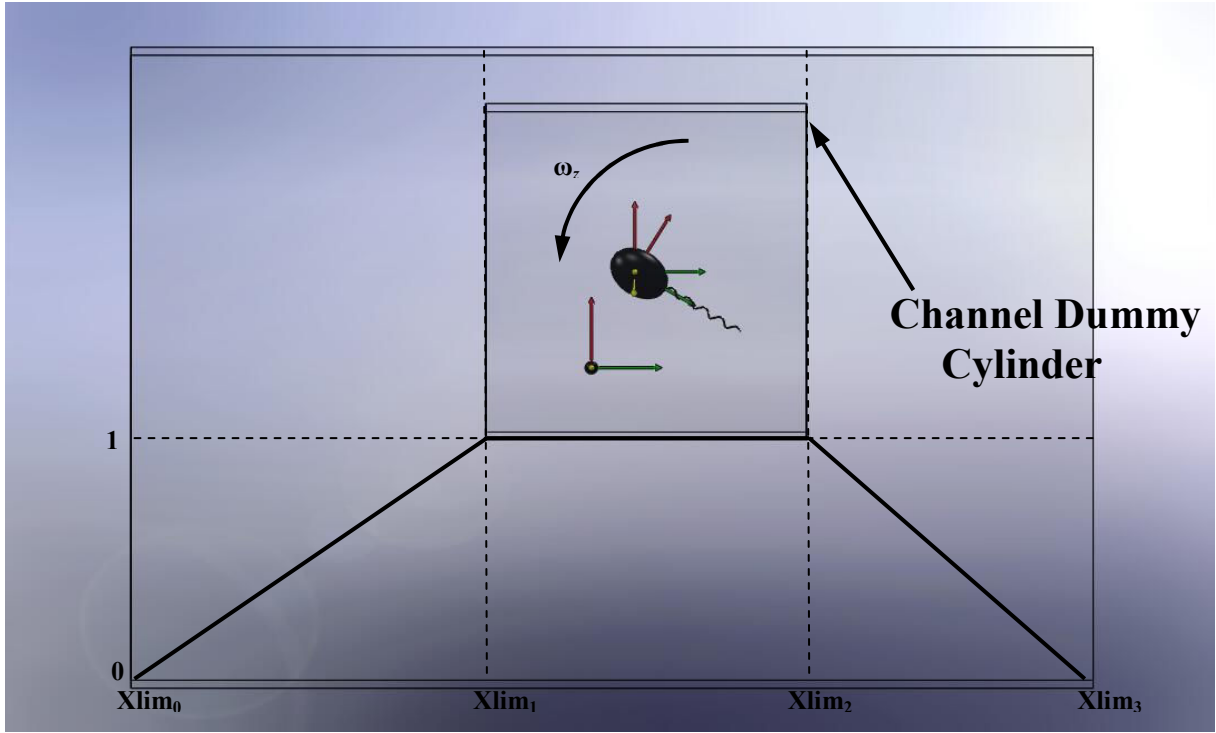
Figure 21: The application of the longitudinal mesh zone, $Zn_{x,rot}$ for a rotation about z axis.

The first radial mesh zone, $Zn_{y,z,rot}$ is formulated in case of a mesh node moving in y or z direction induced by the rotations of the micro swimmer about y-z axes. Since the displacement is in the y-z axes and the zone regulates the displacement induced by the swimmer rotation, the sub script of Zn is chosen as y,z,rot. The displacement is constraint by the micro channel surfaces in the radial direction. Every displacement in the radial direction, induced by a mesh node on the rotating micro swimmer and in the swimmer dummy cylinder can either compress or tense the mesh nodes in the micro channel. The zone is mathematically formulated in Eq. 56 and 57. The plot of the zone is given in Fig. 22 and the application is depicted in Fig 23 but the channel dummy cylinder is not depicted for convenience.

$$r_x(0) = \sqrt{y^2(0) + z^2(0)} \tag{56}$$

55

$$Zn_{y,z,rot} = \begin{cases} r_x(0) \le R_{sw,dm,cyl} & 1 \\ R_{sw,dm,cyl} < r_x(0) \le R_{ch} & 1 - \dfrac{r_x(0) - R_{sw,dm,cyl}}{R_{ch} - R_{sw,dm,cyl}} \end{cases} \tag{57}$$
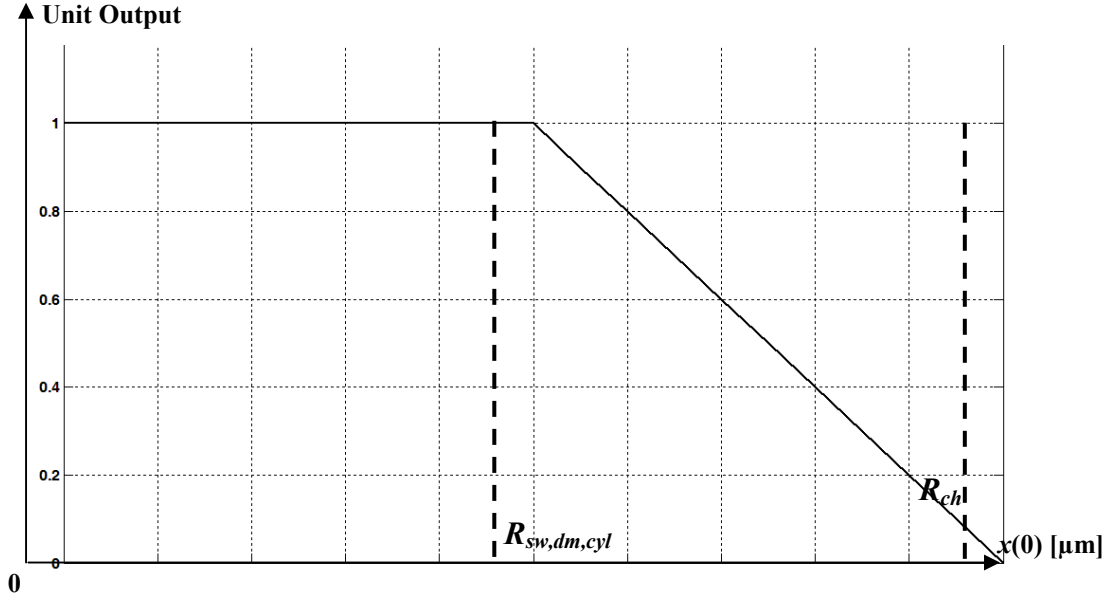
Figure 22: The plot of radial zone, $Zn_{y,z,rot}$.
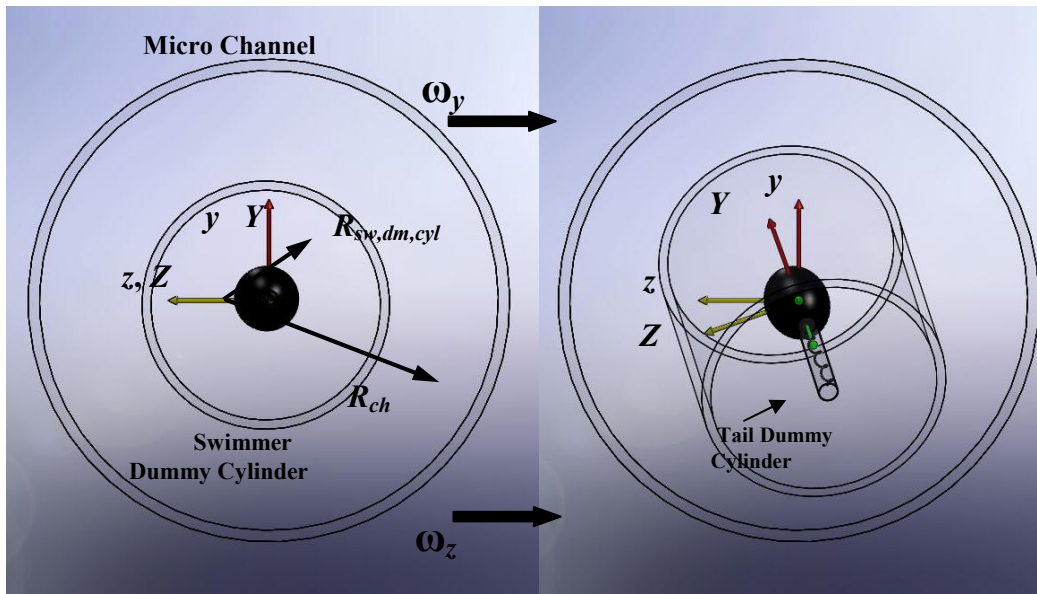
Figure 23: The 3D application of the radial zone, $Zn_{y,z,rot}$.

The second and the last radial zone, $Zn_{y,z,tl}$ regulates the displacement of the helix tail, $\mathbf{dX}_{tl}$ in the y and z axes. The displacements are constraint by the micro channel. The working principle is the same with the previous radial zone. The plot of the zone is given in Fig. 24 and the application of it can be seen in the Fig. 25.

56

$$Zn_{y,z,tl} = \begin{cases} r_x(0) \le R_{tl,dm,cyl} & 1 \\ R_{tl,dm,cyl} < r_x(0) \le R_{ch} & 1 - \dfrac{r_x(0) - R_{ch}}{R_{ch} - R_{tl,dm,cyl}} \end{cases} \tag{58}$$
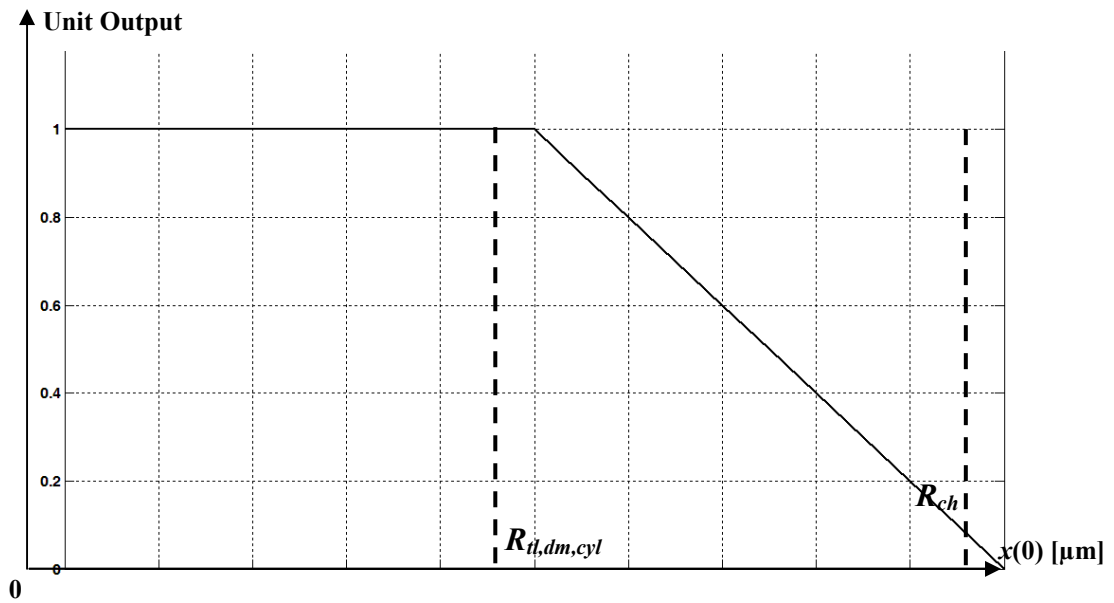
Figure 24: The plot of radial zone, $Zn_{y,z,tl}$.
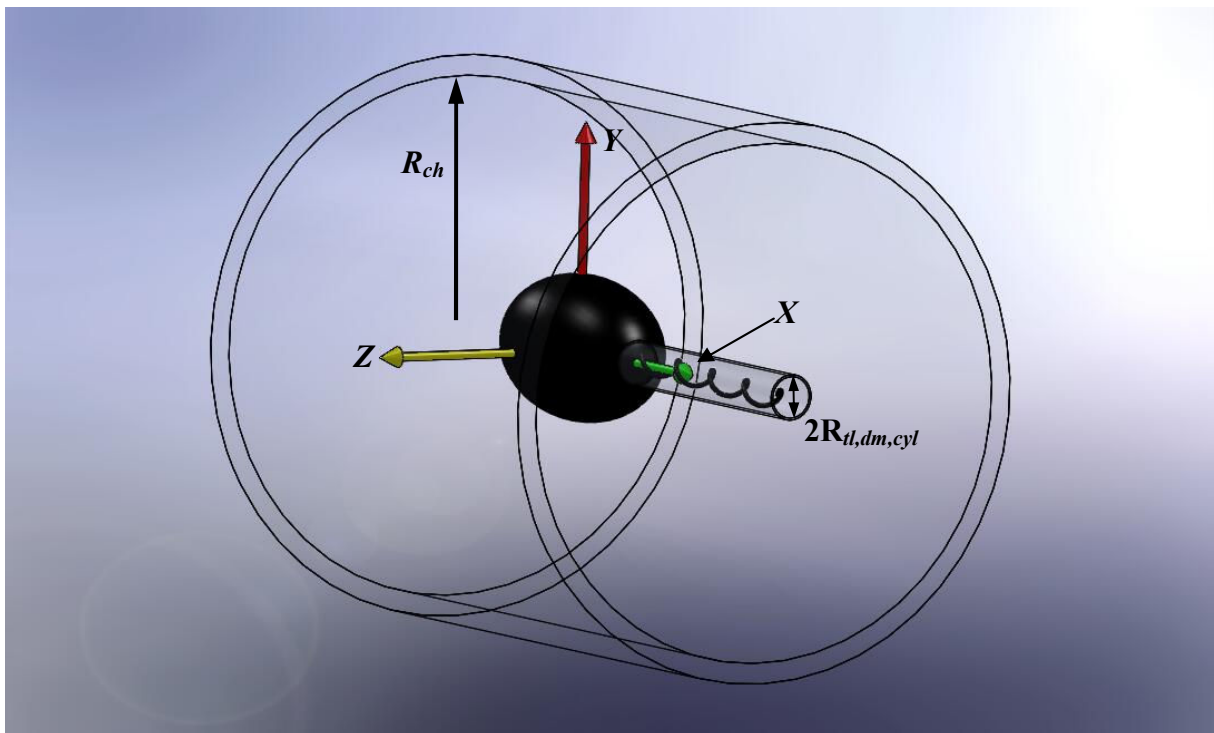
Figure 25: The application of radial zone, $Zn_{y,z,tl}$

2.4.4 Mesh Displacements

The mesh displacement in the channel can be divided into two procedures. The first mesh displacement is done in order to reorient the micro swimmer in the channel. This displacement is achieved by the use of a different transformation matrix, $\mathbf{R}_{orient}$ other than the transformation matrices used for switching between body and space frames. The rotational motion of the swimmer does not affect the orientation of the swimmer because the swimmer is axis symmetric around X axis. For this reason, there is no contribution of the angular velocity expressed in the X axis to the transformation matrix, $\mathbf{R}_{orient}$.

$$\dot{\mathbf{R}}_{orient}(t) = \begin{bmatrix} \mathbf{R}_{orient}(1,2)\omega_z - \mathbf{R}_{orient}(1,3)\omega_y & \mathbf{R}_{orient}(1,1)\omega_z & \mathbf{R}_{orient}(1,1)\omega_y \\ \mathbf{R}_{orient}(2,2)\omega_z - \mathbf{R}_{orient}(2,3)\omega_y & \mathbf{R}_{orient}(2,1)\omega_z & \mathbf{R}_{orient}(2,1)\omega_y \\ \mathbf{R}_{orient}(3,2)\omega_z - \mathbf{R}_{orient}(3,3)\omega_y & \mathbf{R}_{orient}(3,1)\omega_z & \mathbf{R}_{orient}(3,1)\omega_y \end{bmatrix} \tag{59}$$

$$\mathbf{R}_{orient}(t) = \int_{t=0}^{t} \dot{\mathbf{R}}_{orient}\, dt \tag{60}$$

An arbitrary point on the micro swimmer has the coordinates of $x(0)$, $y(0)$ and $z(0)$ at the initial condition. At the t second, the partial position changes of this arbitrary point induced by the rigid body rotations are given in the equations below.

$$\begin{bmatrix} \Delta x(t) \\ \Delta y(t) \\ \Delta z(t) \end{bmatrix} = \mathbf{R}_{orient}(t)\mathbf{x}(0) - \mathbf{x}(0) \tag{61}$$

The displacements are regulated with the corresponding mesh zones in the micro channel in Eq. 62.

$$\begin{bmatrix} \Delta x_{rot} \\ \Delta y_{rot} \\ \Delta z_{rot} \end{bmatrix} = \begin{bmatrix} \Delta x(t) Zn_{x,rot} \\ \Delta y(t) Zn_{y,z,rot} \\ \Delta z(t) Zn_{y,z,rot} \end{bmatrix} \tag{62}$$

In the second part of the mesh displacement, the helical tail rotation is obtained by specifying the y-z deformation of each slice on a straight rod. The position of each slice from the straight rod is given in Eq. 34. The θ_X value is the time integral ω_X. Therefore, unused ω_X values in $\mathbf{R}_{orient}$ matrix calculation, is now used in helical tail rotation. Equation 30 gives the

displacement of the straight rod in the body coordinates. In result, the displacement vector for the mesh becomes:

$$\mathbf{dx}_m = \begin{bmatrix} \Delta x_{rot} \\ \Delta y_{rot} + \Delta y_{tl} \\ \Delta z_{rot} + \Delta z_{tl} \end{bmatrix} \quad (63)$$

The mesh displacements are specified as "physics induced mesh deformation" in COMSOL ALE module settings because these displacements are results of the forces and torques calculated as an output of Navier-Stokes module [32].

2.4.5   Mesh Configuration

In all the numeric models simulated in this work are meshed with quadratic Lagrange finite elements which are tetrahedrons. In total, there are five mesh parameters to be optimized for high computing performance and precision. These parameters are: "the maximum sub domain mesh element size" in the micro channel ($Ms_{ch,sd}$, Fig. 26) and channel dummy cylinder ($Ms_{dm,cyl,sd}$, Fig. 27); "the maximum boundary mesh element size" on the surface of micro swimmer body and tail ($Ms_{sw,b,srf}$ and $Ms_{sw,tl,srf}$, Fig. 28); and the element growth rate (EGR) for each element size. The optimized values as a result of trials and errors, and their corresponding degrees of freedom and number of elements for all cases in this work are given in Table 5.
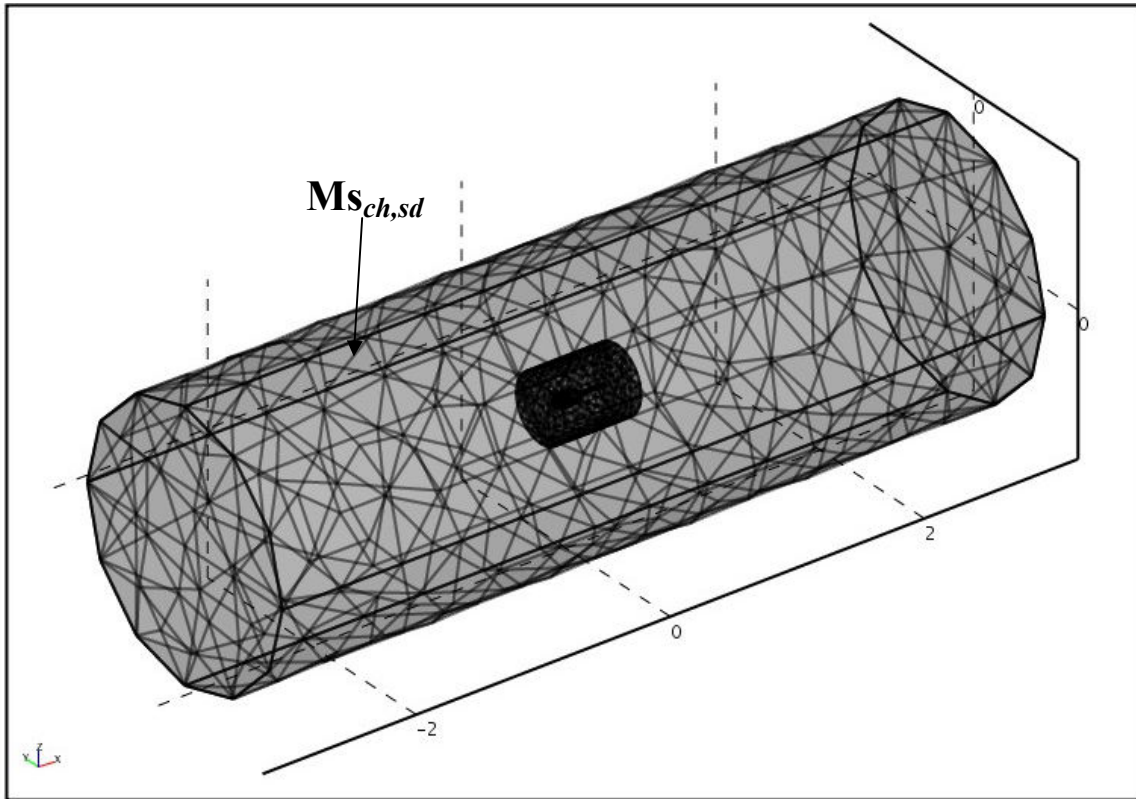
Figure 26: Maximum sub domain element size for micro channel.
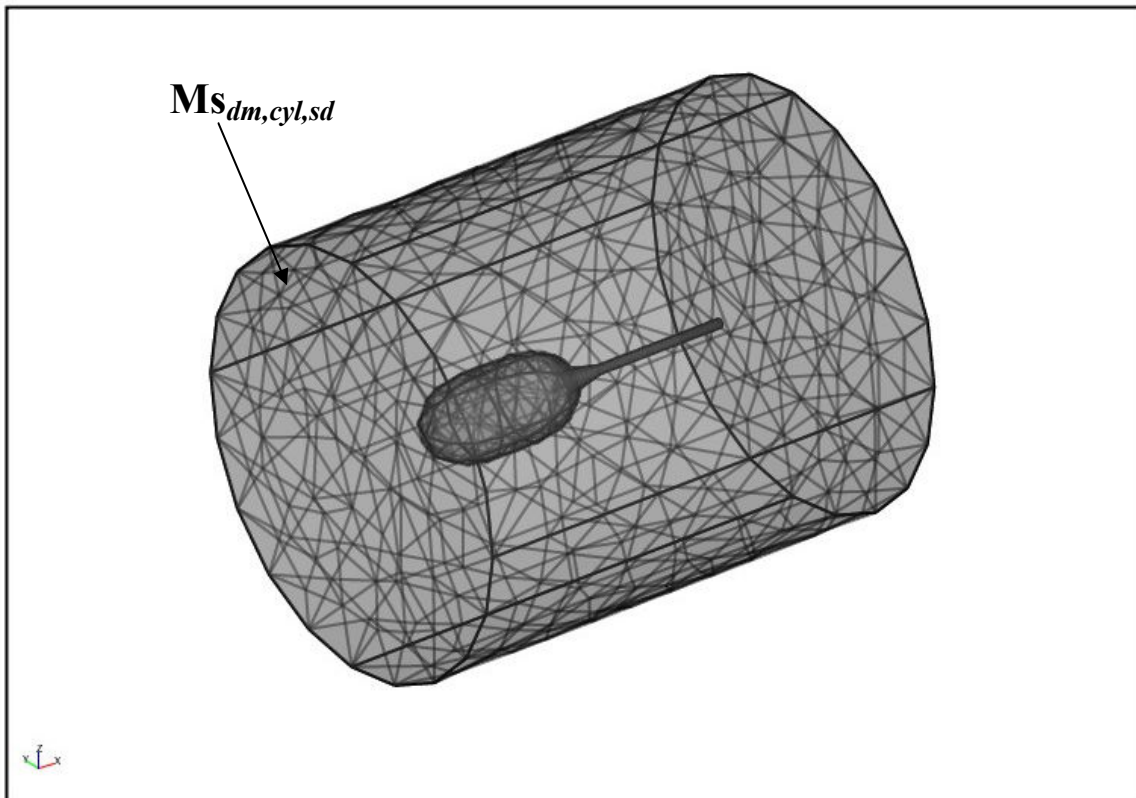
Figure 27: Maximum sub domain element size for channel dummy cylinder.
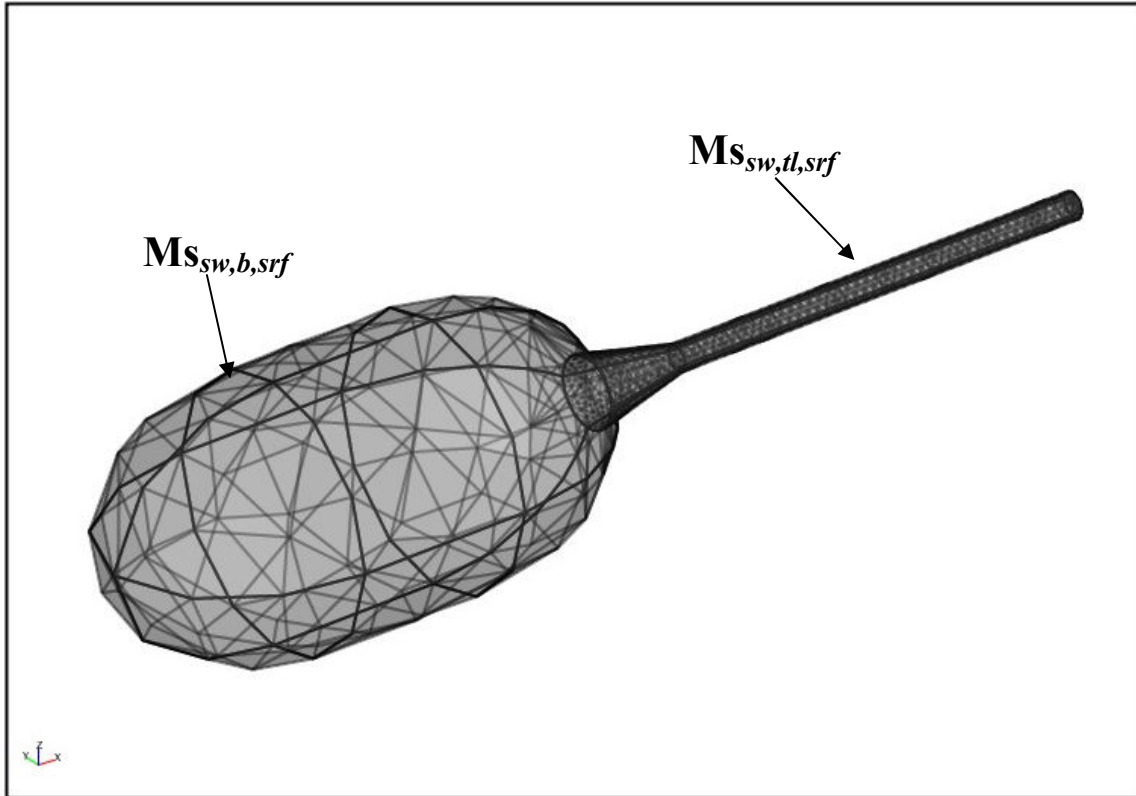
Figure 28: Maximum boundary element sizes for swimmer body and tail.

	Vibrio alginolyticus	Parametric Swimmer
EGR / $Ms_{ch,sd}$	2 / 10 μm	2 / 5 μm
EGR / $Ms_{dm,cyl,sd}$	2 / 1 μm	2 / 0.8 μm
EGR / $Ms_{sw,b,srf}$	2 / 0.1 μm	3 / 0.4 μm
EGR / $Ms_{sw,tl,srf}$	2 / 0.03 μm	2 / 0.04 μm
# DOF	198536	91449
# Tetrahedral elements	33676	16853
# Triangular	7504	3096

Table 5: Mesh configuration for models.

2.4.6 Solver Settings

On the mesh points which were explained above, Navier-Stokes equations are solved with weak constraints by the Parallel-Direct-Sparse-Solver (PARDISO) with a relative tolerance of 10^{-3} and an absolute tolerance of 10^{-4}. The solver maximum time step size is selected one twentieth of the applied tail rotation period for the parametric swimmer runs.

However for the V. alginolyticus model, time step size is selected one ten thousandth of the applied rotation period. This value has been used by Hsu-Dillon [19] in their recent work. With these mentioned solver settings, each parametric swimmer and the V. alginolyticus simulation takes about 12 hours on average and about 5 days on a double-core, 3.7GHz, Xeon processor workstation with 16GB RAM and running 64-bit SUSE 10.2 Linux operating system.

2.5 Parametric Approach

The six degrees of freedom motion (DOF) of a micro swimmer depends on the geometric properties of the swimmer body and propulsion mechanism. The geometric properties of the body, in other words: the cargo is not parametrically analyzed in this work. However, a parametric analysis for the propulsion system is presented.

The propulsion system of the micro swimmer consists of a rotating helix tail at the back of the swimmer ellipsoid body. The output of this propulsion system, which is the six dof motion, was presented in the Section 2.1. The effect of the input parameters will be measured with respect to the change in outputs.

The input parameters for the propulsion are the applied rotation frequency (ω_{app}), axial length (L_{tl}), wavelength (λ) and maximum amplitude of the helix tail (B_0). The selected values for these parameters are in Table 6. These parameters are selected according to the observed features of micro organisms reported in Section 1.3.2.

ω_{app}	5, **20**, 320, 640 [Hz]
L_{tl}	**2**, 4, 6 [μm]
B_0	0.05, **0.1**, 0.2, 0.4 [μm]
λ	1, 1.5, **2**, 2.5 [μm]

Table 6: The range of parameters for the parametric swimmer.

For each parameter set, an individual time-dependent simulation runs. For analyzing the effect of each parameter, simulations run by changing only one parameter at a time and keeping the other parameters at their reference values. The reference values of each parameter are written in bold in Table 6. As the requirement of the one-factor-at-a-time approach, 13 simulations in total run.

In order to analyze the effect of the applied rotational frequency, it should be considered with the rotation of the swimmer head. As a result of applied tail rotation, which is relative to swimmer head, there is a rotation of the head in the opposite direction. This counter rotation decreases the rotational frequency of the tail with respect to the fluid (ω_{eff}). Hence, the change in swimmer motion should be also evaluated with respect to ω_{eff}.

In addition to ω_{app}, the effect of parameters B_0 and λ should be evaluated with respect to the change in total helical tail length, l_{tl} they cause. According to Eq. 11, there is a positive correlation between the B_0 - λ values and l_{tl}. So, a separate parametric analysis of l_{tl} is required. With the constant B_0 - λ values, the total helix length and the axial length are linearly dependent. Therefore, with the obtained correlation between L_{tl} and the motion of the swimmer, the effect of the B_0 - λ parameter can be analyzed individually and clearly.

2.6 Assumptions

In the numeric models presented in this work, the following assumptions are made:
- Brownian Motion is ignored
- Coriolis force is ignored
- Helical tail is assumed to be rigid

CHAPTER 3

RESULTS

3.1 Validation Means

The same numerical modeling procedure is applied to the V. Alginolyticus and parametric swimmer models. The V. Alginolyticus and parametric swimmer model only differ with their mesh qualities. The corresponding mesh qualities presented in Table 5, show that the V. Alginolyticus model has a higher quality mesh than the parametric swimmer model. Therefore, V. Alginolyticus model is expected to reflect the observed motion parameters with a small error. The amount of the error will be presented in the next chapter. The parametric swimmer simulations can only reflect the effect of parametric changes but cannot result the observed motion parameters with the same precision that the V. Alginolyticus model has. These validation means are presented in the following chapter.

3.1.1 Comparison of the Numeric Results of Vibrio Alginolyticus with the Observed Data

The swimming motion of V. Alginolyticus with a single flagellum, has been observed by Magariyama etal in 1995 [24], Goto etal in 2001 [4] and Chattopadhyay etal in 2009 [26]. In this work, except one parameter, all of the geometric and motion parameters for the flagellum and cell body are taken from the work of Chattopadhyay etal [26] and generated a one-to-one model of the V. Alginolyticus. The only modified parameter is the maximum helical tail amplitude. Because of using a geometric ramp function on the tail as in Eq. 31, the effective tail amplitude factor is calculated with $m=0.2$ and Eq. 32. As a result, the amplitude taken from the literature is multiplied with 1.186 and used in the simulation.

The numeric results are compared not only with the observation results of Chattopadhyay etal [26] but also with the results of Magariyama etal [24] and Goto etal [4] obtained from the same bacterium race with deviations in their geometric and motion parameters.

The rotation of the helical flagellum (ω_{app}) and the cell body (ω_X) with respect to the space frame is reported to be 571 and 26 Hz respectively [26]. Therefore, the applied rotary motor frequency is calculated to be 571+26=597 Hz. The rest of the constants used in the

model are given in Table 3. With the inputs mentioned above, the swimming speed is expected to be 34 µm/s and the resulting rotations for the cell body and tail is expected to agree with the observed results.

In the observational work of Chattopadhyay etal [26], they deduce the drag force and the torque on the cell body by multiplying the measured swimming speed and the rotation rate with certain constants as in Equations [64-67]. The constants A_0 and D_0 are obtained by holding a bacterium with the use of externally imposed flow and optical tweezers [14]. Therefore, the force required to hold a bacterium can be directly measured as a function of externally imposed flow velocity. However, even these constants are in agreement with resistive force theory (RFT), they can largely vary among bacteria with same length grown from a single colony [14]. Equations 64-67 present the methodology to derive the drag forces and torques out of the swimming speeds and body rotations.

$$F = A_0 u_{cm} \tag{64}$$

$$A_0 = \frac{2\pi\eta L_b}{\ln\left(L_b / R_b\right) - 0.5} \tag{65}$$

$$\tau_X = D_0 \omega_X \tag{66}$$

$$D_0 = \frac{16}{3}\pi R_b^2 L_b \tag{67}$$

In Figure 29, the time dependent swimming speed is plotted. After the swimmer reaches to its maximum speed, around 36 µm/s, the swimming speed is plotted to be very close to 34 µm/s for the time interval between 0.002 and 0.0025 s. In between this time range, the numerical deviation from the 34 µm/s value is not larger than the observational standard deviation, 1 µm/s reported by Chattopadhyay etal [26]. After 0.0025 seconds, due to the mesh deformation mostly induced by the rotation of the swimmer in y and z axes, the swimming speed slows down.
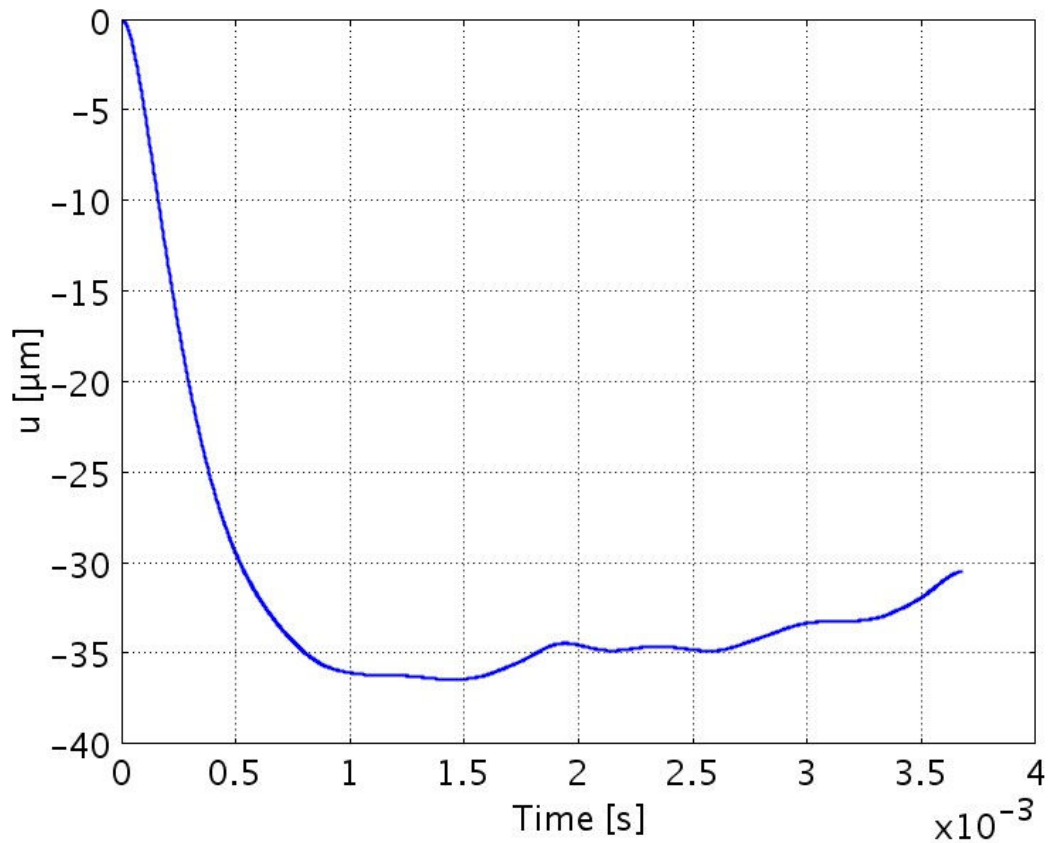
Figure 29: The simulation result for swimming speed, u_{cm} of V. Alginolyticus.

In Figure 30, the simulation result for the body rotation rate of the V. Alginolyticus is presented. The observed rotation rate [26] is 26 Hz with a standard deviation of 1 Hz. Figure 30 shows that the body rotation rate is simulated with 21.1% error. This error is one of the reasons for the other motion parameters to deviate from their expected values. Moreover, Chattopadhyay presented dimensionless swimming velocities which are experimentally observed and analytically predicted by slender body theorem (SBT) and resistive force theory (RFT) versions by Lighthill and Gray-Hancock [26]. According to the results of the results of the Chattopadhyay, SBT is the most successful one to predict the swimming velocity. The accuracy of SBT (85%) and the numerical swimming velocity result (~90% on average, ~100% for $0.002 < t < 0.0025$) are in the same accuracy range [26].
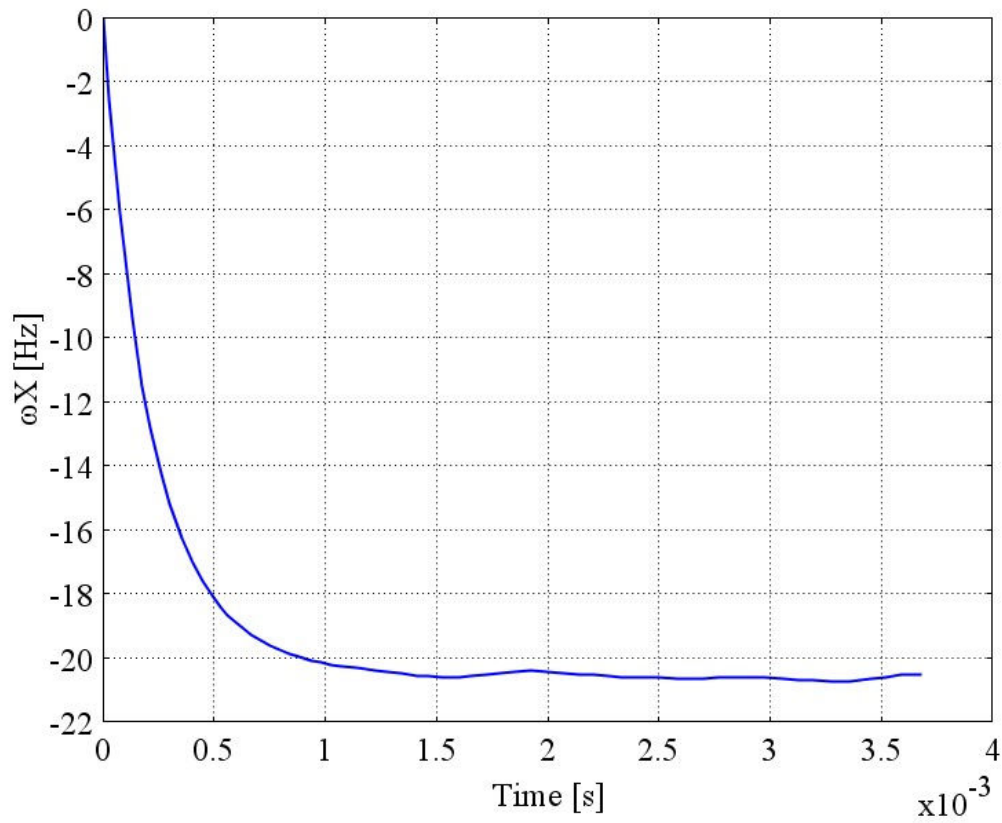
Figure 30: The simulation result for cell body rotation, ω_X of V Alginolyticus.

By using Equations 64 and 65, the drag on the V. Alginolyticus body is derived and compared with the numerical results. Figure 31 shows that there is a 40% overshoot by the numerical result compared to the analytical prediction.
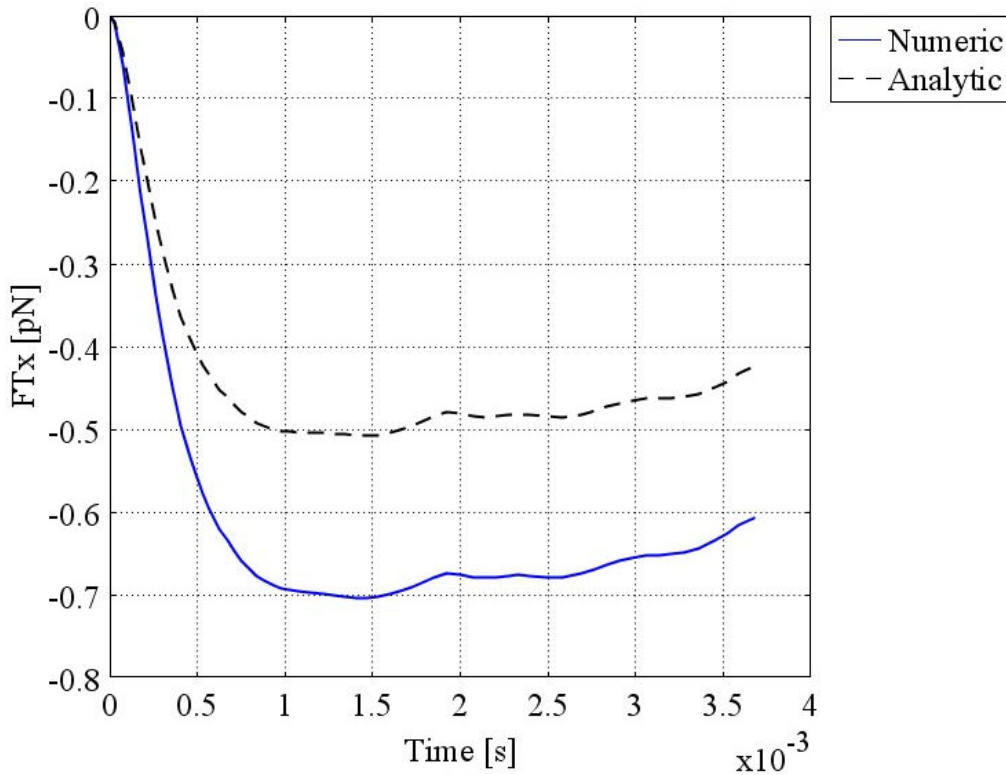
Figure 31: The simulation result and analytical prediction for V Alginolyticus body drag.

Equations 66 and 67 output the predicted torque of the V. Alginolyticus body and this value is compared with the numerical result. In Figure 32, the results intersect at the time interval 0.002 and 0.0025 when the numerical swimming speed outputs the observed value. The resulting 0.6 pNμm torque is also in agreement with the torque range 0.1-1 pNμm observed by Goto etal [4] and the 1 pNμm value by Magariyama etal [24] for the same race of V. Alginolyticus with different rotation rates and geometric sizes. The dimensionless torque values to make comparison between the observed results and analytical predictions show that SBT is the most accurate one among all. The overlapping plots of numerical and analytical results proved that simulations are an accurate predictor as SBT.
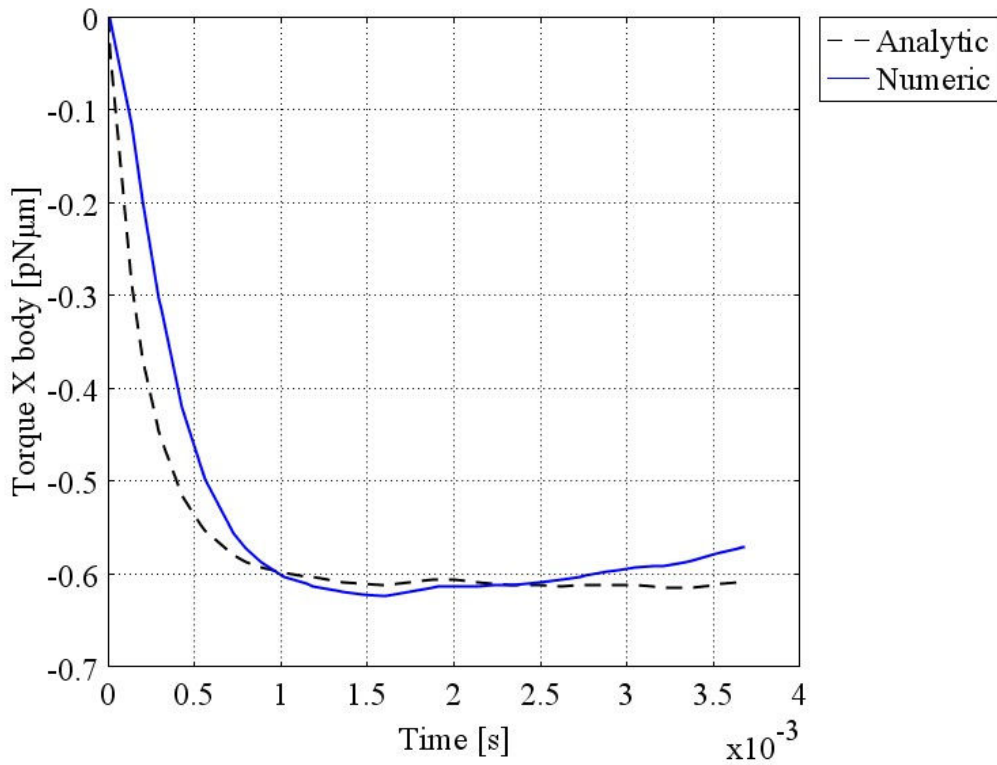
Figure 32: The simulation result and analytical prediction for V Alginolyticus body torque in the X axis.

Chattopadhyay [26] has lastly deduced the dimensionless the power requirement. The dimensionless power requirement is measured to be 650 units and SBT predicted it as 600 units which correspond to 92.3% agreement. The simulation result presented in Fig. 33 has a lower agreement (61.5%) than SBT. However, the accuracy of the simulation is still higher than RFT by Lighthill and Gray-Hancock (~%30).
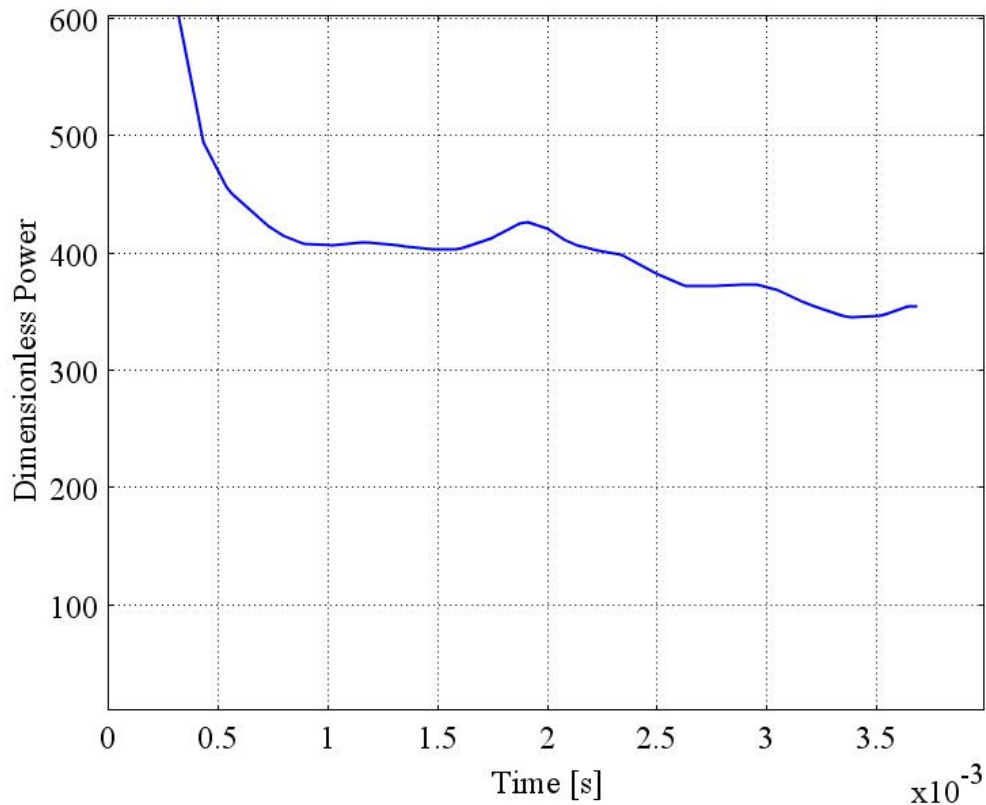
Figure 33: The dimensionless power requirement for V Alginolyticus.

Goto etal [4] introduced ratios of body torques and rotation rates which correspond to the load curve of the rotary motor. The observations [4] of different V. Alginolyticus cells with different sizes and rotation rates, show that the ratios are all around the 0.002 pNμm value. The simulation here outputs a value slightly larger than 0.001 pNμm.

In addition to body rotation torque and frequency ratio, Goto etal [4] has put forward another analysis parameter which is the ratio between the swimming speed and the body rotation rate. This numeric output of this parameter is plotted in Fig. 35 and this result (~1.6 μm) drops in the range of observational results which vary in between 1-2 μm.
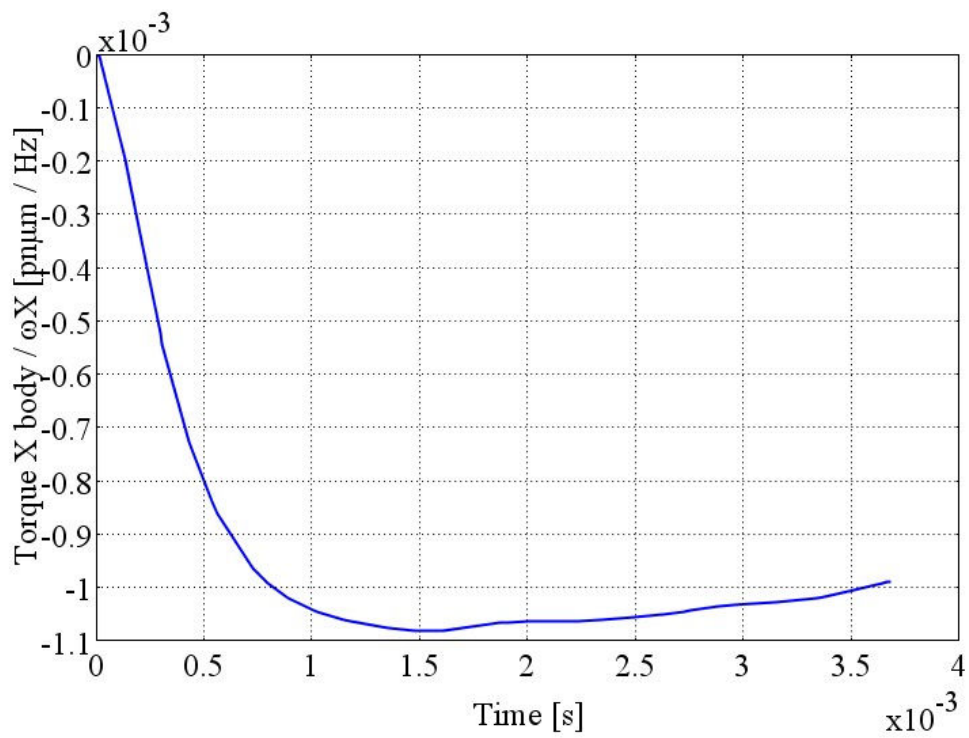
ure 34: The ratio of body torque and rotation for V. Alingolyticus.
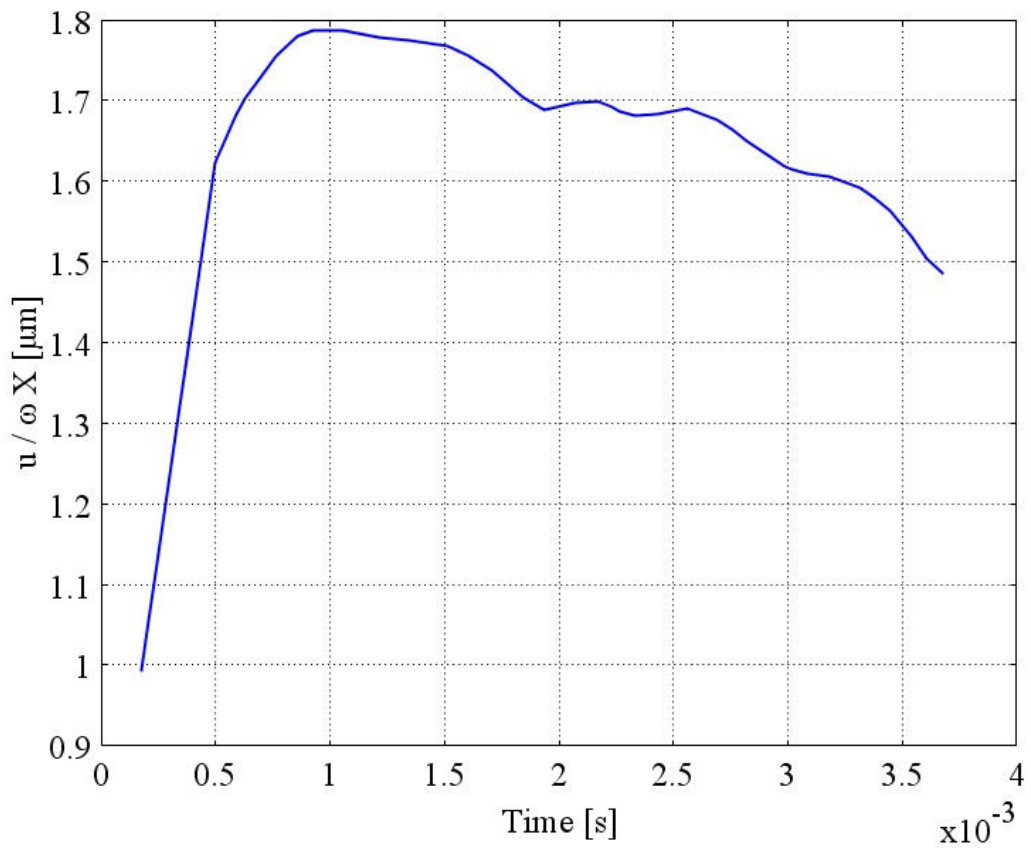
Figure 35: The swimming speed and body rotation ratio for V Alginolyticus.

An additional analysis parameter is put forward by Magariyama etal [24] which is the slip rate of the helical tail. The slip rate is found by the ratio of swimming speed to effective tail rotation with respect to the working fluid. This ratio is observed to be 0.113 μm on average whereas in Fig. 36, the nearly half of the observed value is plotted. This means that the simulated swimmer displaces less with per rotation of its helical tail than the observed swimmers.
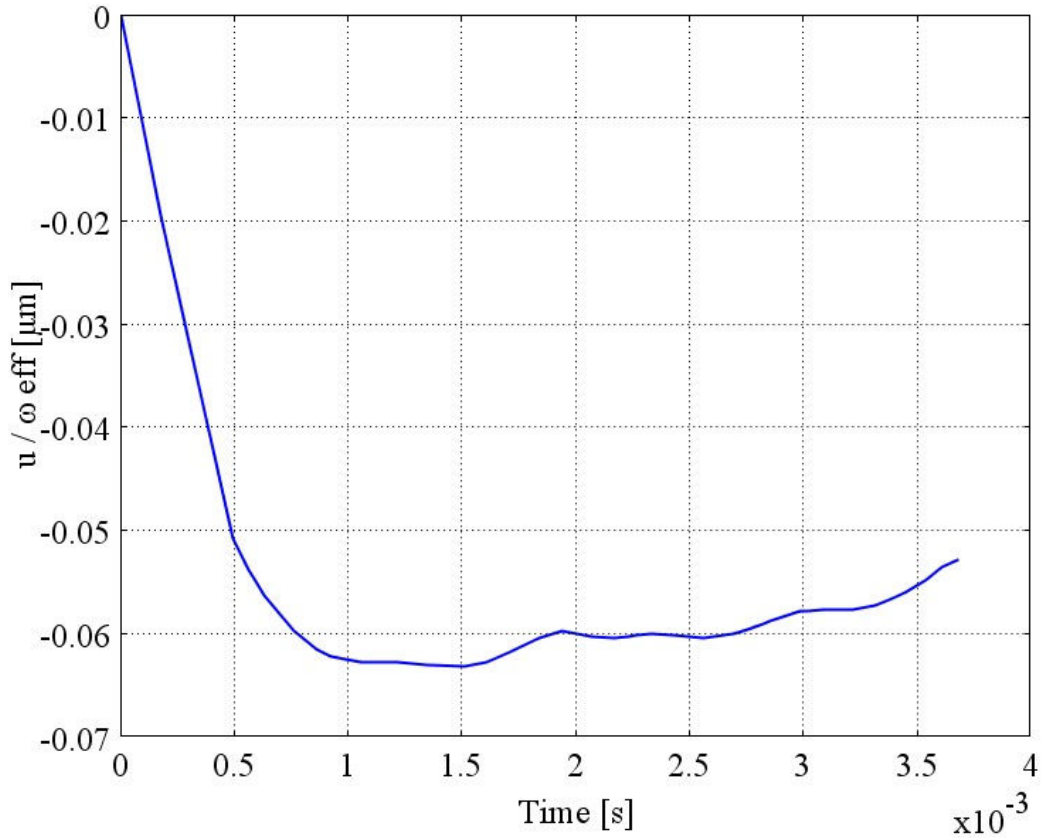
Figure 36: The swimming speed and tail rotation ratio for V Alginolyticus.

Different definitions of propulsive efficiency of a micro swimmer were made in Section 2.3.2. The propulsive efficiencies in the x axis and y-z axes are plotted separately in the Fig. 37. The simulation result of efficiency for propelling the swimmer in the x direction is in the range of values (1% < η < 2%) that Magariyama observed. The efficiencies of translating in the y-z axes are nearly zero (~0.017%) when they are compared with the efficiency in the x direction. Therefore, the values for $\eta_{y,z}$ are not depicted in Fig. 37. The main reason for having such a small efficiency is the helical trajectory of the swimmer which results no net displacement both in y and z axes.
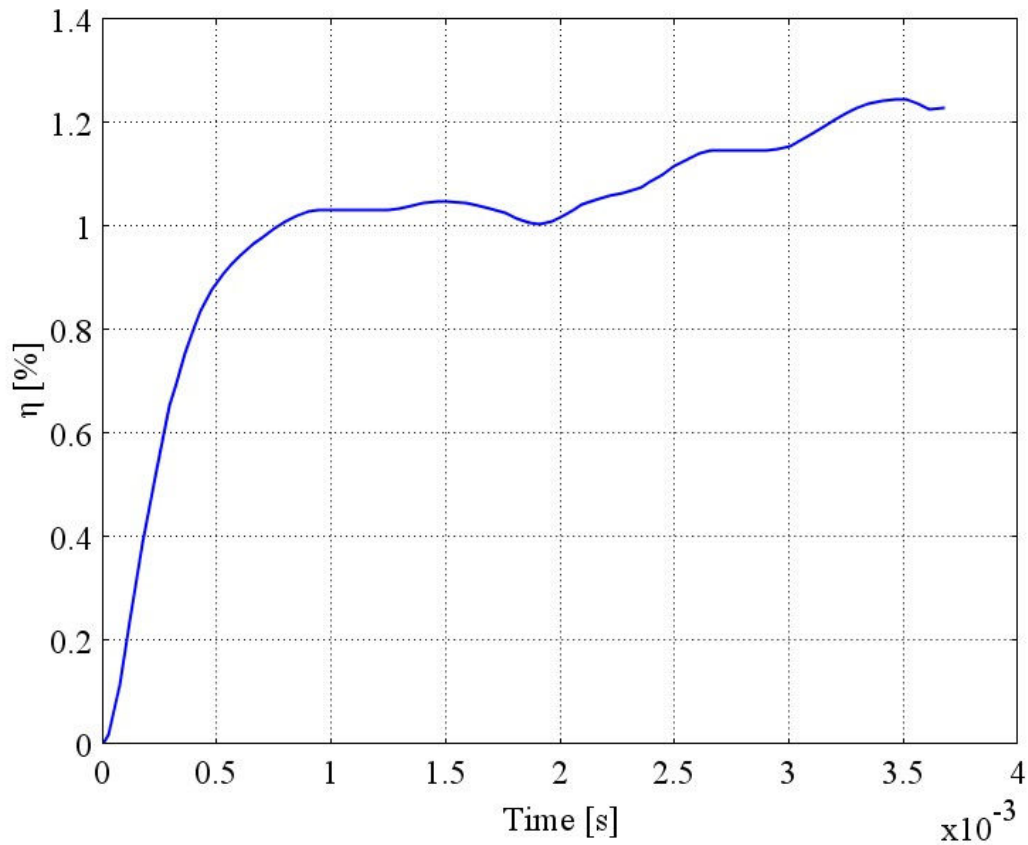
Figure 37: Propulsive efficiency for V Alginolyticus.

The helical trajectory of a single flagellated bacterium was analytically predicted by Keller and Rubinow [21], experimentally observed by Crenshaw [22] and lately, simulated by Hsu and Dillon [19]. For a single rotation of the helical flagellum, Fig. 38 and 39 shows the velocities and positions in the y and z axes respectively. Figure 38 demonstrates that the sinusoidal and out of phase v-w velocities have a one tenth of an amplitude of the longitudinal swimming velocity. In Figure 39, the trajectory of the swimmer is under transitional effects which stem from the time ramp function imposed on the helical rotation. However, there was not enough computing power to wait for the transitional effects to diminish. The helical trajectory of a micro swimmer will be demonstrated in the parametric swimmers section with less transitional effects.
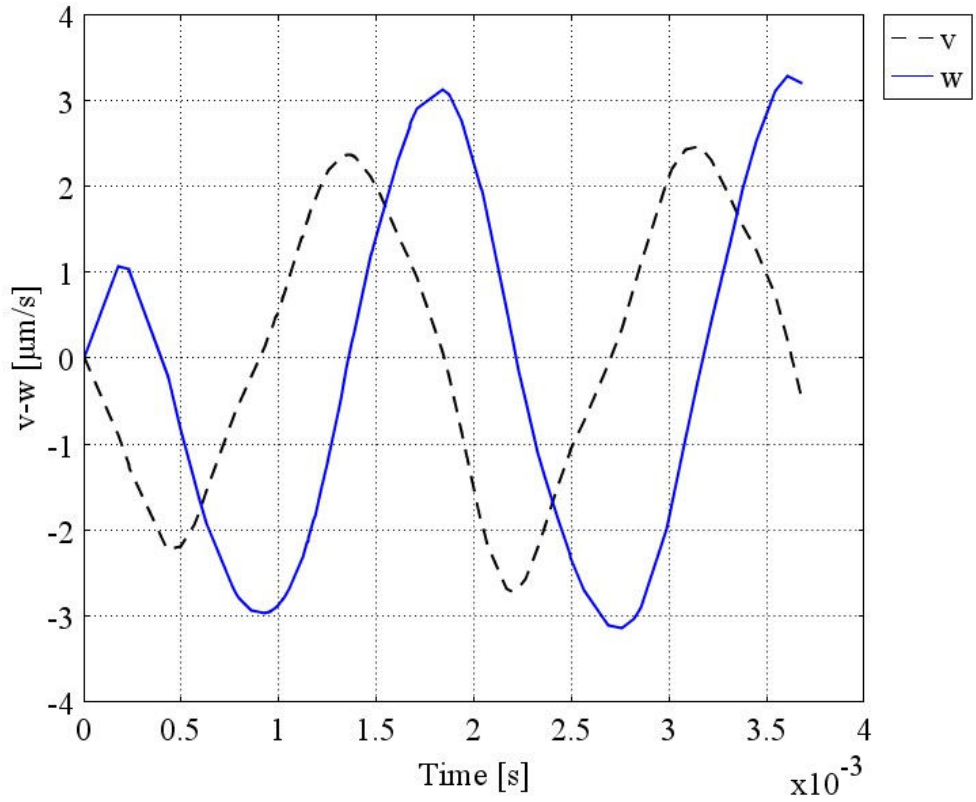
Figure 38: Velocities, *v* and *w* for V Alginolyticus.
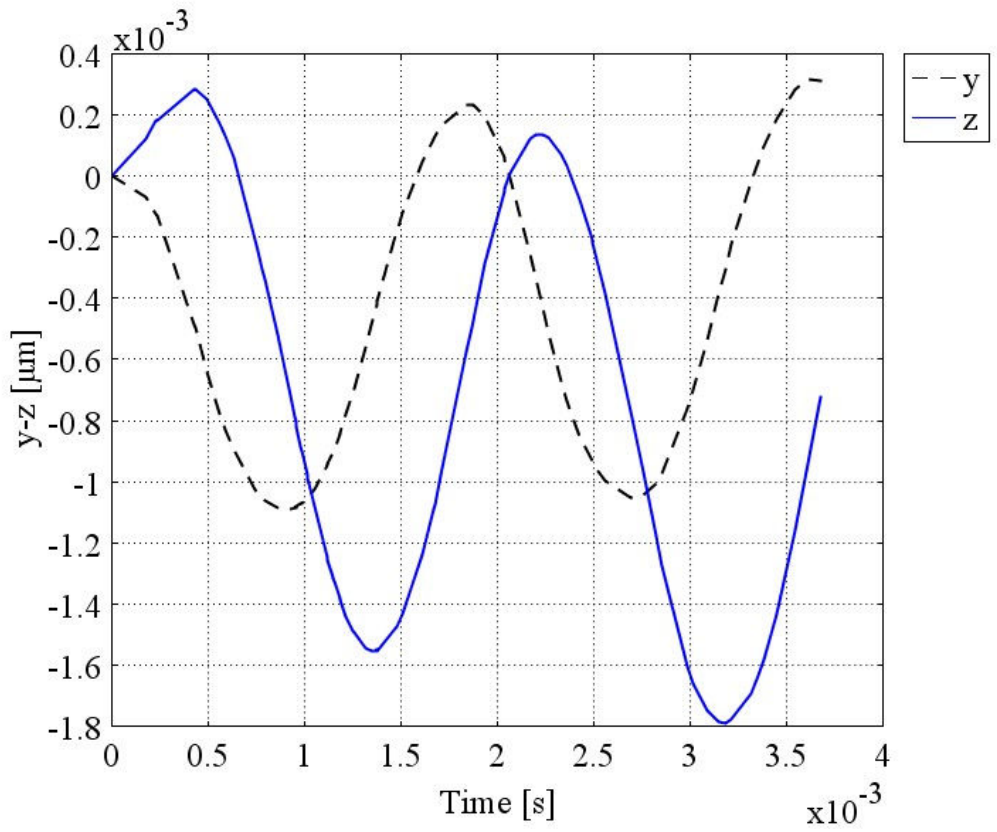
Figure 39: The time dependent position on y-z axes of V Alginolyticus.

The orientation of the swimmer is defined by α and β angles which are plotted as sinusoidal functions of time in Figures 40 and 41. When α angle starts to increase to its maximum value, the swimmer body points out the −y axis rather than the −x axis. For this reason, the swimmer velocity in the −y axis starts to increase with the α angle. Nearly at the same time (t=~0.5 s), α angle and v velocity reach to their maximum and minimum respectively. Around 1.5 s, they reach to minimum and maximum respectively. Therefore, they are sinusoidal functions with approximately 90 degrees of phase difference. The comparison of α angle and y coordinates, in Figures 39 and 40 show that these two functions are in phase. Detail inspections will show that α angle and v velocity do not always exactly have 90 degrees of phase difference. Additionally, α angle and y coordinates are not always exactly in phase. The reason for the mentioned deviations is the effect of lift forces acting on the swimmer. Therefore, the orientation of the swimmer is not the only reason for its perpendicular motion to x axis. Moreover, the transitional effect of the time ramp function can be listed as another reason for deviations.
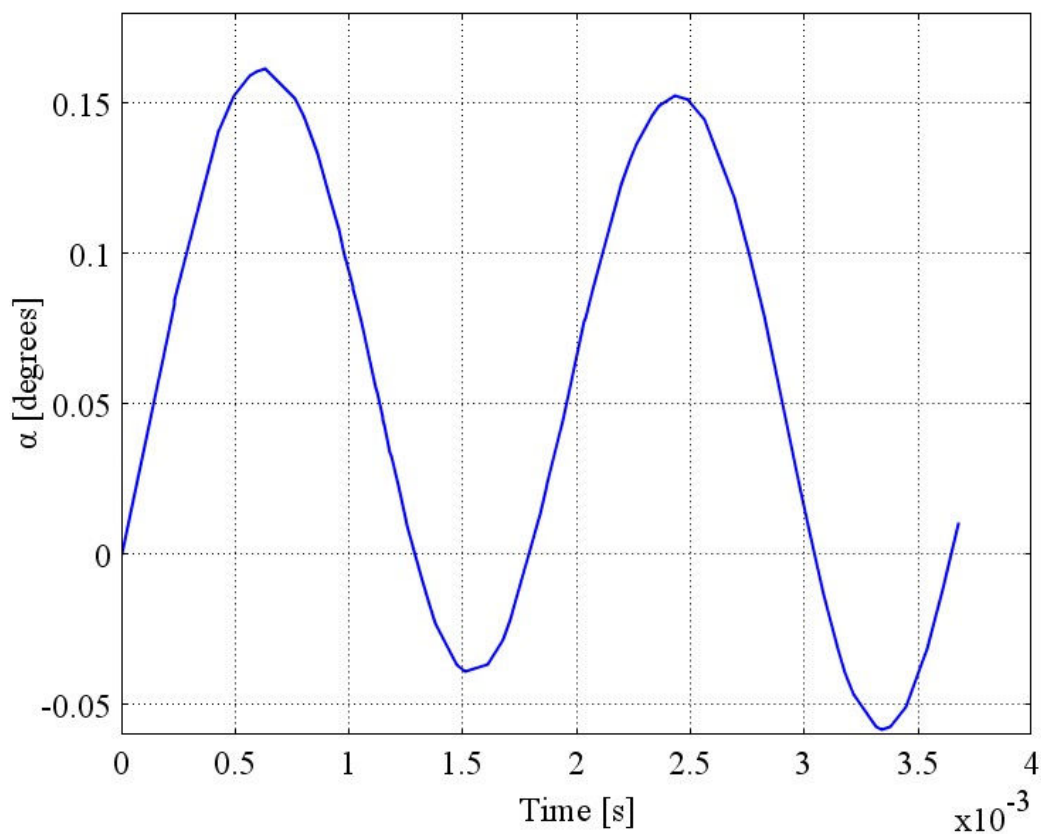
Figure 40: The time dependent α angle of V. Alginolyticus.

The mentioned relation between the α, *v* and *y* values is depicted for the β, *w* and *z* trio in Figures 38, 39 and 41.
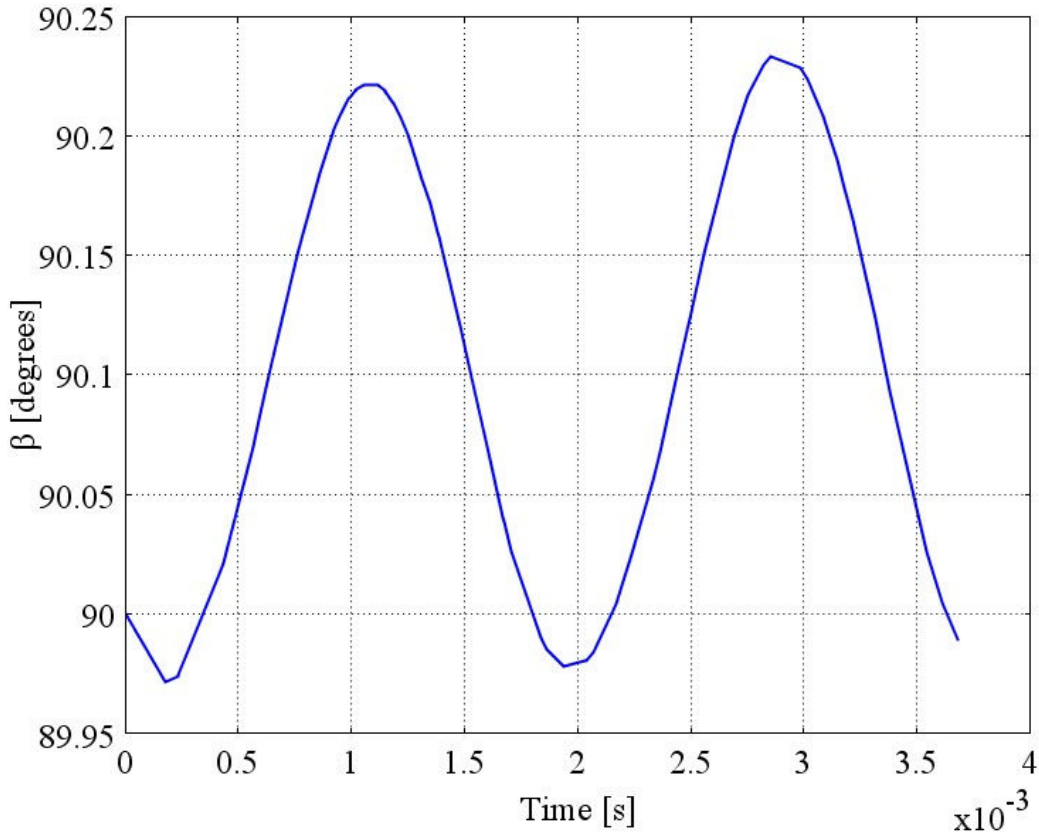
Figure 41: The time dependent β angle of V Alginolyticus.

3.1.2 Comparison of Parametric Results with the Analytical Predictions

Behkam and Sitti [2] formulated the swimming speed of a micro swimmer with variable parameters by conserving the linear and rotational momentum on the longitudinal axis of the swimmer. Equations 68 and 69 are based on the resistive force theory (RFT) and the resistance coefficients for normal and longitudinal directions ($C_{norm,tl}$ and $C_{longt,tl}$) are empirically driven by Johnson and Brokaw for a flagellum with both free ends [2]. However, the body of the swimmer is assumed to be sphere, whereas in this work, the numerical model of the parametric swimmer possesses an ellipsoid body which increases the effective friction area on the swimmer body boundary. This increased boundary area in the numerical models may cause a slower swimming speed.

$$u_{cm} = \frac{L_{tl}\omega_{app}B_0 \sin\phi\cos\phi(C_{norm,tl} - C_{longt,tl})}{L_{tl}(C_{norm,tl}\sin^2\phi + C_{longt,tl} - C_{longt,tl}\sin^2\phi) + 6\pi\sigma R_b\cos\phi} \qquad (68)$$

$$\tan\phi = \frac{2\pi}{\lambda}B_0 \qquad (69)$$

Every parameter used in the parametric models is directly used in the Equations 68 and 69, except one which is the maximum helical tail amplitude B_0. This value is calculated by using Eq. 32 with the input $m=0.6$. As a result, the maximum amplitude of the tail used the numeric model is multiplied with the factor 0.5128 to give the effective maximum amplitude.

3.2 Verification of the Parametric Models

After setting the parametric model up, the reference model with parameters ω_{app}=20 Hz, L_{tl}=2 μm, λ=2 μm, B_0= 0.1 μm, runs for checking if the generic swimmer model is working properly.

First of all, the rotation of the helix tail in the X axis is verified by plotting the time-dependent tail tip position with respect to Y and Z axes in Fig. 42. The tip point starts its deformation from the origin with an increasing magnitude as time goes by. The linear time ramp function makes the tail rotation direction visible in this plot. The rotation direction in Fig. 42 is counter clockwise (CCW) which is also validated by the observational data available in the literature [9, 12, 13].
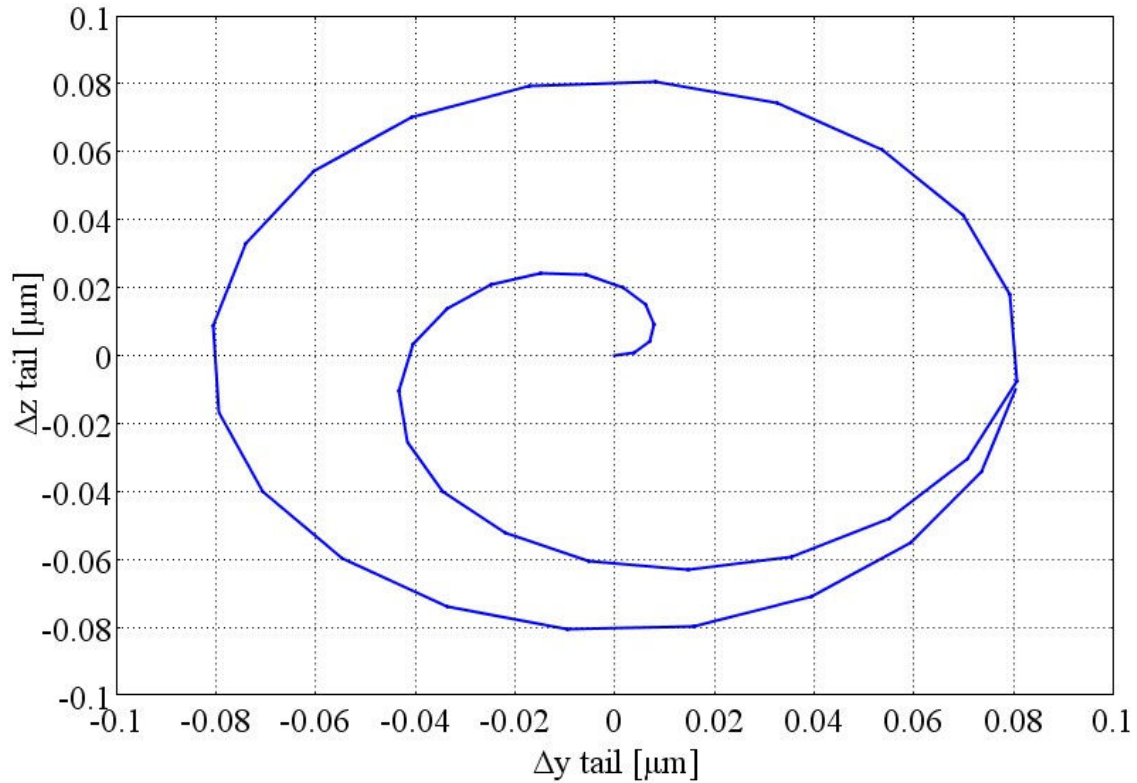
Figure 42: The time dependent tail tip deformation of the reference swimmer in y-z axes.

The rotation of the tail is also verified by 3D Figures 43-45, which show the smooth transition between the swimmer body and the tail. This smooth transition was previously observed as a proximal hook [13]. The helix tail creates pressure differentials around it and these differentials can be tracked by the colored pressure distribution and the normalized fluid velocity vectors. In Fig. 43-45, the high and low pressure zones are represented with red and blue colors respectively. The figures in temporal order show that the pressure zones move to the tail tip of the swimmer in time. When the high pressure zone reaches at the back, the new low pressure zone comes into scene.

In addition to pressure zones, the fluid velocity vectors on the swimmer body give clues about the swimmer motion. By looking at the velocity vectors around the swimmer head in the first frame (t=0.05 s), it can be inferred that the swimmer is rotating its body to upwards. Then it rotates back to its horizontal orientation and in the last frame, it swims mostly in the longitudinal axis.
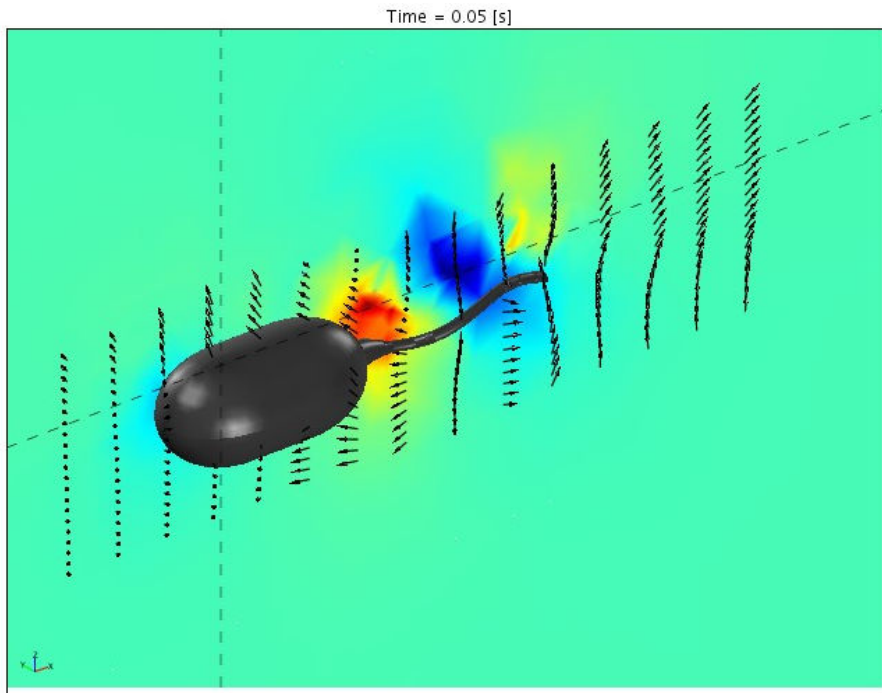
Figure 43: A snap shot from the motion of the reference swimmer at *t*=0.05 s.
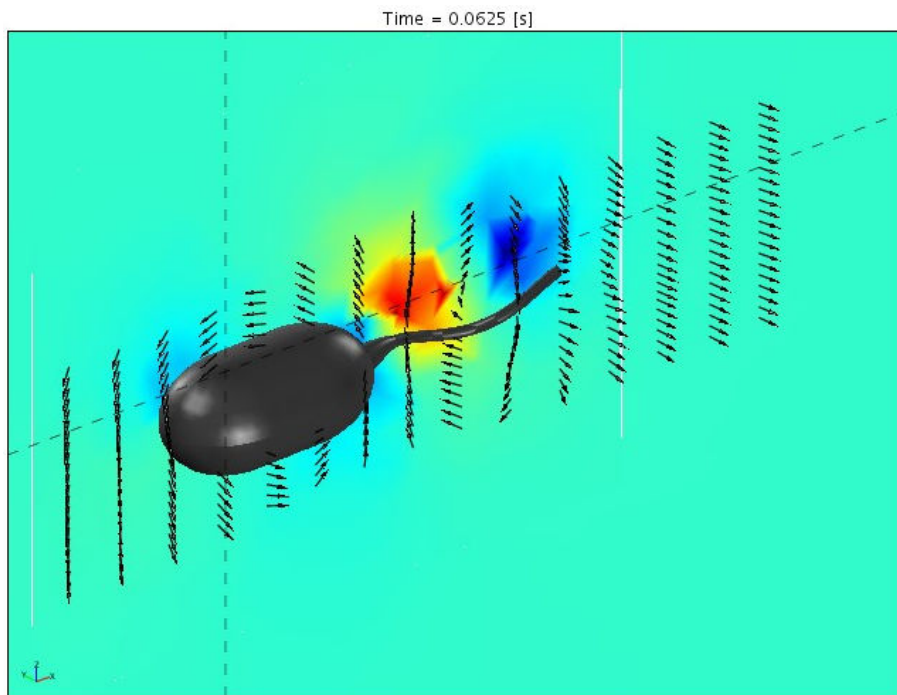
Figure 44: A snap shot from the motion of the reference swimmer at *t*=0.0625 s.
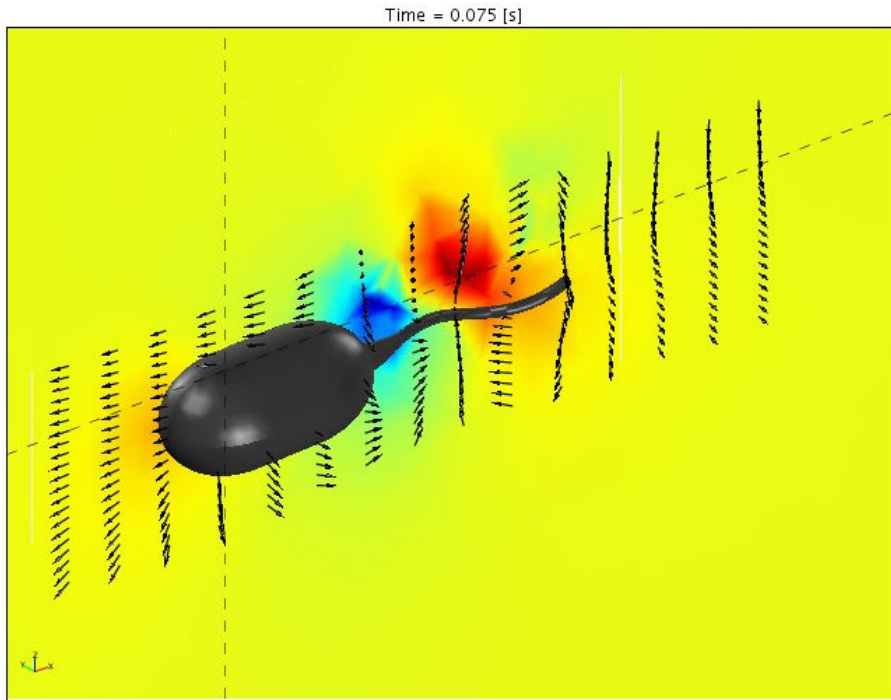
Figure 45: A snap shot from the motion of the reference swimmer at *t*=0.075 s.

The helix tail rotation in the fluid generates a reaction torque from the fluid. The fluid reaction distorts the zero torque balance on the swimmer and the swimmer body becomes affected by the reaction torque coming from the helix tail. Therefore, the helix tail and swimmer body rotates in opposite directions to create zero net torque on the swimmer. Figures 46 and 47 shows that as the applied tail rotation is increased by the time ramp function, the counter rotation of the body increases accordingly.

The numerically found torque and drag on the swimmer body is compared against the values calculated according to the methodology that Chattopadhyay put forward [26]. By using the torque and force constants presented in Equations 65 and 67, the Equations 64 and 66 output the torque and force predictions based on the observational data and resistive force theory (RFT). The one-to-one comparisons between numerical and analytical results for torque and force are depicted in Figures 48 and 49. The numeric result for the torque is calculated to be eight times the magnitude of the analytical prediction whereas the numerically calculated drag force overshoots the analytical prediction by 36%.
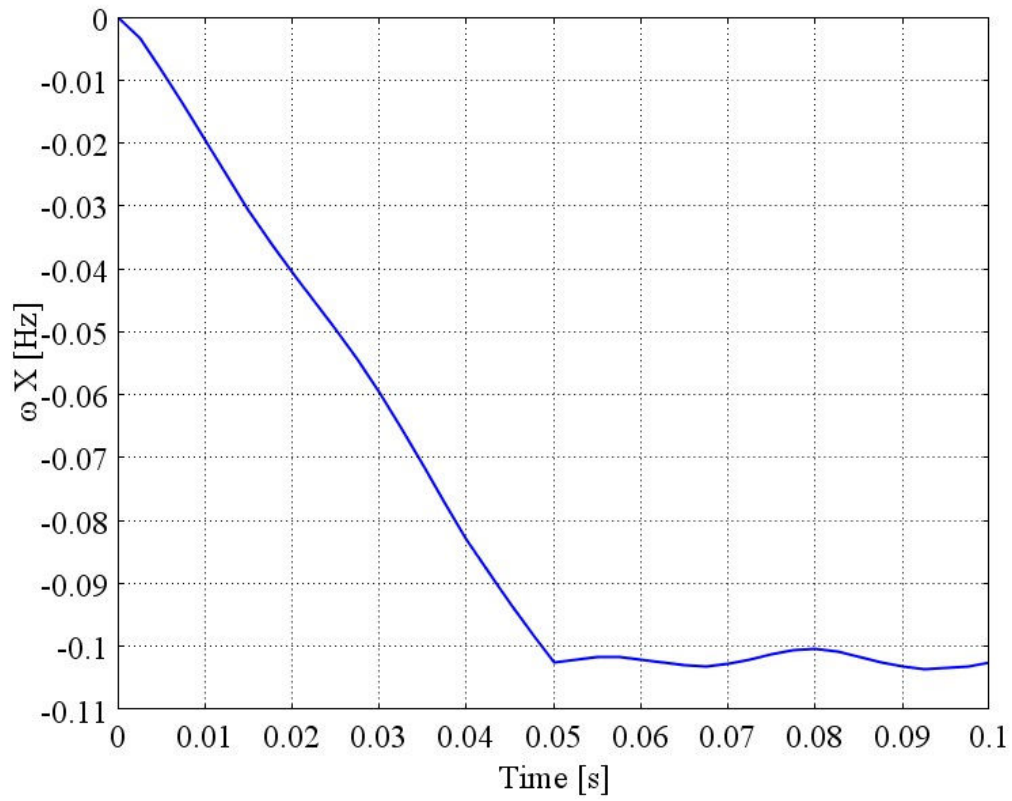
Figure 46: The time dependent body rotation rate for the reference swimmer.
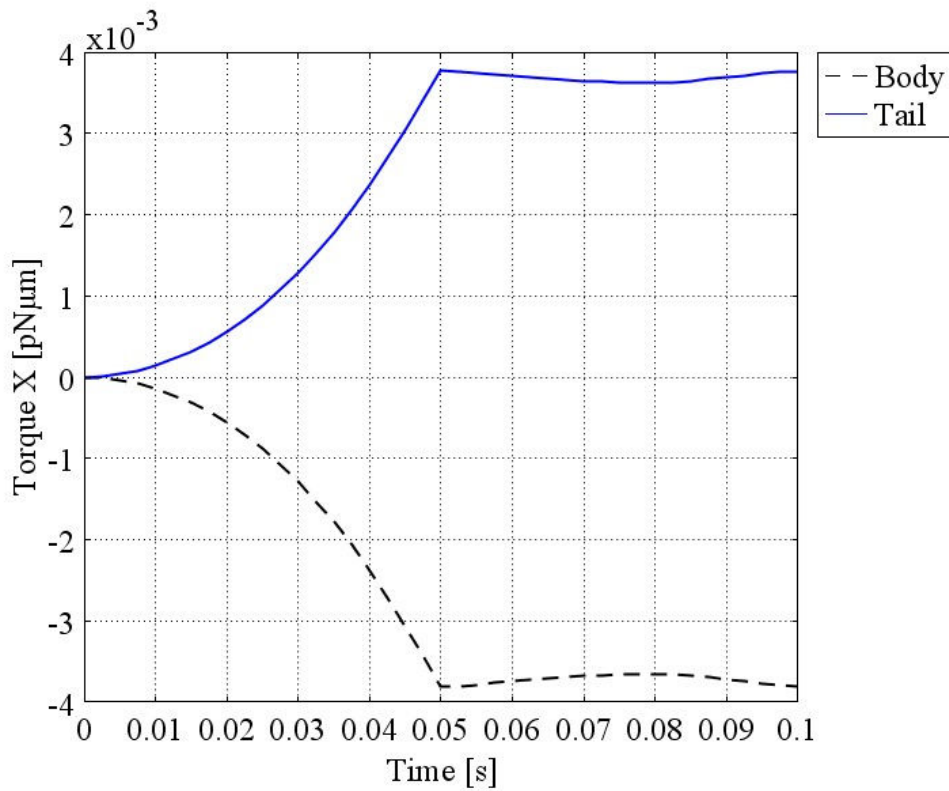
Figure 47: Time dependent body and tail torques of the reference swimmer.
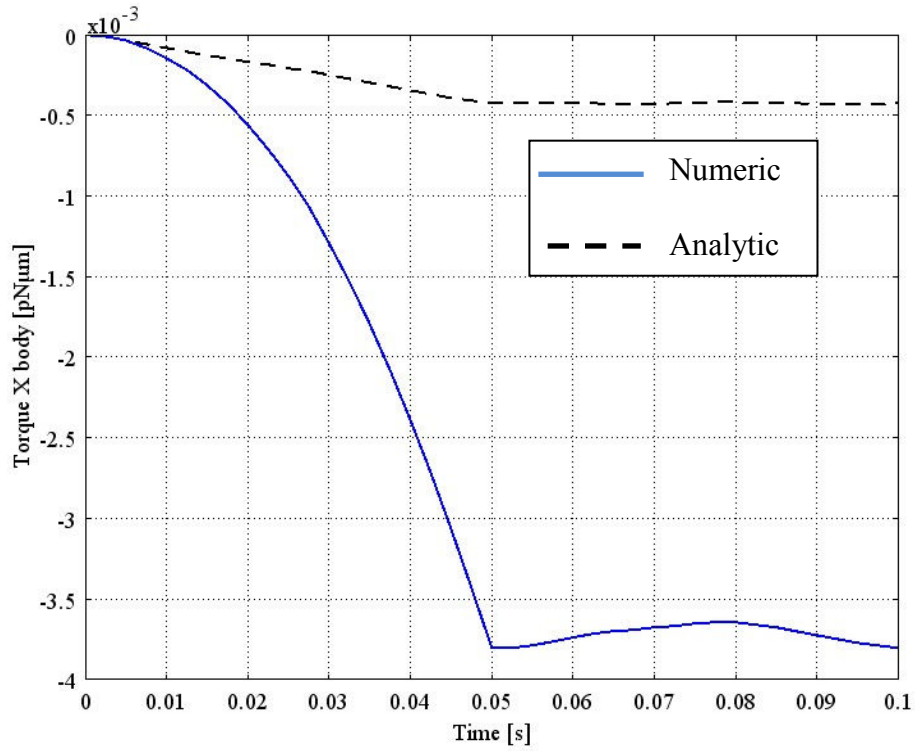
Figure 48: Numerical result and analytical prediction of the body torque for the reference swimmer.
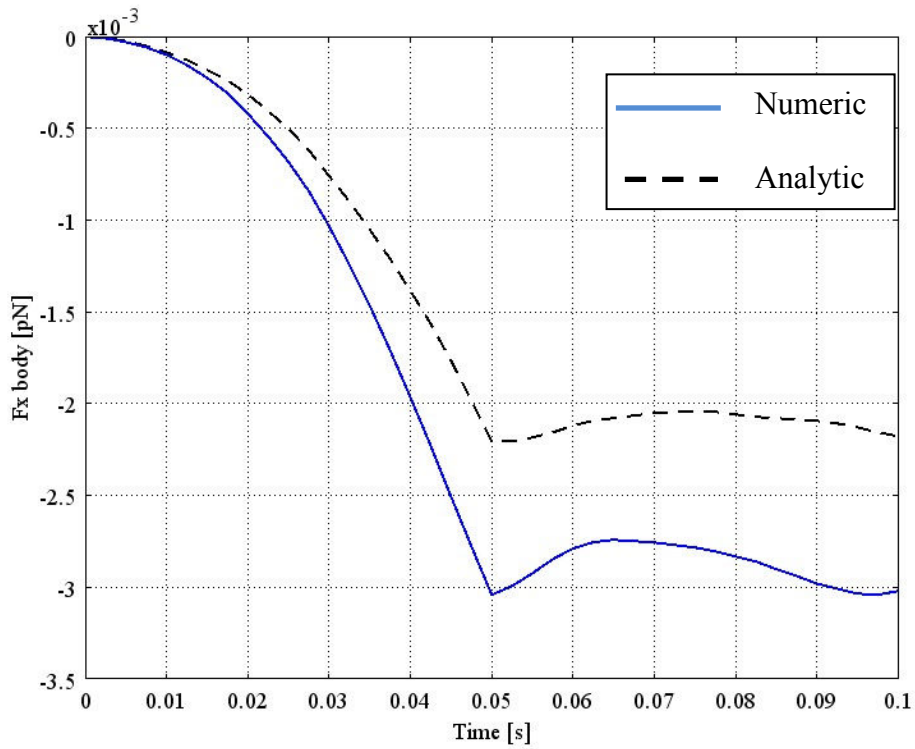
Figure 49: The numeric result and analytical prediction of body drag for the reference swimmer.

In Figure 50, the net force directed in the -x axis moves the swimmer with an average speed of 0.15 μm/s. In Figure 51, there is a plot of sinusoidal velocities in y-z axes nearly at the same magnitude with the swimming speed and have a phase difference approximately 90 degrees. The magnitudes of the *v-w* velocities show that the helical trajectory of this parametric swimmer has a larger radius of curvature than the V. Alginolyticus.
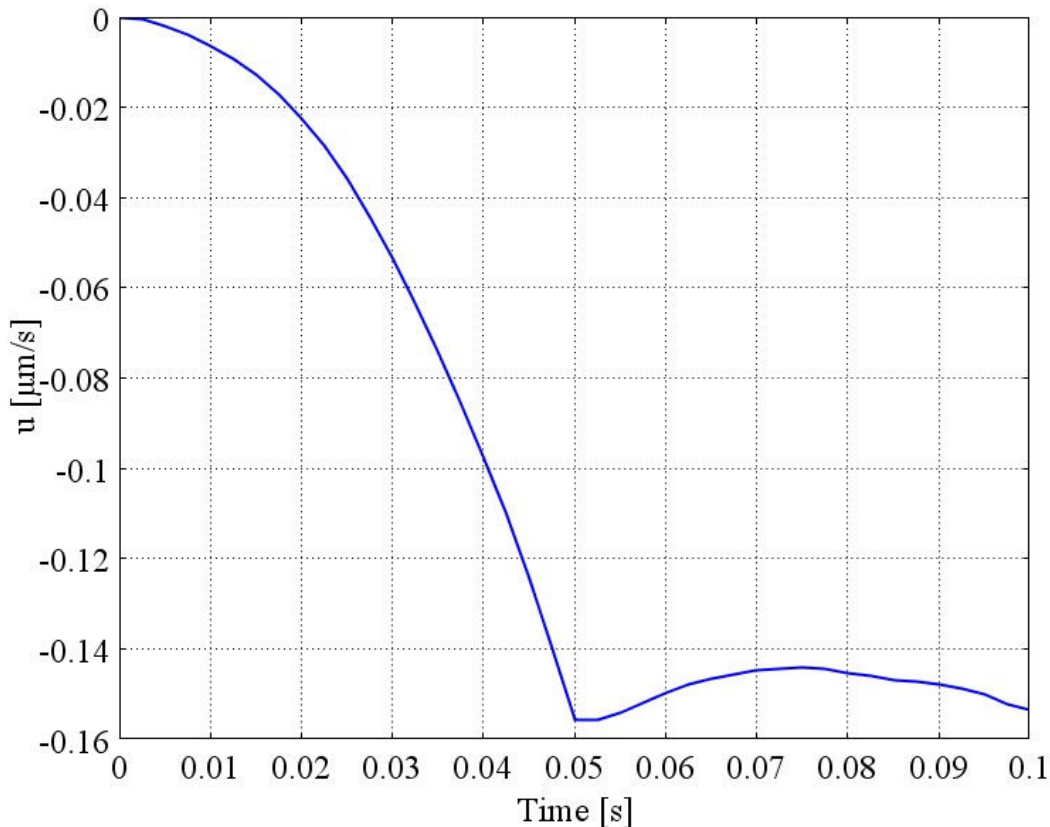
Figure 50: Time dependent swimming velocity of the reference swimmer.

The position coordinates which are the time integrals of the velocities *v* and *w* in Fig. 51 are depicted in Fig. 52. Both velocity and position plots show a symmetric behavior around *y*=0 line which means the net displacement in either *y* or *z* axis is zero.

The main reason of this clear helical path is the rotations of the swimmer around *y* and *z* axes. Their time dependent plot, Fig. 53shows that the rotations around *y* and *z* axes have nearly the same magnitude with the rotation of the swimmer head. Moreover, they reflect the phase shift between the *v-w* velocities and *y-z* positions.
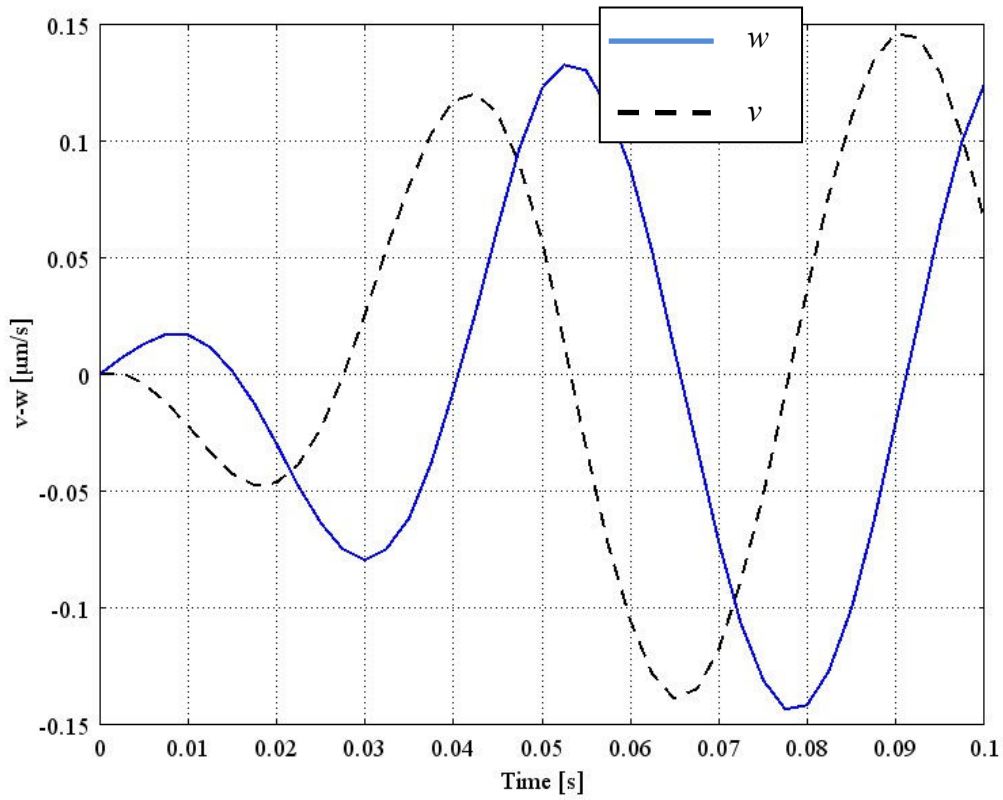
Figure 51: Time dependent *v-w* velocities of the reference swimmer.
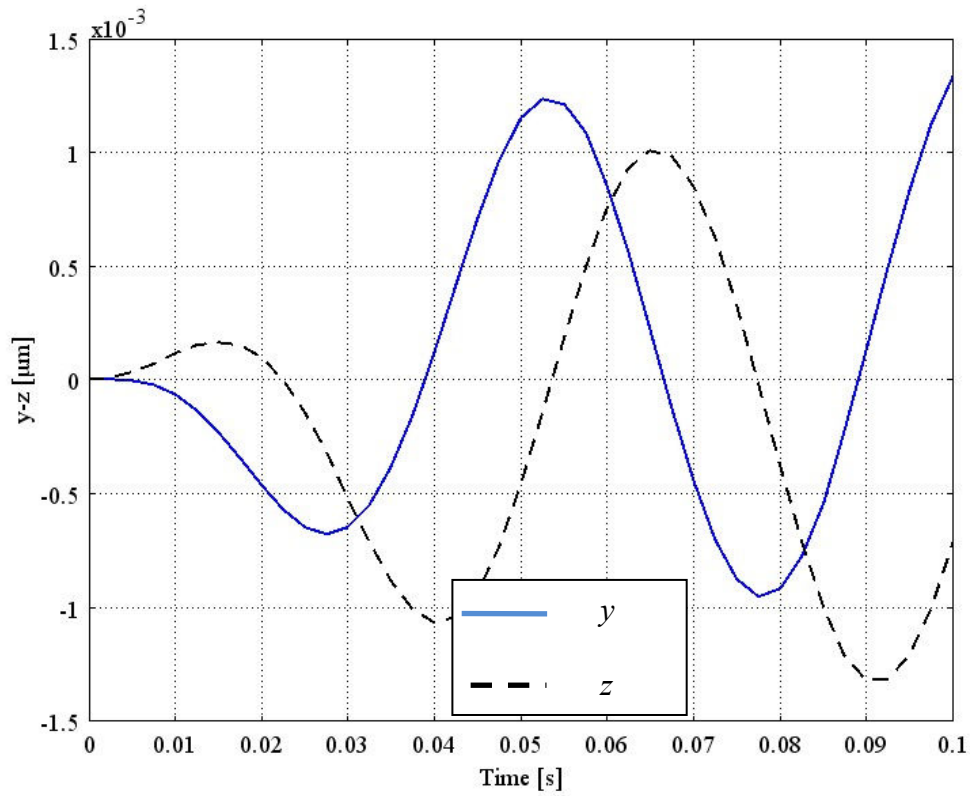
Figure 52: Time dependent position of the reference swimmer on y-z axes.
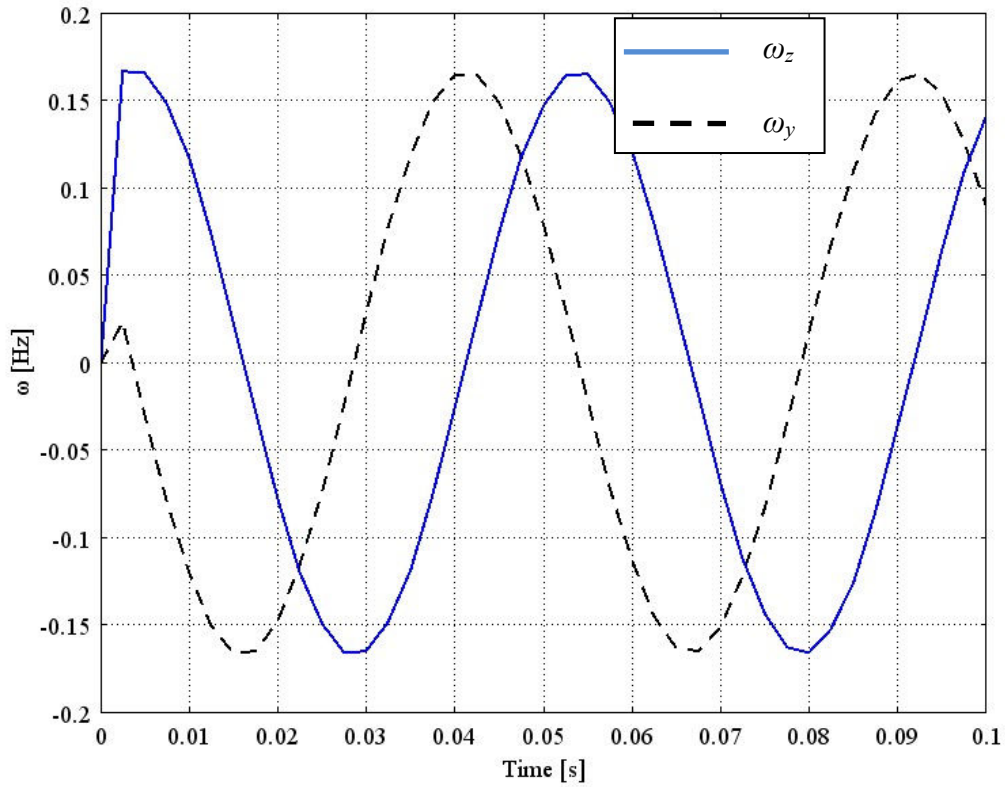
Figure 53: Time dependent angular velocities in y-z axes for the reference swimmer.

The effect of the swimmer rotations about *y-z* axes can be tracked from the orientation of the swimmer which is expressed with α and β angles. They are plotted in Figures 54 and 55. They reflect the same phase difference between the angular velocities in *y-z* axes, *v-w* velocities and *y-z* positions.
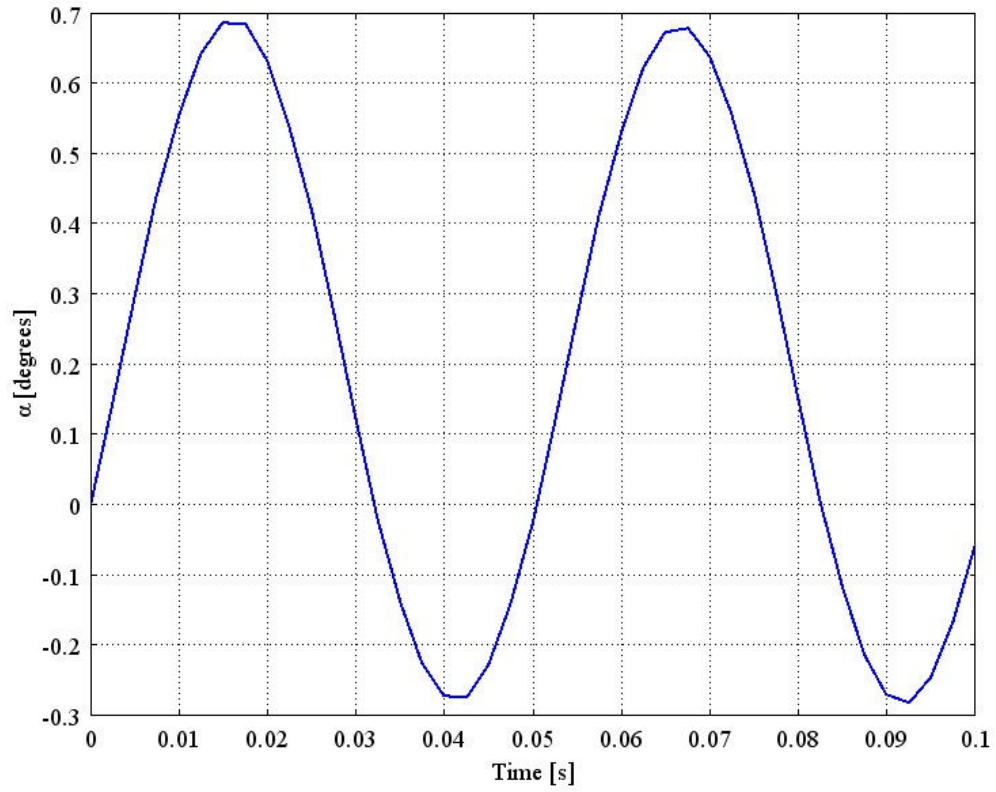
Figure 54: The time dependent α angle of reference swimmer.
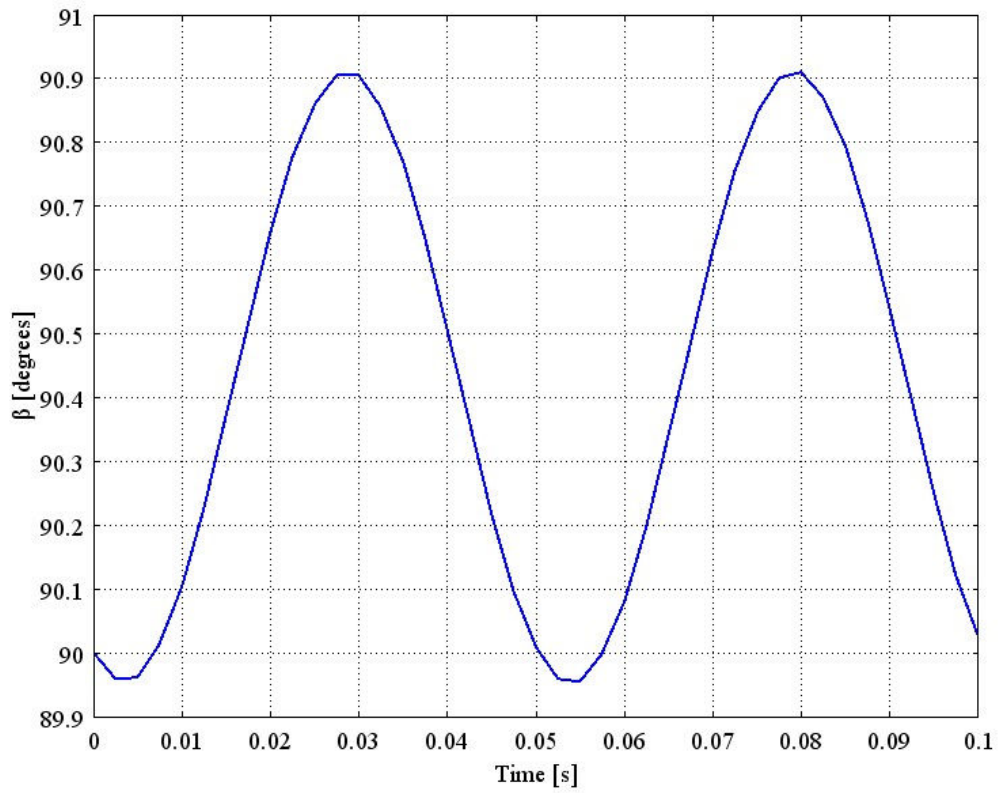
Figure 55: The time dependent β angle of reference swimmer.

3.3 Parametric Results

3.3.1   The Interpretation of Parametric Results

3.3.1.1 Swimming velocity in the *x* axis

The parametric results are presented in log-log plots to show the order to correlations clearly. Moreover, the swimming speeds in the longitudinal axis of the micro channel are compared with the analytical prediction of Behkam and Sitti [2].In Figure 56, a linear correlation between the swimming speed and rotation frequency is depicted. Both the linear correlation and swimming speed values are validated by the analytical prediction. As an observational validation, Magariyama etal [24] reported a roughly linear correlation between the swimming speed and helical tail rotation rate. In Figure 56, applied rotation frequency is the input parameter, instead of effective rotation rate with respect to fluid. However, the difference between these values is low enough to assume that they are the same. In Section 3.2, the ratio between the applied rotation frequency and body rotation frequency was 20/0.1 (Hz) = 200. Therefore, the contribution of body rotation in the calculation of effective tail rotation is negligible and it is assumed that $\omega_{app} \sim= \omega_{eff}$.
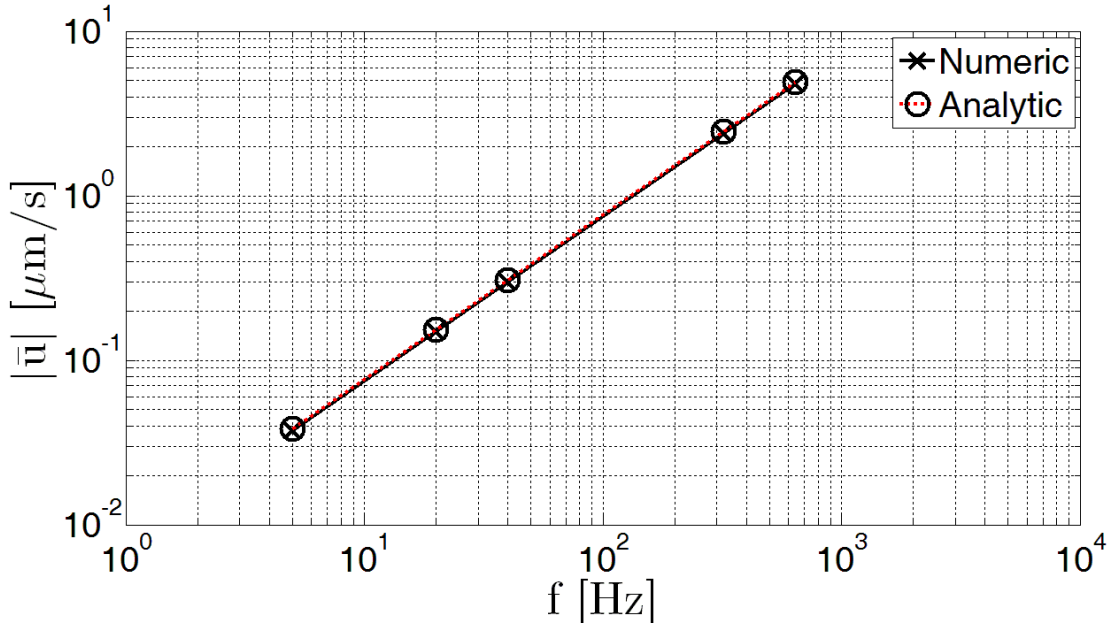
Figure 56: The numeric and analytical results for the frequency dependency of swimming speed.

In Figure 57, there is linear correlation between the swimming speed and the axial length of the helical tail. The behavior of change with input parameter is validated with the analytical prediction. However, the numeric results overshoot the analytical predictions with 20-25%. Magariyama and co writers [24] report that there is a positive correlation between swimming speed and axial length of flagellum for values smaller than 5 μm. However, the order of correlation is not clearly depicted in the figure of work. For the reference case with 2 μm axial length of helical tail, the numeric result underscores the analytical prediction which was expected in Section 3.2. Therefore, the results of larger input values can be outliers because of the lack of mesh quality.
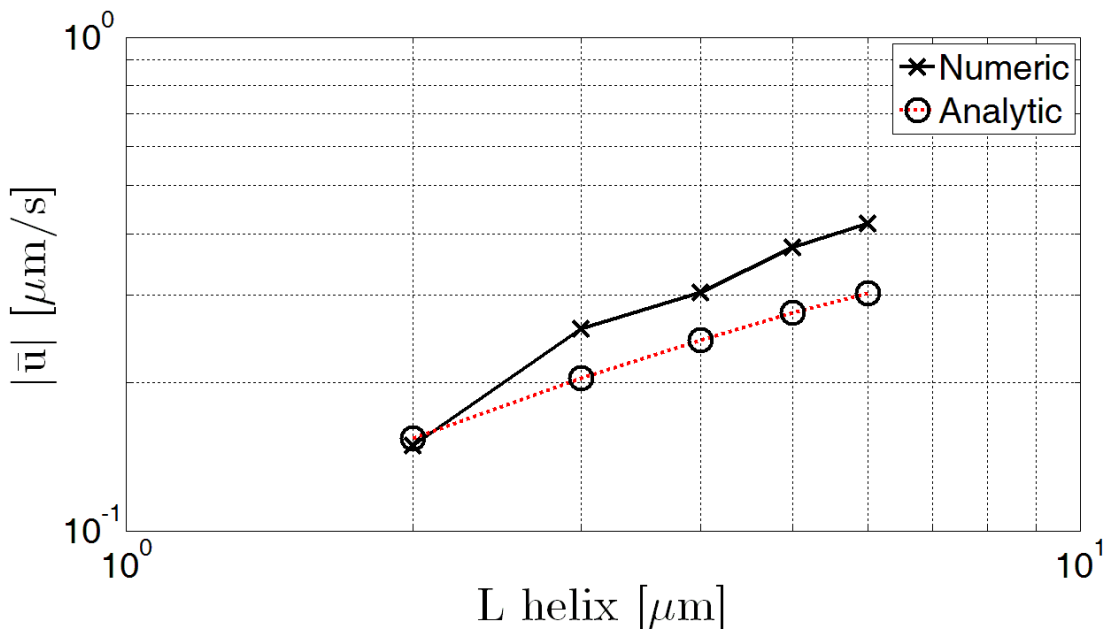
Figure 57: The numeric and analytical results for the dependency of swimming speed on the axial length of helix.

The effect of the helical wave length on the swimming speed is depicted in Fig. 59 with an inverse proportionality. This correlation and the swimming speed for each input are validated by the analytical prediction. Moreover, observational results [24] also validate that swimming speed is inversely proportional for helical wavelengths larger than 2 μm.

There is a quadratic dependence of swimming speed on the input parameter of maximum helical amplitude. Figure 59 shows this quadratic dependence by also demonstrating the approach to a horizontal asymptote for input values larger than 0.2 μm. This asymptotic behavior is the result of approaching to the limiting wave speed of the tail ($\omega_{app}.\lambda$). The behavior is validated by the analytical prediction and there is strong agreement

for the input values smaller than 0.4 µm. The deviation for input 0.4 µm stems from the asymptotic behavior mentioned above and the increasing mesh deformation specified on the tail geometry.
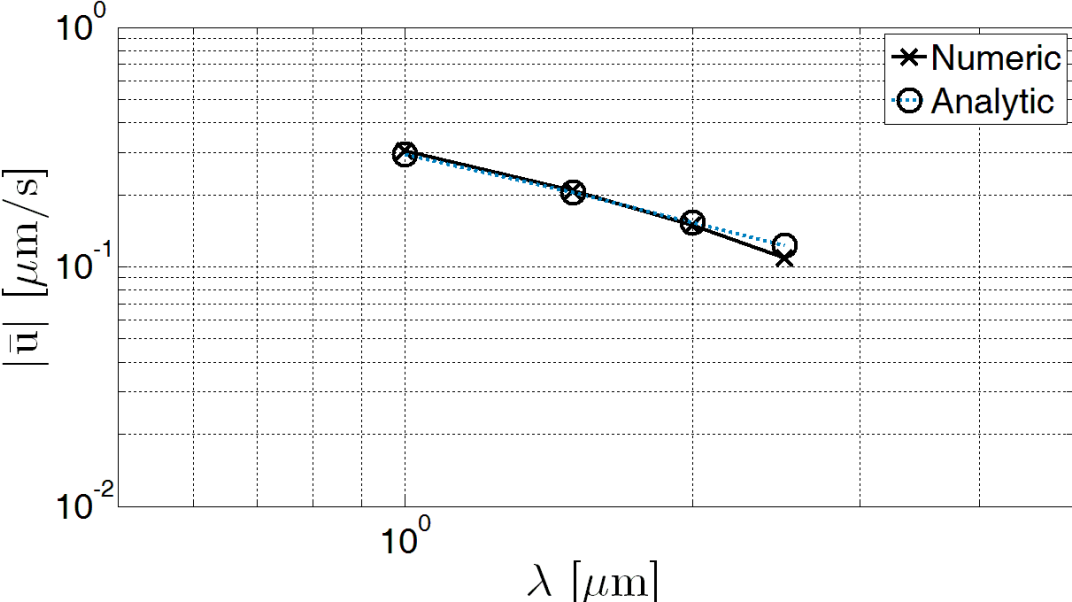
Figure 58: The numeric and analytical results for the dependency of swimming speed on the wavelength of the helical tail.
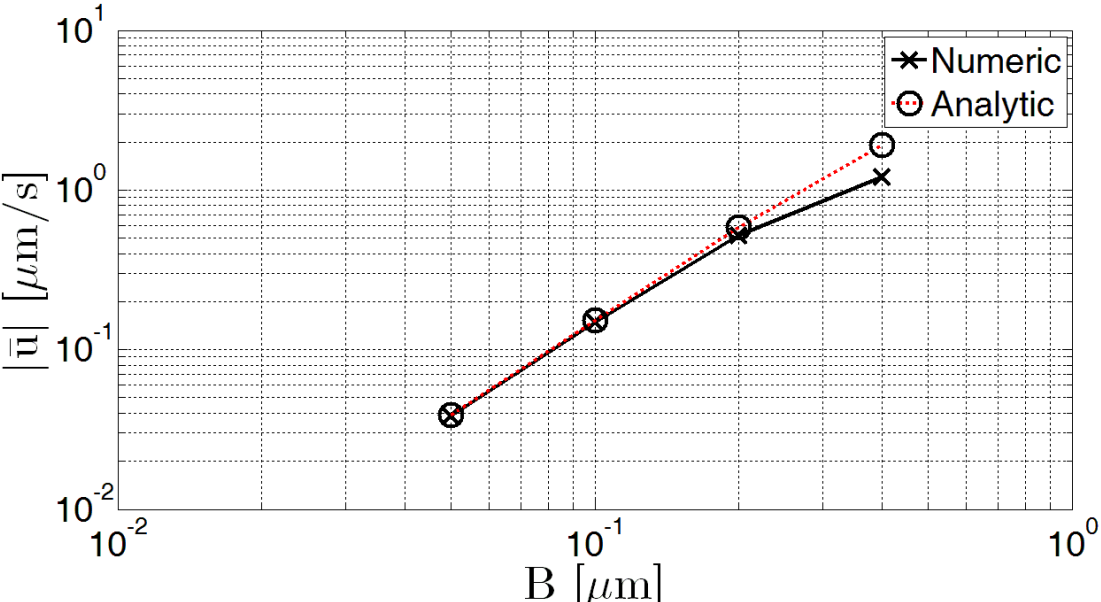
Figure 59: The numeric and analytical results for the dependency of swimming speed on the maximum amplitude of the helical tail.

3.3.1.2 Swimming velocities in the *y-z* axes

Swimming speeds perpendicular to the longitudinal axis of the micro channel, *v-w* are time dependent, sinusoidal waveforms, as depicted for the reference swimmer in Fig. 51. These waveforms are quantified and analyzed with their amplitudes.

There is a first order dependence of their amplitude on the rotation rate of the helical tail. Moreover, the amplitudes for *v* and *w* velocities are exactly the same for all input values of frequency. This means that the helical trajectory of the swimmer is symmetric in both *xy* and *xz* planes.

The axial length of the tail has a linear correlation with the amplitudes of *v* and *w* velocities. This linear correlation cannot be observed only for the axial length 4 μm. The parametric results are not verified to be independent of mesh quality. Therefore, this maximum point at axial length 4 μm, can either reflect a pure mesh quality or it reflects the most efficient axial length of helical tail for swimming sideways. In the observational work of Magariyama [24], the swimming speed in the longitudinal direction is maximized for a length of helical tail. This value is around 3 μm. So, there can also be an optimized value for swimming sideways. Moreover, the symmetry between *v* and *w* velocities starts to diminish for the values closer to 4 μm; and for the values closer to 2 μm and 6 μm, the symmetry is achieved.
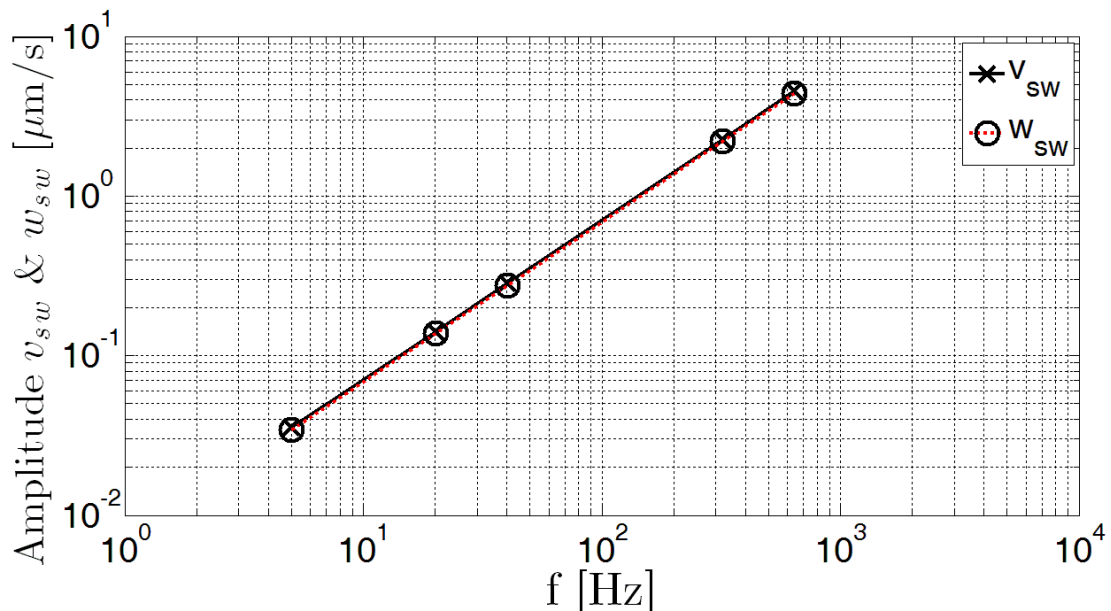
Figure 60: The numeric results for the dependency of *v-w* velocities on the rotation rate of the helical tail.
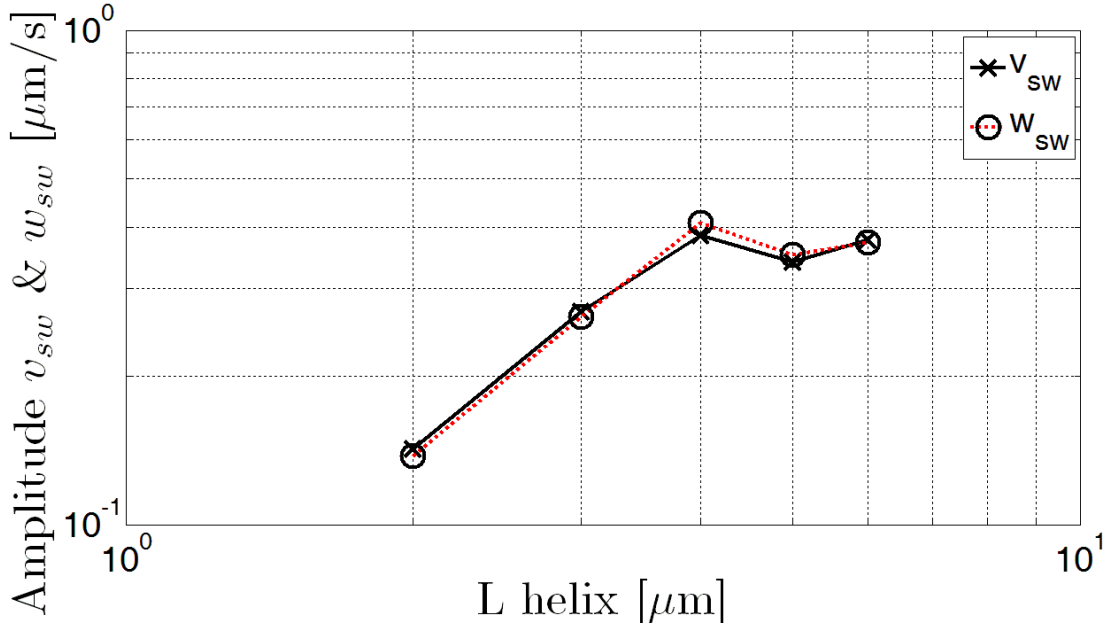
Figure 61: The numeric results for the dependency of *v-w* velocities on the axial length of the helical tail.

Figure 62 demonstrates the quadratic correlation between the amplitudes of v-w velocities and wavelength of the helical tail. The correlation between the wavelength of the helical tail and the swimming speed in the longitudinal axis was demonstrated to be a linear one in Fig. 58. Therefore, by decreasing the wave number on a constant length of helical tail, the micro swimmer can be maneuvered in *xy* and *xz* planes. An increasing wave number on a helical tail would lead to a trajectory which is more of a straight line. The input value 1.5 µm is a potential outlier. Moreover, the symmetry between the *v-w* is achieved better for higher values of wavelength values. This may stem from the lack of precision to resolve the smaller amplitudes of *v-w* velocities.

In Figure 63, a linear correlation between the amplitude of *v-w* velocities and maximum amplitude of the helical tail is depicted. This correlation was depicted as second order one for the swimming speed in the longitudinal axis in Fig. 59. This means that as the maximum amplitude of the helical tail increases, the swimmer motion in the longitudinal axis dominates the motion in the axes perpendicular to it. Moreover, the amplitude of velocity *v* slightly dominates *w* for the amplitude 0.05 µm. These velocities have exactly the same amplitude for 0.1 µm input. For the input values larger than 0.1 µm, the amplitude of *w* starts to dominate *v* more and more.
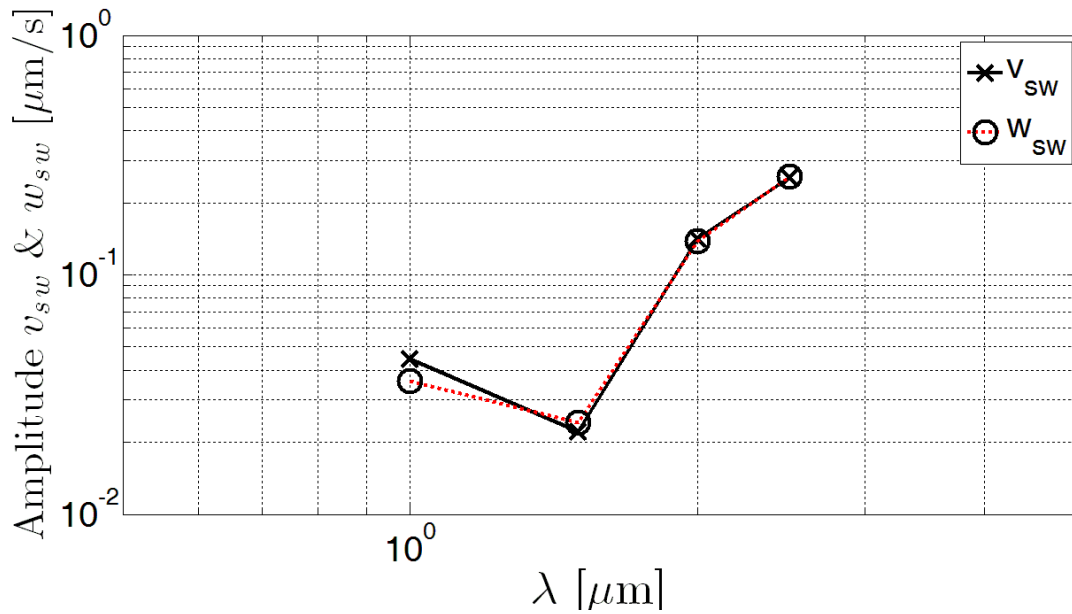
Figure 62: The numeric results for the dependency of *v-w* velocities on the wavelength of the helical tail.
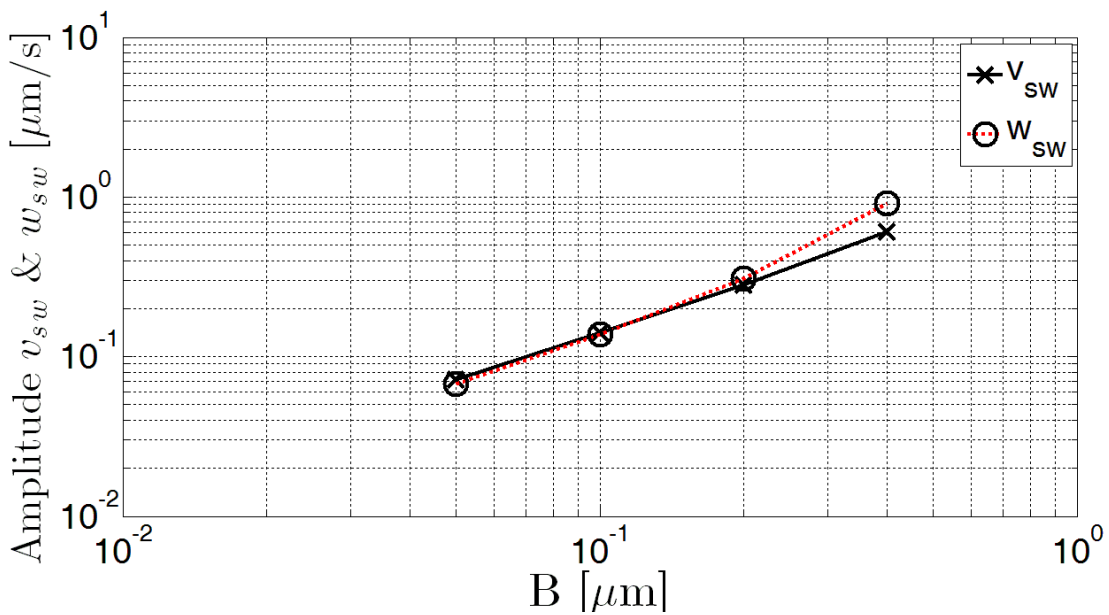
Figure 63: The numeric results for the dependency of *v-w* velocities on the maximum amplitude of the helical tail.

3.3.1.3 Swimmer rotations in the *y-z* axes

In addition to translational motions of the swimmer in the space frame, the full body motion of the swimmer is also expressed with the rotation of it in *y-z* axes. The rotations in *y-z*

axes are sinusoidal functions which are quantified and parametrically analyzed with their amplitudes.

Figure 64 shows the linear correlation between the rotation rate of the helical tail and the rotate rate amplitude of the swimmer in *y-z* axes. The individual amplitudes of rotations exactly match for the all input values of tail rotation rates.

The rotation rates of the swimmer decreases with an increasing axial length of the helical tail. This shows that an increasing number of waves provided by an increasing length of helical tail decrease the body rotations. From the Figures 61 and 65, it can be inferred that, the increasing velocities *v* and *w* are not a result of body rotation in *y* and *z* axes. The increasing length of the helical tail may introduce larger net forces in the *y* and *z* axes as sinusoidal functions. At the same time, it stabilizes the swimmer motion by introducing smaller torques in the *y* and *z* axes and creating a swimming trajectory more of a straight line rather than a helix.
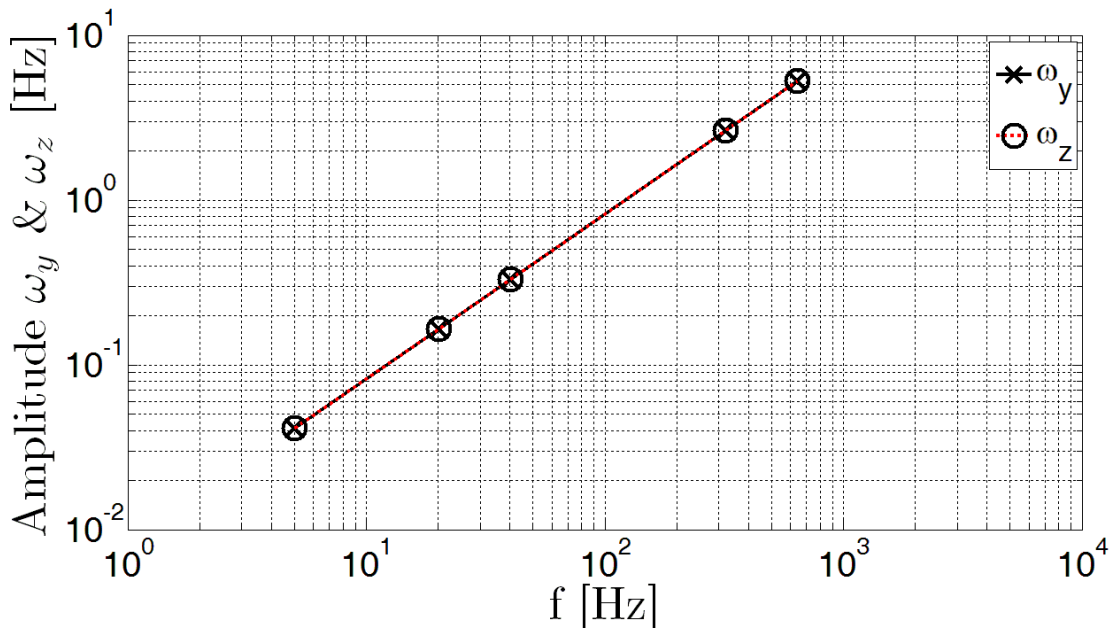
Figure 64: The numeric results for the dependency of *y-z* rotations on the rotation rate of the helical tail.

The linear correlation between the wavelength of the helical tail and the rotation amplitudes of the swimmer in *y-z* axes is depicted in Fig. 66. The quadratic dependence of *v-w* velocities on the wavelength of the helical tail (Fig. 62) can be explained by the increasing rotations of the swimmer with the increasing wavelength. So, it can be concluded that decreasing wave numbers on a helical tail induces higher torques to rotate the swimmer.
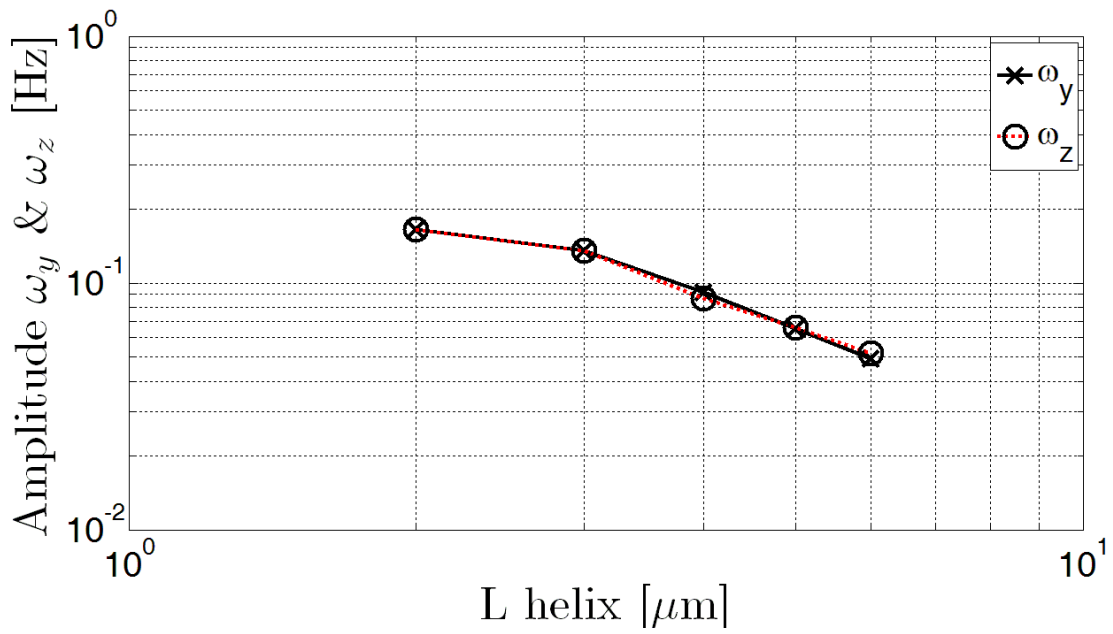
Figure 65: The numeric results for the dependency of *y-z* rotations on the axial length of the helical tail.
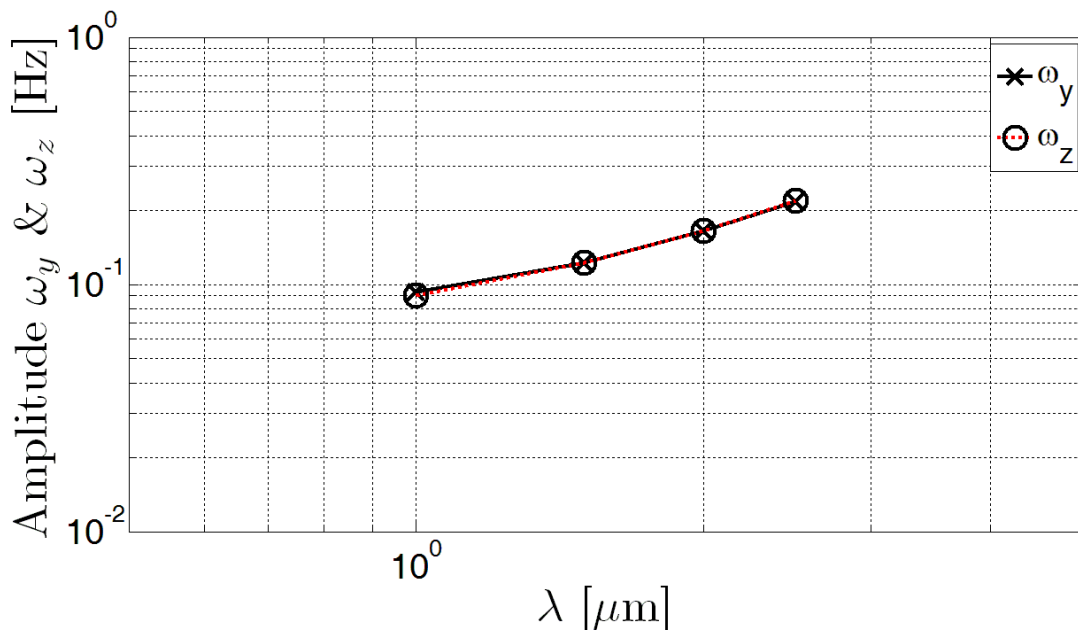
Figure 66: The numeric results for the dependency of *y-z* rotations on the wavelength of the helical tail.

Lastly, Figure 67 shows that the amplitudes of the swimmer rotations are linear functions of maximum tail amplitude. The amplitude values of each rotation for a particular input value matches exactly. As presented in Fig. 63, there was a quadratic relation between

the maximum tail amplitude and *v-w* velocities. Therefore, larger maximum tail amplitude leads the way of higher net forces and torques in *y-z* axes. However, the increase in the net forces is larger than torques. This enables the swimmer to have a helical trajectory with larger radius but at the same time, does not enforce larger rotations which change the orientation of the micro swimmer.
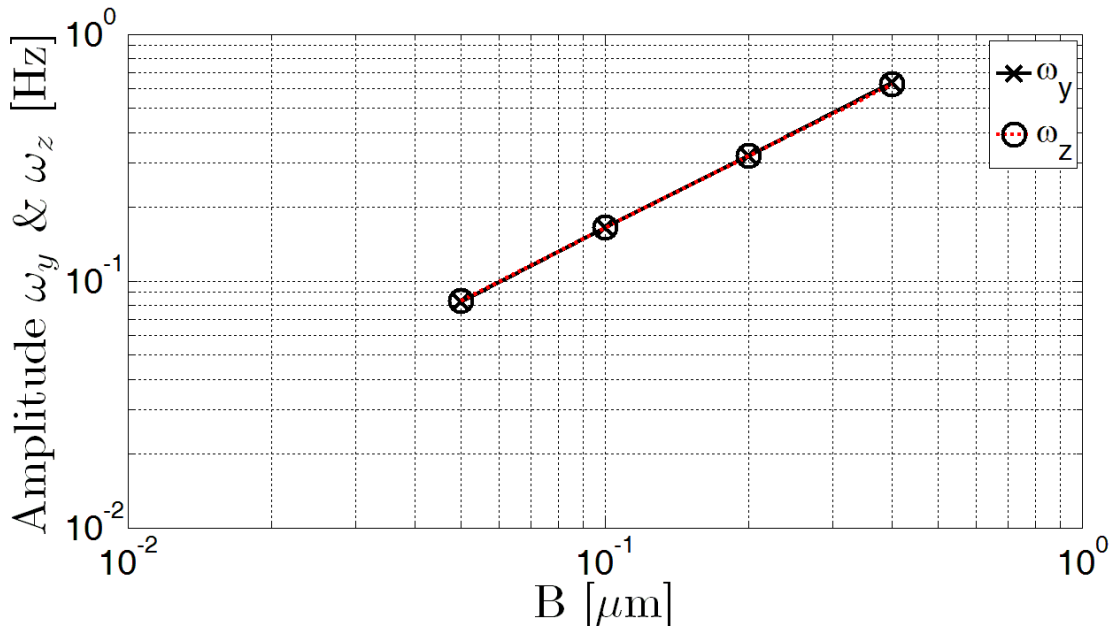
Figure 67: The numeric results for the dependency of *y-z* rotations on the maximum amplitude of the helical tail.

3.3.1.4 Power requirement

The power requirement of the micro swimmer is quantified and parametrically analyzed by time averaging the absolute power required to actuate the helical tail for a full rotation.

Figure 68 shows that there is a quadratic correlation between the time averaged power requirement and rotation frequency of the tail. For the rotation rate 640 Hz, the power requirement value is validated by data that Berry [11] provided. He states that micro organisms can have rotation rate up to and beyond 1000 Hz which requires power on the order of femto Watts [11].

In Figure 69, the axial length of the helix tail has a first order effect on the time averaged power requirement.

Wavelength of the helical tail and time averaged power requirement are inversely proportional as depicted in Fig. 70.

Time averaged power requirement has a quadratic dependency on maximum amplitude of the helical tail as shown in Fig. 71.
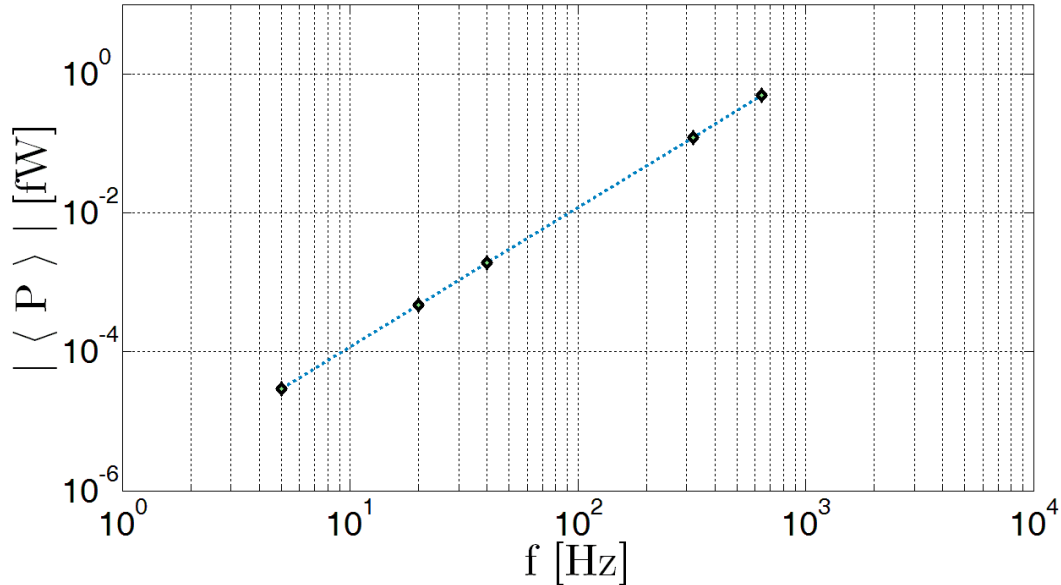
Figure 68: The numeric result for the dependency of time averaged power requirement on the rotation rate of the helical tail.
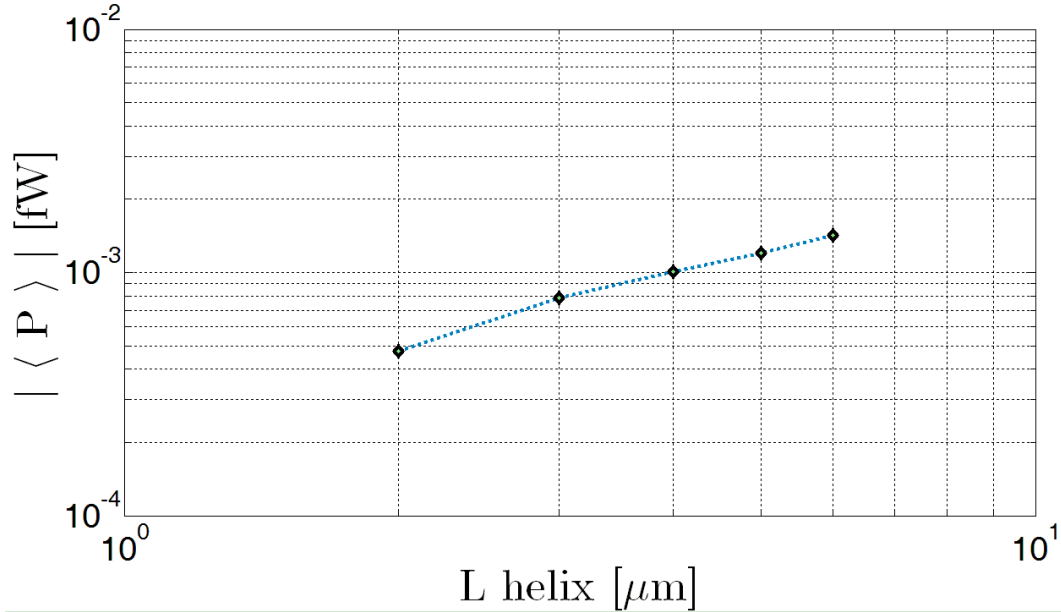
Figure 69: The numeric result for the dependency of time averaged power requirement on the axial length of the helical tail.
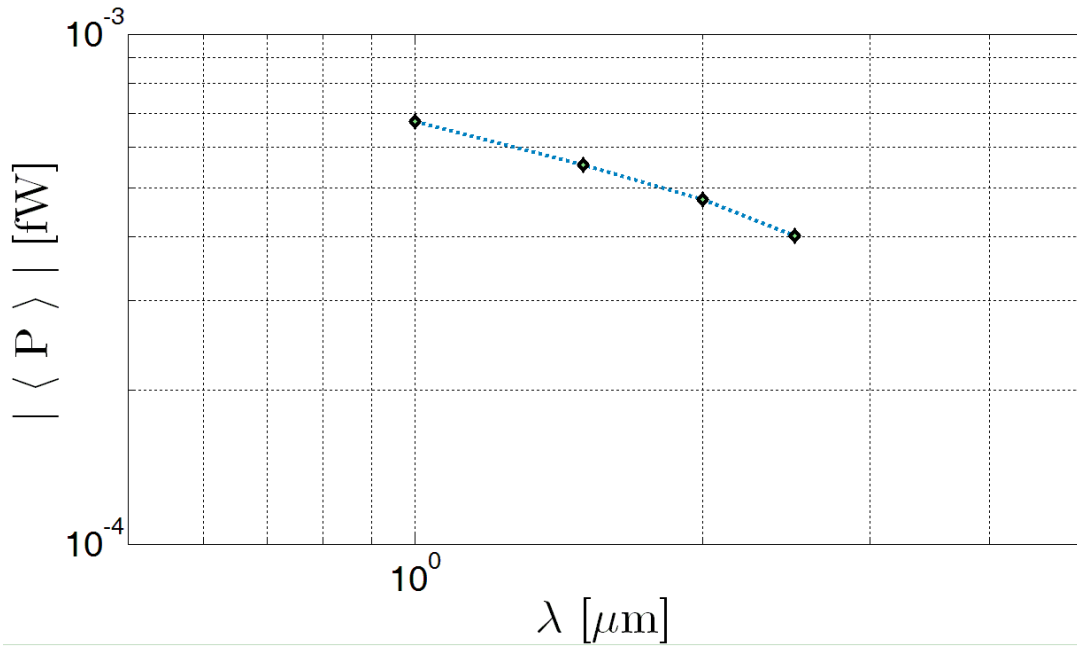
Figure 70: The numeric result for the dependency of time averaged power requirement on the wavelength of the helical tail.
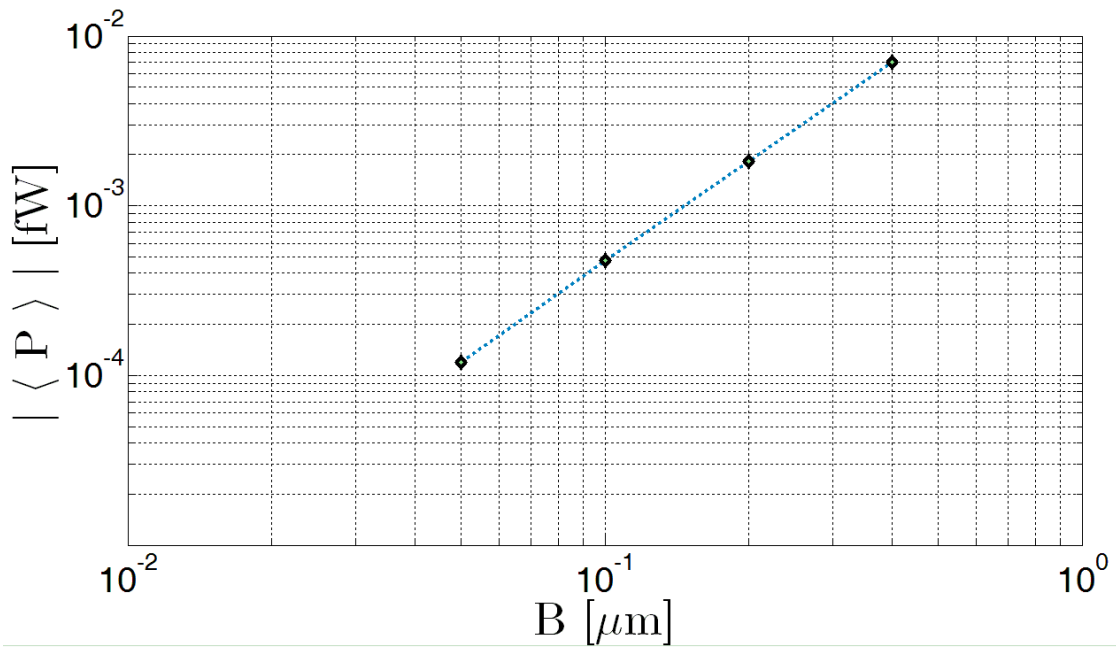
Figure 71: The numeric result for the dependency of time averaged power requirement on the maximum amplitude of the helical tail.

3.3.1.5 Propulsive efficiencies

Figure 72 shows that tail rotation rate does not have any effect on the propulsive efficiencies. Propulsion in longitudinal direction is nearly two times the efficient of propulsion in perpendicular directions to it.
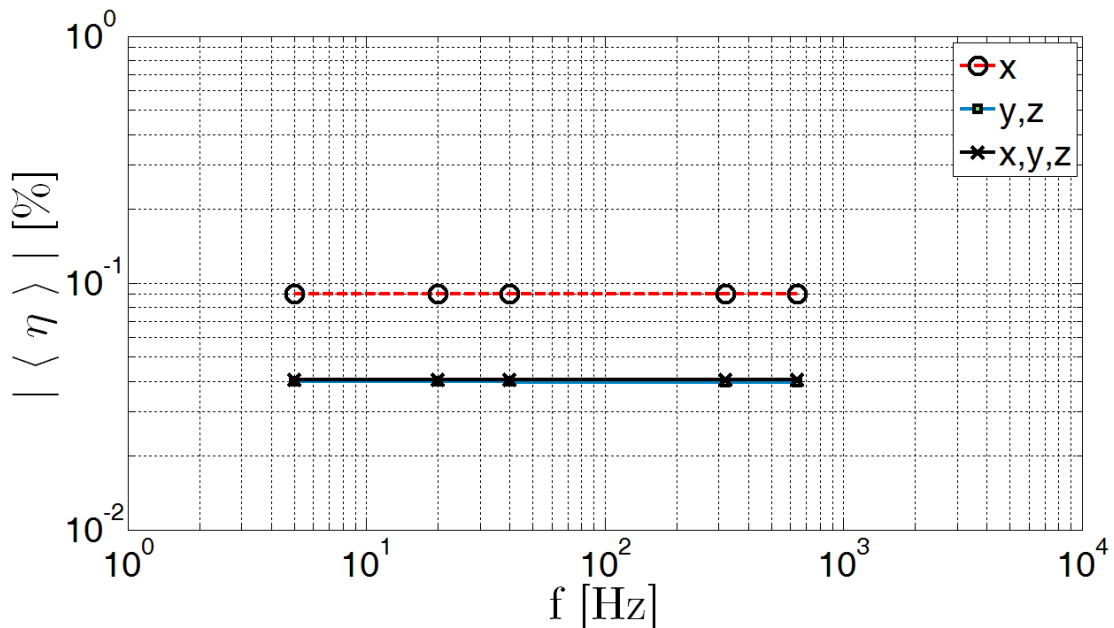
Figure 72: The numeric results for the dependency of time averaged propulsive efficiencies on the rotation rate of the helical tail.

Increasing the helical tail length does not affect propulsive efficiencies very much. Figure 73 shows that the correlation between the propulsive efficiencies and the tail length is even weaker than a linear one. The only remarkable effect can be seen for input length 4 μm of which result is a potential outlier.

According to the plot in Fig. 74, the effect of helical tail wavelength on the propulsive efficiencies has a result which can provide valuable insight for maneuvering the micro swimmer. The total propulsive efficiency in all three directions remains nearly constant for the whole range of wavelength. However, from the figure, it can be inferred that for swimming on a straight line, smaller wavelengths are more efficient but for swimming sideways, higher wavelengths are more efficient.
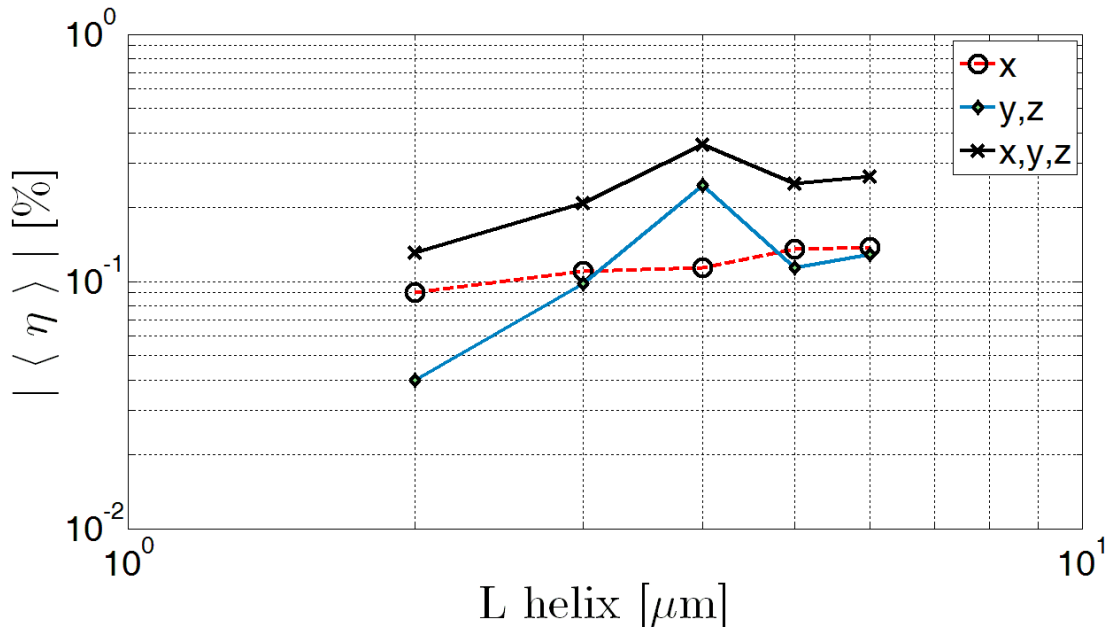
Figure 73: The numeric results for the dependency of time averaged propulsive efficiencies on the axial length of the helical tail.
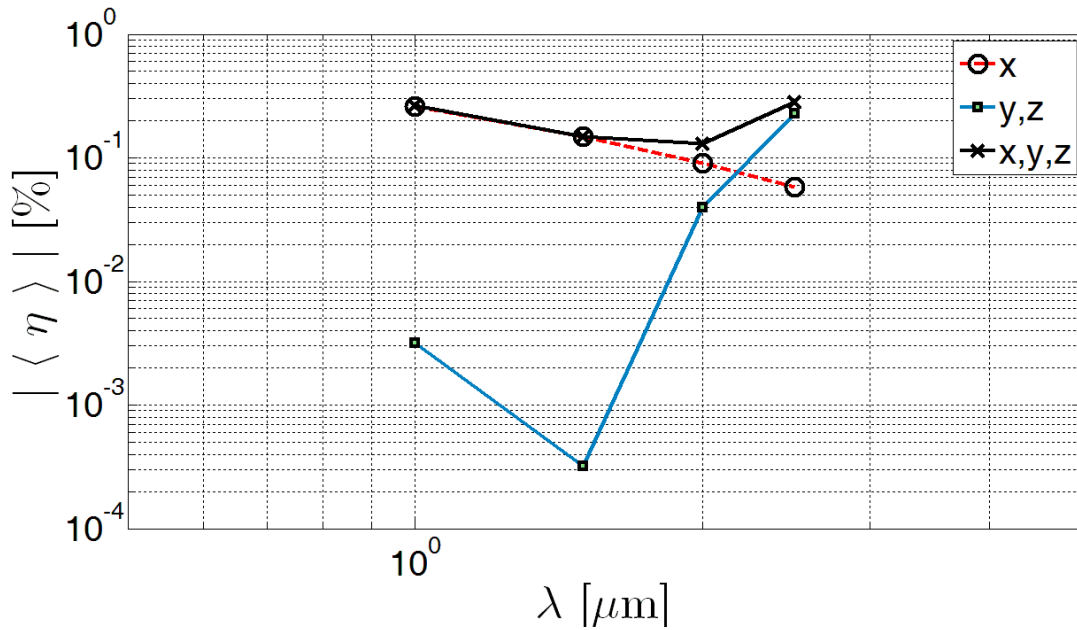
Figure 74: The numeric results for the dependency of time averaged propulsive efficiencies on the wavelength of the helical tail.

Figure 75 demonstrates that the maximum amplitude of helical tail has the strongest effect among all other parameters. There is a clear linear effect of the maximum amplitude of the helical tail on the propulsive efficiency in *x* direction. However, smaller values of

maximum tail amplitude affect the propulsive efficiency in *y-z* directions less than a linear correlation. Only for amplitudes higher than 2 μm, there is a linear correlation between the efficiency in *y-z* direction and maximum tail amplitude.
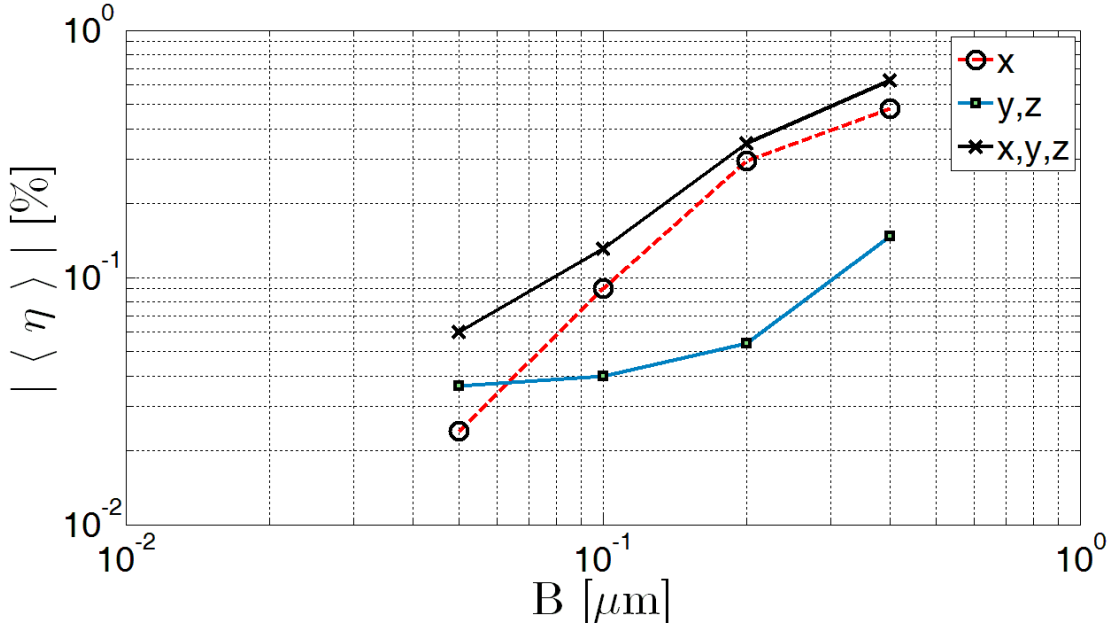
Figure 75: The numeric results for the dependency of time averaged propulsive efficiencies on the maximum amplitude of the helical tail.

3.3.2   The Implications of Parametric Results

The parametric results show give clues about how to maneuver the micro swimmer by manipulating the helical tail parameters:

To swim faster in straight line, the swimmer should definitely have low wavelengths. In a range of wavelengths from 1 to 2.5 μm, the ratio of longitudinal swimming speed to the amplitudes of *v-w* velocities can vary between ~10-0.4 values respectively. Therefore, the domination between *u* and *v-w* duo can be chosen with parameter wavelength. Rotation rate and axial length of the helical tail affect *u* and *v-w* with a linear correlation. Hence, there is no effect of ω_{app} and L_{tl} on the domination between *u* and *v-w*. As the last parameter, maximum helical tail amplitude has a higher order affect on velocity *u* than it has on *v-w*. Therefore, in a range of maximum amplitude from 0.05 to 0.5 μm, the ratio between *u* to *v-w* can vary from 0.5 to 1.25. In order to have a dominating *v-w*, the procedure above can be applied from the

other way around. By having larger displacements in *y-z* axes than in *x* axis, the micro swimmer can get around obstacles without the need of changing its orientation.

If the swimmer needs to change its orientation, it requires larger rotation rates in *y-z* axes by controlling its translational velocity at the same time. In order change the orientation with minimizing the translations, the axial tail length should definitely be decreased. A shorter tail length will decrease all translational velocities by increasing the rotation rates in *y-z* axes at the same time. Moreover, increasing wavelength of the helical tail will decrease *u* which causes net displacement. Even an increasing wavelength will increase the amplitudes of *v-w*, they will not cause any net displacement.

CHAPTER 4

CONCLUSIONS AND FUTURE WORK

In this thesis, a conceptual micro swimmer with a single helical flagella and the bacterium, Vibrio Alginolyticus are successfully simulated and the results are validated by using the analytical and observational data available in the literature. The agreement between simulation results and the observational data of V. Alginolyticus bacterium shows that by the use of commercially available software, COMSOL time-dependent, 3D models governed by Navier-Stokes equations can be solved to obtain results to reflect the reality more than 80%. Moreover, the parametric simulations with relatively low mesh qualities compared to V. Alginolyticus model, can effectively reflect the parametric effect observed in the motion of micro organisms.

The parametric results presented here give a valuable insight for the reinterpretation of 2D observations of the bacterium motion. Moreover, artificial micro swimmer can be designed with correct parameters according to the application to be used while being energy efficient at the same time. When technology can provide helical tails which can deform into any given shape instead of being rigid, the helical tail can reconfigure its geometric properties as well as its rotation rate. This would enable it have the features of micro swimmer with different tail parameter or even features that none of them can ever have.

With the use of a conceptual deformable helical tail, a micro swimmer can change its orientation which is normally done by bacteria with several flagella actuated individually in the "tumble mode.

REFERENCES

[1] Bouge, R., "The development of medical microrobots: a review of progress", *Industrial Robot: An International Journal,* 35(4), pp. 294–299, **2008**.

[2] Behkam, B., Sitti, M., "Design Methodology for Biomimetic Propulsion of Miniature Swimming Robots", *Journal of Dynamic Systems*, Measurement, and Control, 128, pp. 36-43, **2006.**

[3] Becker, L.E., Koehler, S.A., Stone, H.A., "On Self-Propulsion of Micro-Machines at Low Reynolds Number: Purcell's Three Link Swimmer", *J. Fluid Mech.*, 490, pp. 15-35, **2003.**

[4] Goto, T., Masuda, S., Terada, K., Takano, Y., "Comparison between observation and boundary element analysis of bacterium swimming motion," *JSME International Journal Series C*, 44, pp. 958-963, **2001**.

[5] M. Koz, S. Yesilyurt, "Simulations of microflows induced by rotation of spirals in microchannels," *Proc. of SPIE, vol 6886, Microfluidics, BioMEMS, and Medical Microsystems VI*, ed. Wang, Wanjun, Vauchier, Claude, **2008.**

[6] M. Koz, S. Yesilyurt, "Simulation-based analysis of a biologically-inspired micropump with a rotating spiral inside a microchannel," *6th Int. Conf. on Nanochannels, Microchannels and Minichannels*, Darmstadt, Germany, ASME, **2008**.

[7] Laser, D.J., Santiago, J.G., "A Review of Micropumps", *J. Micromech. Microeng.,* 4, pp. R35-R64, **2004.**

[8] Dreyfus, R., Baudry, J., Roper, M.L., Fermigier, M., Stone, H.,A., Bibette, J., "Microscopic Artificial Swimmers", *Nature*, 437(6), pp. 862-864, **2005.**

[9] Berg, H.C., "Navigation on a Micron Scale", *Lect. Notes Phys.*, 711,pp. 1–13, **2007**.

[10] Berg, H.C., "Motile Behavior of Bacteria", *Physics Today*, pp. 24-29, **2000**.

[11] Berry, R.M., "The Bacterial Flagellar Motor", *Forces, Growth and Form in Soft Condensed Matter: At the Interface between Physics and Biology*, pp. 145-164, **2004**.

[12] Lighthill, Sir, J., "Mathematical Biofluiddynamics", *Society for Industrial and Applied Mathematics*, USA, **1975.**

[13] Turner, L., Ryu, W.S., Berg, H.C., "Real-Time Imaging of Fluorescent Flagellar Filaments", *Journal of Bacteriology*, 182 (10), pp. 2793-2801, **2000**.

[14] Chattopadhyay, S., Moldovan, R., Yeung, C., Wu, X. L., "Swimming efficiency of bacterium Escherichia coli", *PNAS*, 103 (37), pp. 13712-13717, **2006**.

[15] Taylor, Sir, G.I., "Analysis of the Swimming of Microscopic Organisms", *Proc. R. Soc. Lond.*, 209(A), pp. 447-461, **1951.**

[16] Hancock, G.J., "The Self-Propulsion of Microscopic Organisms through Liquids", *Proc. R. Soc. Lond., Series A,* 217 (1128), pp. 96-121, **1953**.

[17] Brokaw, C.J., "Flagellar Propulsion" *JEB Classics The Journal of Experimental Biology*, pp. 985-986, **2006**.

[18] Gray, J. and Hancock, G., "The Propulsion of Sea-Urchin Spermatozoa", *Journal of Experimental Biology*, 32, pp. 802-814, **1955.**

[19] Hsu, C.-Y., Dillon, R., "A 3D Motile Rod-Shaped Monotrichous Bacterial Model", *Bulletin of Mathematical Biology*, 71, pp. 1228-1263, **2009**.

[20] Childress, S., "Mechanics of Swimming and Flying", Cannings, C., ed., Hoppensteadt, F., ed., Cambridge Studies in Mathematical Biology:2, Cambridge University Press, New York, **1981.**

[21] Keller, J.B., Rubinow, S.I.,"Swimming of flagellated microorganisms," *Biophysical Journal*, 16, pp. 151-170, **1976**.

[22] Crenshaw, H.C., "A New Look at Locomotion in Microorganisms: Rotating and Translating", *Amer. Zool.*, 36, pp. 608-618, **1996**.

[23] Brennen, C., Winnet, H., "Fluid Mechanics of Propulsion by Cilia and Flagella", *Ann. Rev. Fluid Mech.*, 9, pp. 339-398, **1977.**

[24] Magariyama, Y., Sugiyama, S., Muramoto, K., Kawagishi, I., Imae, Y., Kudo, S., "Simultaneous Measurement of Bacterial Flagellar Rotation Rate and Swimming Speed", *Biophysical Journal*, 69, pp. 2154-2162, **1995**.

[25] Magariyama, Y., Sugiyama, S., Kudo, S., "Bacterial swimming speed and rotation rate of bundled Flagella", *FEMS Microbiology Letters*, 199, pp. 125-129, **2001.**

[26] Chattopadhyay, S., Wu, X.-L., "The effect of Long-Range Hydrodynamic Interaction on the Swimming of a Single Bacterium", *Biophysical Journal*, 96, pp. 2023-2028, **2009**.

[27] Donea, J., Huearta, A., Ponthot, J.-P., Ferran, A.R., "Arbitrary Lagrangian-Eulerian Methods", Encyclopedia of Computational Mechanics Vol. 1: Fundamentals, Stein, E., de Borst, R., Hughes, T.J.R., Ed., John Wiley & Sons, Ltd., **2004.**

[28] Duarte, F., Gormaz, R., Natesan, S., "Arbitrary Lagrangian-Eulerian Method for Navier-Stokes Equations with Moving Boundaries", *Comput. Methods Appl. Mech. Engrg.*, 193, pp. 4819-4836, **2004.**

[29] Baraff, D., "Physically Based Modeling: Rigid Body Simulation", *SIGGRAPH Course Notes,* **2001**.

[30] Spong, M.W., Vidyasagar, M., "Robot Dynamics and Control", *John Wiley & Sons, Inc., USA,* Ch. 2, **1989**.

[31] Goto, T., Nakata, K., Baba, K., Nishimura, M., Magariyama, Y., "A Fluid-Dynamic Interpretation of the Asymmetric Motion of Singly Flagellated Bacteria Swimming Close to a Boundary", *Biophysical Journal*, 89, pp. 3771–3779, **2005**.

[32] COMSOL, A.B., COMSOL Multiphysics User Guide, **2005.**

APPENDIX A

Mass, Volume and Rotational Inertia Calculations

In this work, the micro swimmer volume, mass and rotational inertia matrix is numerically calculated with the commercial software package, COMSOL. Additionally, the principle moments of inertia are analytically calculated for verification.

The volumes of the swimmer head and tail are separately calculated by having COMSOL to take the volume integrals of the deformed shape.

$$V_b = \int_{V=V_b} dV \tag{70}$$

$$V_{tl} = \int_{V=V_{tl}} dV \tag{71}$$

$$V_{sw} = V_b + V_{tl} \tag{72}$$

In order to show the lowest ratio between the masses of body and tail, the volumes are calculated for the set of parameters: m=0.6, B_0=0.4 μm, λ=1 μm and L_{tl}=6 μm.

$$\frac{V_b}{V_{tl}} = \frac{1.046x10^{-18}}{4.656x10^{-20}} = 22.46 \tag{73}$$

For the reference case parameters, m=0.6, B_0=0.1 μm, λ=2 μm and L_{tl}=2 μm the ratio becomes:

$$\frac{V_b}{V_{tl}} = \frac{1.046x10^{-18}}{1.519x10^{-20}} = 68.86 \tag{74}$$

For a case of inertia matrix comparison between the analytic and numeric results, the parametric set m=0.6, B_0=0.4 μm, λ=2 μm and L_{tl}=2 μm are chosen for the microswimmer used in parametric simulations. The result of this comparison will also show the accuracy of the numeric calculations done above.

In the numeric model, the swimmer is drawn with a straight rod instead of a helix as Figure 76. Afterwards, 0.4 μm deformation is specified on the rod boundaries in order to form the helix shape out of the straight rod. As in Eq. 30, displacements in Y and Z directions are

cosines and sine functions respectively. The original and deformed shape of the swimmer is depicted in Figures 76,77 and 78.
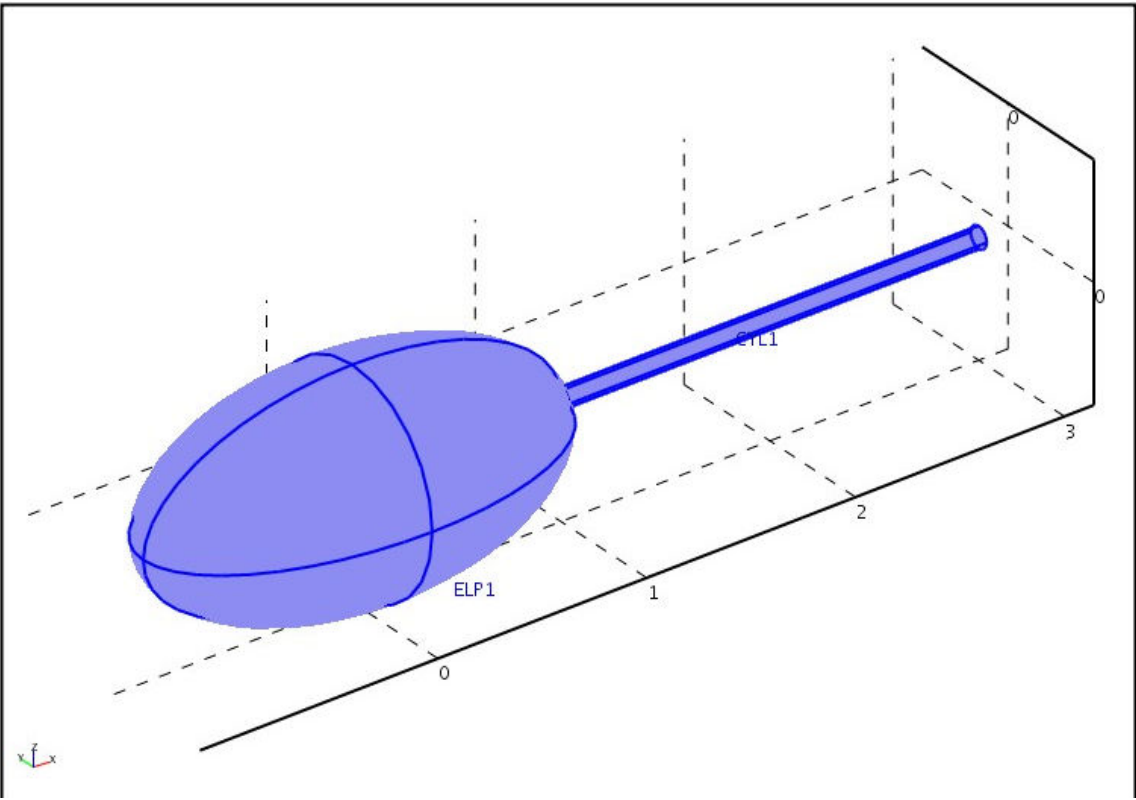
Figure 76: The initial drawing of the micro swimmer without any displacement induced on the straight rod tail.

Figures 77 and 78 are showing the tail deformations on the *XY* and *XZ* planes. The cosine displacement function on the *XY* and the sine displacement on the *XZ* planes are verified with the correct amplitude and wavelength. The elliptical body shape is kept with the correct dimensions. There is a smooth geometric transition between the body and tail with the help of *B(X)* function. The superposition of the displacements in two planes gives the 3D helix shape.
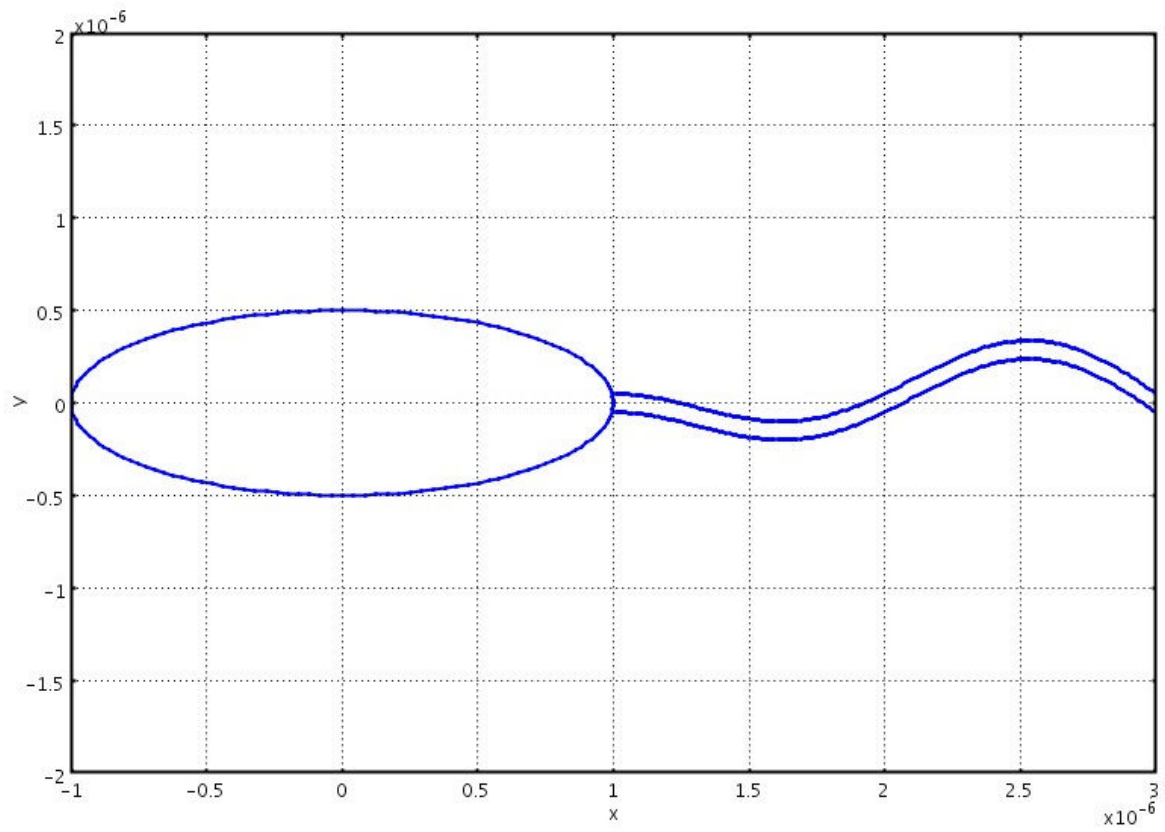
Figure 77: The deformed straight rod in to a helix in the *XY* plane.
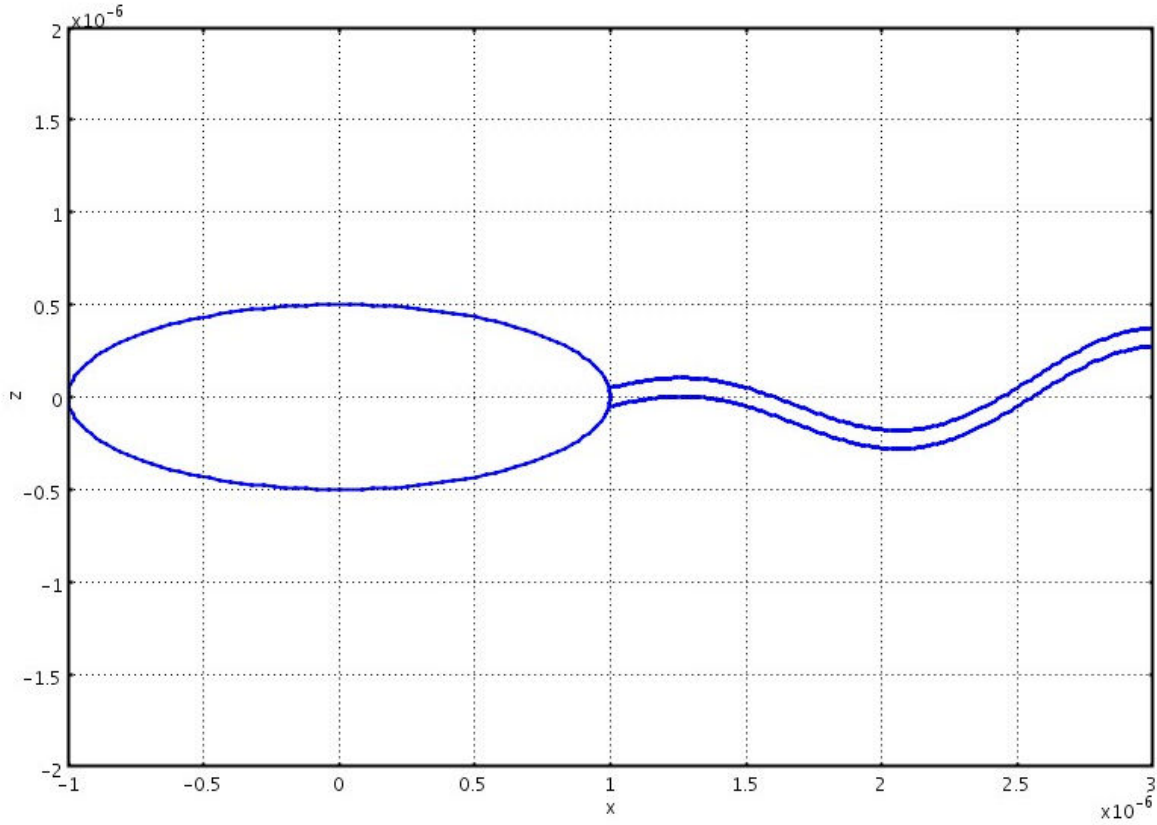
Figure 78: The deformed straight rod into a helix in the *XZ* plane.

According to the positions given in the deformed shape plot above, full rotational inertia matrix of the swimmer expressed in body frame is obtained by having COMSOL to take the numeric integrals given below:

$$
J = \rho \begin{bmatrix} \int (Y^2 + Z^2)dV & -\int XYdV & -\int XZdV \\ -\int XYdV & \int (X^2 + Z^2)dV & -\int YZdV \\ -\int XZdV & -\int YZdV & \int (Y^2 + Z^2)dV \end{bmatrix}
\tag{75}
$$

The results of the integrals give the full rotational inertia matrix of the micro swimmer which is expressed in body frame.

$$
J_{sw,numeric} = \begin{bmatrix} 1.05x10^{-28} & -2.43x10^{-30} & -8.38x10^{-32} \\ -2.43x10^{-30} & 3.27x10^{-28} & -6.36x10^{-32} \\ -8.38x10^{-32} & -6.36x10^{-32} & 3.27x10^{-28} \end{bmatrix} \text{kg.m}^2
\tag{76}
$$

When the rotational inertia matrix is decomposed for the tail and body, their partial effect on the whole swimmer inertia matrix can be calculated.

$$J_{tl,numeric} = \begin{bmatrix} 7.83x10^{-31} & -2.43x10^{-30} & -8.38x10^{-32} \\ -2.43x10^{-30} & 6.59x10^{-29} & -6.36x10^{-32} \\ -8.38x10^{-32} & -6.36x10^{-32} & 6.59x10^{-29} \end{bmatrix} kg.m^2 \tag{77}$$

Due to the fact that the principle moments of inertias dominate the products of inertia by a factor of 10^6 in the J_b, the off diagonal elements are assumed to be zero.

$$\begin{aligned} J_{b,numeric} &= \begin{bmatrix} 1.04x10^{-28} & -6x10^{-34} & 6.74x10^{-39} \\ -6x10^{-34} & 2.61x10^{-28} & 9.39x10^{-37} \\ 6.74x10^{-39} & 9.39x10^{-37} & 2.61x10^{-28} \end{bmatrix} \\ &\cong \begin{bmatrix} 1.04x10^{-28} & 0 & 0 \\ 0 & 2.61x10^{-28} & 0 \\ 0 & 0 & 2.61x10^{-28} \end{bmatrix} kg.m^2 \end{aligned} \tag{78}$$

The partial effect of each element from each inertia matrix is calculated in the following equations.

$$J_{tl/sw}(a,b) = \frac{J_{tl,numeric}(a,b)}{J_{sw,numeric}(a,b)} = \begin{bmatrix} \%0.745 & \%100 & \%100 \\ \%100 & \%20.1 & \%100 \\ \%100 & \%100 & \%20.1 \end{bmatrix} \tag{79}$$

$$J_{b/sw}(a,b) = \frac{J_{b,numeric}(a,b)}{J_{sw,numeric}(a,b)} = \begin{bmatrix} \%99.25 & \%0 & \%0 \\ \%0 & \%79.9 & \%0 \\ \%0 & \%0 & \%79.9 \end{bmatrix} \tag{80}$$

In order to verify the numerical values of the $J_{sw,numeric}$ matrix, tail and body rotational inertias are separately calculated with analytic approaches. The rotational inertia matrix of an ellipsoid body can be analytically calculated with parameters of mass density and dimensions of the ellipsoid. Hence, the analytically calculated rotational inertia matrix for the ellipsoid body is formulated as:

$$M_b = \rho V_b = \rho \frac{4}{3} \pi L_b R_b^2 \tag{81}$$

$$J_{b,analytic} = M_b \begin{bmatrix} 2R_b^2 \big/ 5 & 0 & 0 \\ 0 & (L_b^2 + R_b^2) \big/ 5 & 0 \\ 0 & 0 & (L_b^2 + R_b^2) \big/ 5 \end{bmatrix} \tag{82}$$

The correlation between the analytic and numeric values is 100%.

$$J_{b,analytic} = \begin{bmatrix} 1.0472x10^{-28} & 0 & 0 \\ 0 & 2.6180x10^{-28} & 0 \\ 0 & 0 & 2.6180x10^{-28} \end{bmatrix} \text{kg.m}^2 \tag{83}$$

$$J_{b,accuracy} = \frac{J_{b,numeric}(a,b)}{J_{b,analytic}(a,b)} = \begin{bmatrix} \%100 & \%100 & \%100 \\ \%100 & \%100 & \%100 \\ \%100 & \%100 & \%100 \end{bmatrix} \tag{84}$$

Analytic calculation of helix rotational inertia matrix is done by firstly modifying the previous time dependent helix tail position equation (Eq. 34) in to stationary one:

$$\mathbf{X}_{tl} = \begin{bmatrix} X \\ r_{tl} \dfrac{Y_{tl}}{\left(Y_{tl,srf}^2 + Z_{tl,srf}^2\right)} + B(X)\cos(-\dfrac{2\pi(X - X_{tl,st})}{\lambda}) \\ r_{tl} \dfrac{Z_{tl}}{\left(Y_{tl,srf}^2 + Z_{tl,srf}^2\right)} + B(X)\sin(-\dfrac{2\pi(X - X_{tl,st})}{\lambda}) \end{bmatrix} \tag{85}$$

The mass of an infinitesimal volume is in cylindrical coordinates:

$$dm = \rho dV = \rho ds dA = \rho ds r dr d\phi \tag{86}$$

Where ds is the infinitesimal length of the helix:

$$s = \sqrt{B^2 + \left(\frac{\lambda}{2\pi}\right)^2} \left(\frac{2\pi X}{\lambda}\right) \Rightarrow ds = \sqrt{B^2 + \left(\frac{\lambda}{2\pi}\right)^2} \left(\frac{2\pi dX}{\lambda}\right) \tag{87}$$

In the rotational inertia matrix, the integrals to be taken are:

$$J_2(1,1) = \rho \int_{X=X_{tl,st}}^{X_{tl,end}} \int_{r=0}^{R_{tl}} \int_{\phi=0}^{2\pi} (Y^2 + Z^2)\sqrt{B^2 + \left(\frac{\lambda}{2\pi}\right)^2} \left(\frac{2\pi}{\lambda}\right) r\, dX dr d\phi \tag{88}$$

$$J_2(2,2) = \rho \int_{X=X_{tl,st}}^{X_{tl,end}} \int_{r=0}^{R_{tl}} \int_{\phi=0}^{2\pi} (X^2 + Z^2)\sqrt{B^2 + \left(\frac{\lambda}{2\pi}\right)^2} \left(\frac{2\pi}{\lambda}\right) r\, dX dr d\phi \tag{89}$$

$$J_2(3,3) = \rho \int_{X=X_{tl,st}}^{X_{tl,end}} \int_{r=0}^{R_{tl}} \int_{\phi=0}^{2\pi} (X^2 + Y^2)\sqrt{B^2 + \left(\frac{\lambda}{2\pi}\right)^2} \left(\frac{2\pi}{\lambda}\right) r\, dX dr d\phi \tag{90}$$

When the terms above are integrated with the symbolic toolbox of MATLAB, the resulting $J_{tl,analytic}$ matrix below is obtained. Following this analytically calculated matrix, the accuracy percentages of the numerically calculated principle moment of inertia are given and assumed to be the same for the off diagonal elements.

$$J_{tl,analytic} = \begin{bmatrix} 1.2852 \times 10^{-30} & & \\ & 1.0995 \times 10^{-28} & \\ & & 1.0995 \times 10^{-28} \end{bmatrix} kg.m^2 \tag{91}$$

$$J_{tl,accuracy} = \frac{J_{tl,numeric}(a,b)}{J_{tl,analytic}(a,b)} = \begin{bmatrix} \%60 & & \\ & \%60 & \\ & & \%60 \end{bmatrix} \cong \begin{bmatrix} \%60 & \%60 & \%60 \\ \%60 & \%60 & \%60 \\ \%60 & \%60 & \%60 \end{bmatrix} \tag{92}$$

Therefore, the total accuracy for the whole swimmer is calculated as below:

$$J_{sw,accuracy}(a,b) = J_{b/sw}(a,b)J_{b,accuracy}(a,b) + J_{tl/sw}(a,b)J_{tl,accuracy}(a,b) \tag{93}$$

$$J_{sw,accuracy} = \begin{bmatrix} \%99.25 + (\%0.745)(\%60) & (\%100)(\%60) & (\%100)(\%60) \\ (\%100)(\%60) & \%79.9 + (\%20.1)(\%60) & (\%100)(\%60) \\ (\%100)(\%60) & (\%100)(\%60) & \%79.9 + (\%20.1)(\%60) \end{bmatrix} \tag{94}$$

$$J_{sw,accuracy} = \begin{bmatrix} \%99.697 & \%60 & \%60 \\ \%60 & \%91.96 & \%60 \\ \%60 & \%60 & \%91.96 \end{bmatrix} \tag{95}$$

The accuracy matrix shows that COMSOL is calculating the diagonal elements with at least 91.96% accuracy. The 60% accuracy for the off diagonal matrix is tolerable for rotational acceleration calculations while diagonal elements are dominating the off diagonal ones with at least a factor of 50.

According to the numeric techniques explained above, the following inertia matrices are obtained in kg.m^2 unit. $J_{b,X}$ is constant: 1.0472×10^{-28} kg.m^2.

J	B=0.05μm		
L=2μm	1.047239e-28	-3.049317e-31	-1.332495e-32
C=2μm	-3.049317e-31	3.297453e-28	-1.018985e-33
m=0.6	-1.332495e-32	-1.018985e-33	3.297453e-28
J	B=0.1μm		
L=2μm	1.047598e-28	-6.09263e-31	-2.33987e-32
C=2μm	-6.09263e-31	3.29764e-28	-4.022387e-33
m=0.6	-2.33987e-32	-4.022387e-33	3.29764e-28
	B=0.2μm		
L=2μm	1.049033e-28	-1.217925e-30	-4.354644e-32
C=2μm	-1.217925e-30	3.298389e-28	-1.597962e-32
m=0.6	-4.354644e-32	-1.597962e-32	3.298389e-28
J	B=0.4μm		
L=2μm	1.054769e-28	-2.43525e-30	-8.384175e-32
C=2μm	-2.43525e-30	3.301385e-28	-6.369581e-32
m=0.6	-8.384175e-32	-6.369581e-32	3.301385e-28

Table 7: Inertia matrix of the micro swimmer for varying tail amplitudes

J	λ=1μm		
L=2μm	1.047598e-28	-2.811706e-31	-4.707794e-33
B=0.1μm	-2.811706e-31	3.297639e-28	-1.90193e-33
m=0.6	-4.707794e-33	-1.90193e-33	3.297639e-28
J	λ =1.5μm		
L=2μm	1.047598e-28	+2.521504e-31	-3.228815e-31
B=0.1μm	+2.521504e-31	3.297611e-28	+1.229002e-33
m=0.6	-3.228815e-31	+1.229002e-33	3.297611e-28
	λ =2μm		
L=2μm	1.047598e-28	-6.09263e-31	-2.33987e-32
B=0.1μm	-6.09263e-31	3.29764e-28	-4.022387e-33
m=0.6	-2.33987e-32	-4.022387e-33	3.29764e-28
	λ =2.5μm		
L=2μm	1.047597e-28	-4.056836e-31	+7.75117e-31
B=0.1μm	-4.056836e-31	3.297603e-28	+3.46288e-33
m=0.6	+7.75117e-31	+3.46288e-33	3.297603e-28

Table 8: Inertia matrix of the micro swimmer for varying tail wavelengths

J	L_{tl}=2μm		
C=2μm	1.047598e-28	-6.09263e-31	-2.33987e-32

B=0.1μm	-6.09263e-31	3.29764e-28	-4.022387e-33
m=0.6	-2.33987e-32	-4.022387e-33	3.29764e-28
J	L_{tl} =4μm		
C=2μm	1.048174e-28	-9.156947e-31	1.385077e-32
B=0.1μm	-9.156947e-31	5.612479e-28	-3.814492e-33
m=0.6	1.385077e-32	-3.814492e-33	5.612455e-28
	L_{tl} =6μm		
C=2μm	1.048973e-28	-1.414487e-30	-6.928955e-32
B=0.1μm	-1.414487e-30	1.146596e-27	-4.090441e-33
m=0.6	-6.928955e-32	-4.090441e-33	1.146593e-27

Table 9: Inertia matrix of the micro swimmer for varying tail lengths

J_{tl}			B=0.05μm	B=0.1μm	B=0.2μm	B=0.4μm
L=2μm	C=2μm	m=0.6	3.1995e-032	6.9182e-032	2.1793e-031	8.1293e-031
J_{tl}			C=1μm	C=1.5μm	C=2μm	C=2.5μm
L=2μm	B=0.1μm	m=0.6	6.9181e-032	6.9182e-032	6.9182e-032	6.9182e-032
J_{tl}			L=2μm	L=4μm	L=6μm	
C=2μm	B=0.1μm	m=0.6	6.9182e-032	1.249181e-31	2.047281e-31	

Table 10: Inertia values of the helical tail around axis X for varying parameters.

APPENDIX B

Forces in ALE vs Reference Frame

Comsol introduces two frame options for its models which are called reference frame (ref) and Arbitrary-Lagrangian Eulerian frame (ale). They can be used at the same time only for models with deforming meshes. COMSOL assigns (x,y,z) axis names to ale frame and (X,Y,Z) to ref frame. For a non-deforming mesh, only ref frame is used. In order to use these frames properly, their difference in terms of coordinate assignment, stress tensor calculation and depending on the former two differences, the moment calculation difference.

To find out the differences in those areas mentioned above, a test model is generated. In this model, there is fluid flow inside a channel which encapsulates a rectangular solid. This rectangle is fixed from its right edge and the rest of this object deforms in y axis with a sinusoidal motion of 0.05 meters. On all walls of the deforming rectangle and on the top-bottom walls of the channel no-slip boundary conditions are specified. The right edge of the

channel is the inlet with a velocity of 1 m/s and the left edge of the channel is an open boundary with zero pressure.
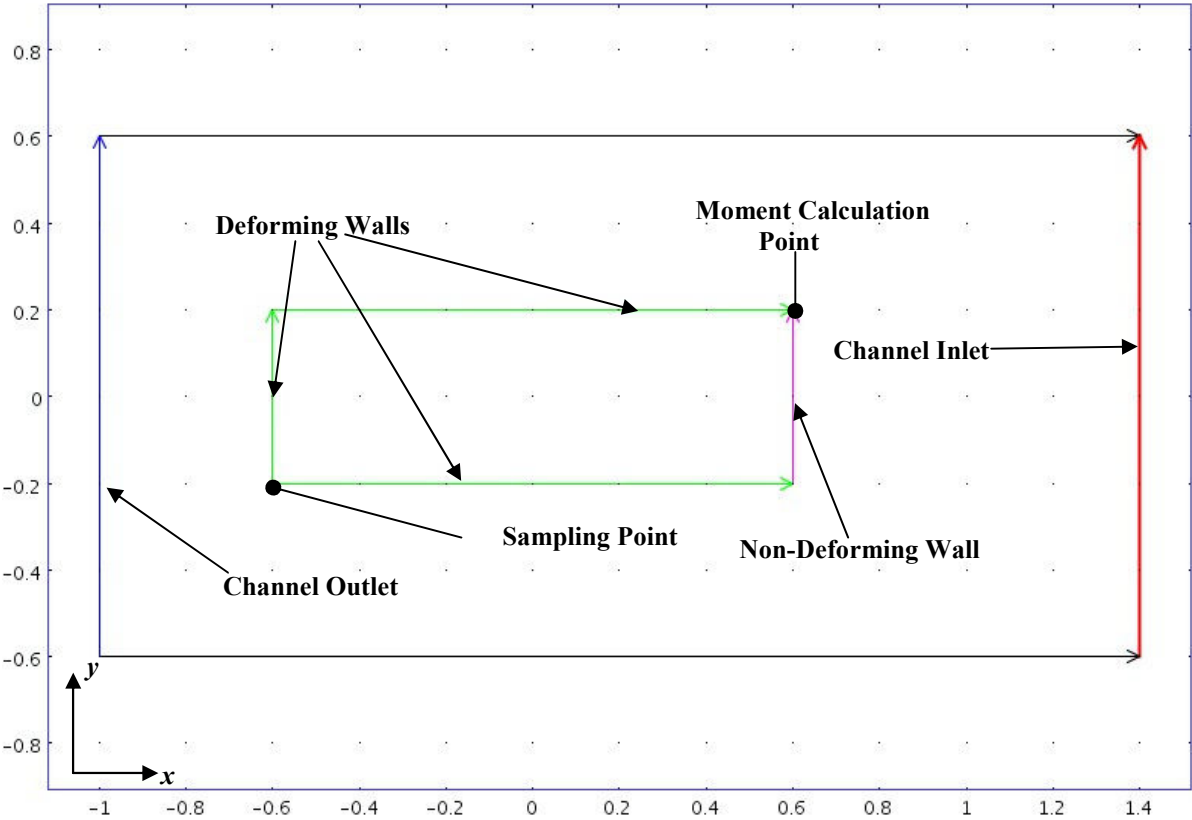
Figure 79: The definition of boundary edges and points in the model.

The time dependent deformation of the rectangle is constraint by channel walls and depicted in the figure below. Moreover, the pressure distribution is presented with varying color on the channel surface. From red to blue, the pressure is decreasing. All colored areas have pressure values at least zero. The white areas at the left of the channel have pressure values smaller than zero.
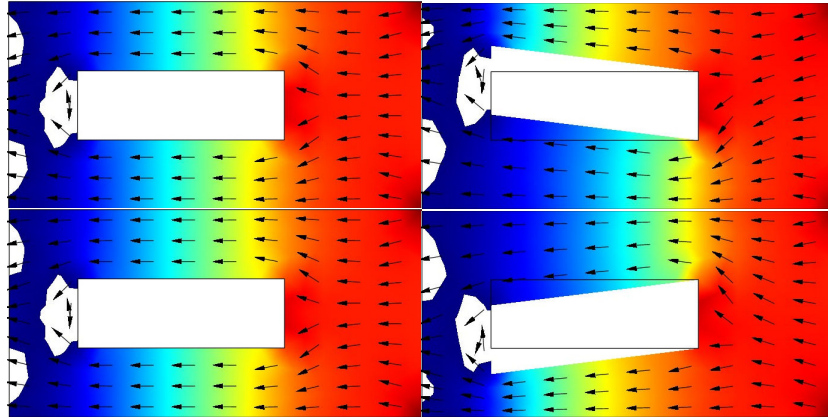
Figure 80: The pressure distribution and solid deformation in the channel.

In order to find out the difference between the coordinate assignments, the *y* axis position (*y* and *Y*) of the "coordinate sampling point" is plotted with respect to two different frames. This plot shows that the reference frame outputs a constant position coordinate which is the same with the initial condition. Contrary to reference frame, the ale frame outputs the instantaneous position of the sampling point.
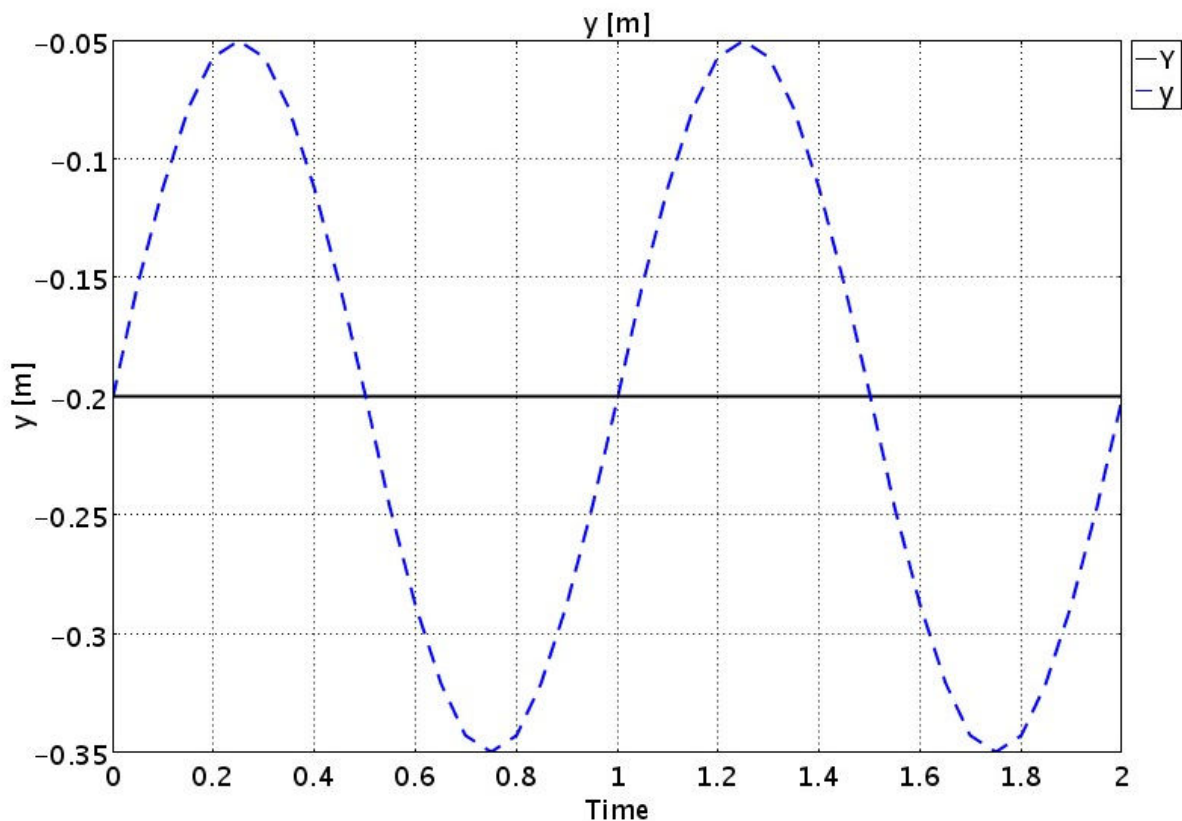
Figure 81: The time dependent positions coordinates in expressed in ALE and reference frame.

For the demonstrating the difference between the calculations of stress tensors, they are plotted on the sampling point and compared with different frame settings. For the fact that there is positive pressure on the sampling point and the pressure on the bottom horizontal deforming edge is higher than the pressure on the right vertical edge, it is expected that the fluid will force the sampling point to the $+y$ and $-x$ direction. However, for the fact that the stress tensors are the reaction forces applied by the solid to fluid, the signs of the forces are expected to be the opposite which are $-y$ and $+x$.

Firstly, stress tensors in reference frame are plotted. There are two stress tensor variables used for x and y axes. The corresponding variable names are T_X_chns and T_Y_chns. They are plotted in the same figure below. The plot shows that despite of having a displacement in the y axis, there is no change in the values with respect to time. This stems from the reference frame choice which calculates the stress tensors according to the initial condition of the mesh. Therefore, because of not having any deformation, there is no change in the stress tensors.

Secondly, stress tensors in the ale frame are plotted. Their names are differentiated from the ones in the reference frame with a capital to small letter transformation. The variables T_x_chns and T_y_chns are plotted together below. There is a clear dependence of the output values on time and so on the sinusoidal deformation magnitude. This shows that the stress tensors calculated in the ale frame reflects the interaction between the fluid and deformed geometric shape.
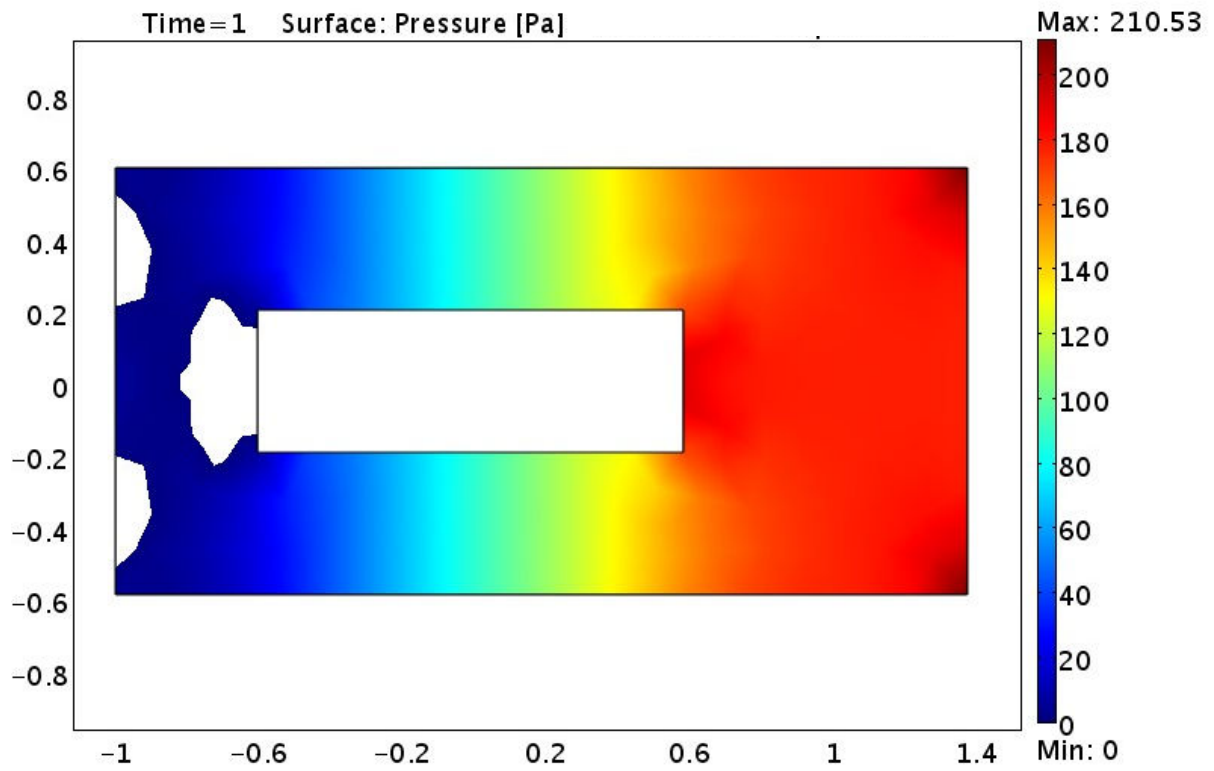
Figure 82: A close up look to the pressure distribution in the channel.
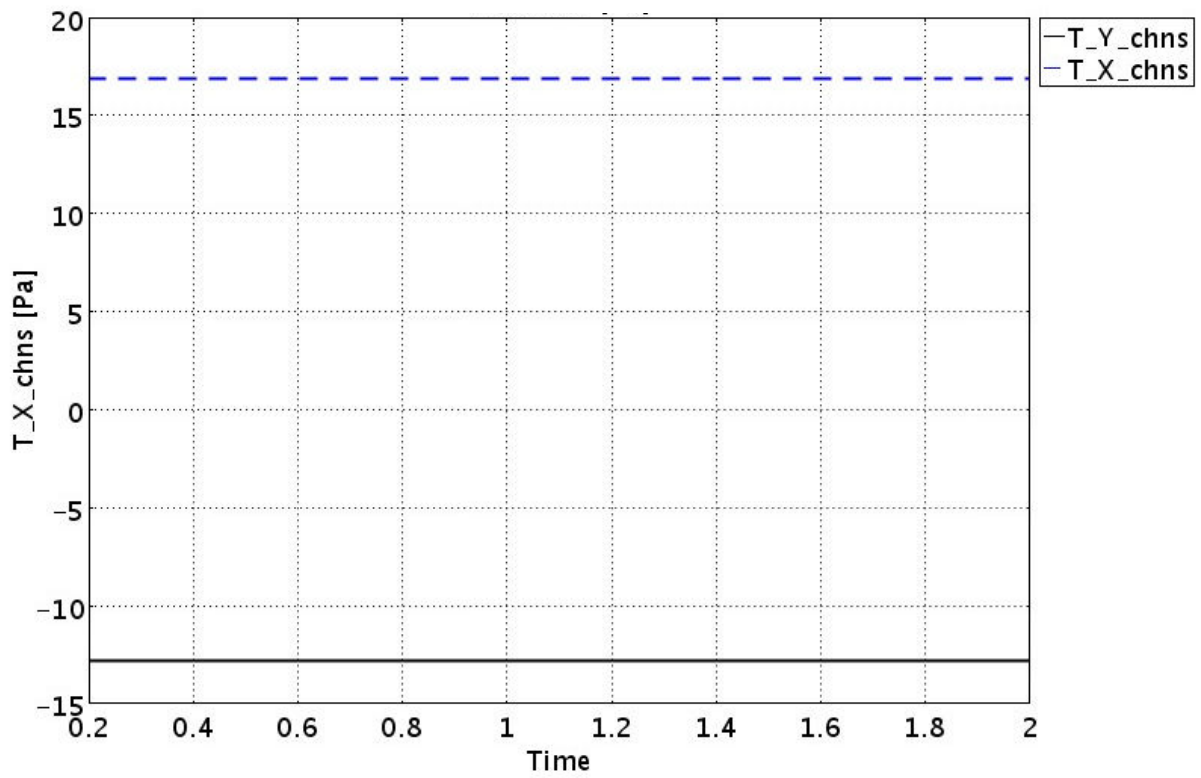
Figure 83: The unaffected stress tensors expressed in reference frame.
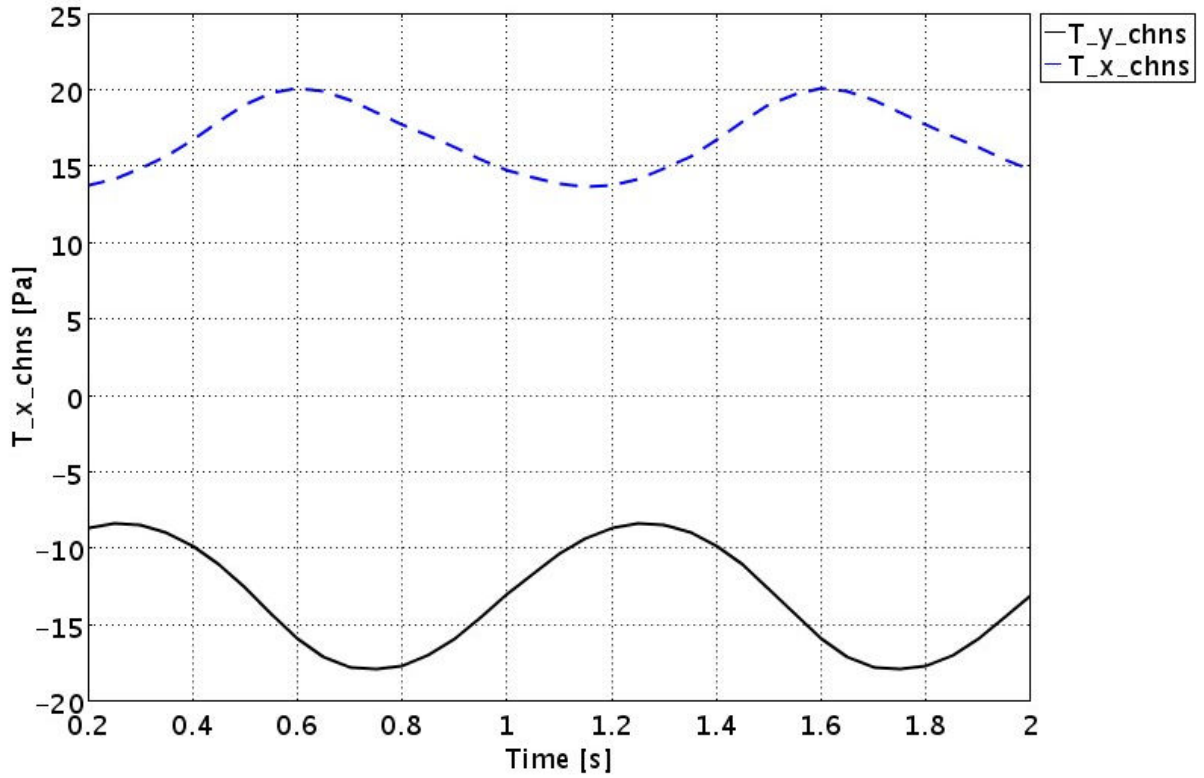
Figure 84: The deformation dependent stress tensors expressed in ALE frame.

By using the facts above, the difference of moment calculation will be presented. In the same model, the z-moment created by the top horizontal deforming wall will be calculated at the "moment calculation point" which in pointed in the figure above. Therefore, there are will be two integrals to be taken on the top horizontal deforming edge:

$$Torque\_Z\_ref = \int\limits_{x=x_{edge}} \left[(X - 0.6)T\_Y\_chns - (Y - 0.2)T\_X\_chns \right] dx \qquad (96)$$

$$Torque\_z\_ale = \int\limits_{x=x_{edge}} \left[(x - 0.6)T\_y\_chns - (y - 0.2)T\_x\_chns \right] dx \qquad (97)$$

After the integrals are taken numerically by COMSOL, the results are plotted below. Such as in the position coordinate and stress tensors calculations, the moment calculated in the reference frame is not time dependent. Contrary to the moment calculated in the reference frame, the one in the ale frame clearly reflects the displacement in the *y* axis.

120
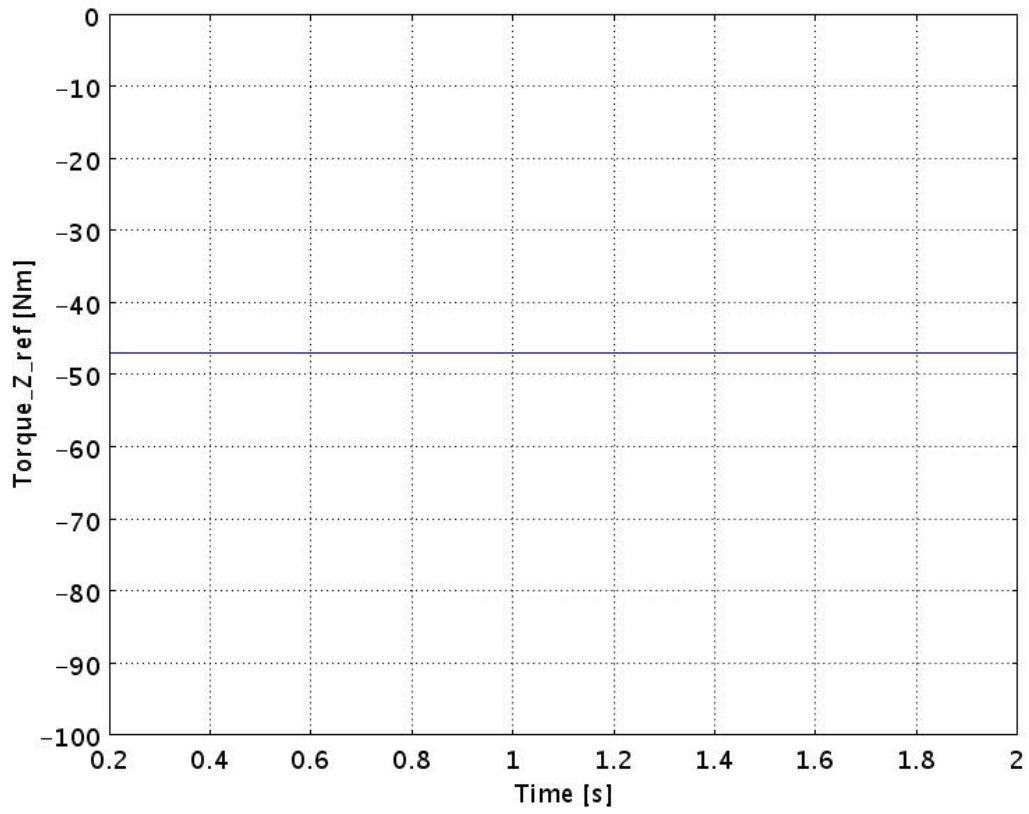
Figure 85: The unaffected *Z* moment expressed in reference frame.
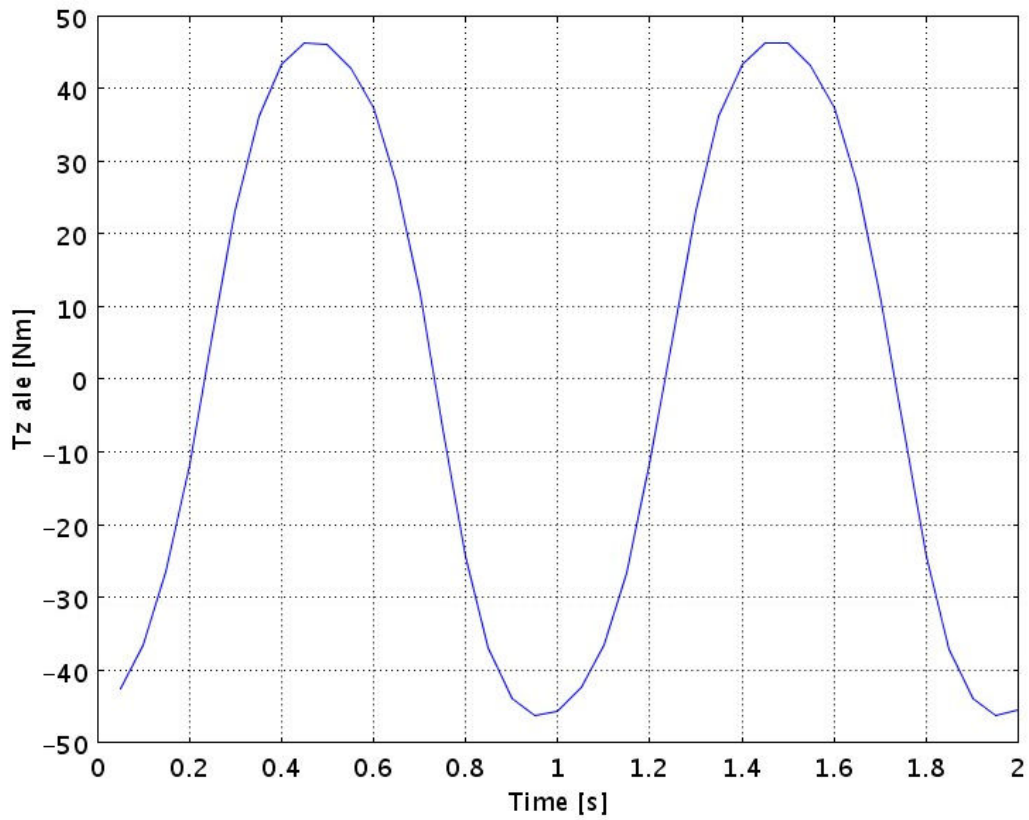
Figure 86: The deformation dependent *z* moment expressed in ALE frame.

121

APPENDIX C

Boundary Velocities in ALE and Reference Frames

The following model has the purpose of showing how the boundary velocity settings are working for a deformed surface. There were two possibilities to consider. On the one hand, COMSOL could specify a different local frame to each mesh node on a boundary. Therefore, as the mesh is deformed, the preset boundary velocities are re-interpreted by COMSOL and reapplied to each point according to their current local frame orientation. On the other hand, COMSOL could use only one frame for all boundaries and the mesh deformations do not affect the boundary velocities which keep their validity for the non-moving frame.

In order to answer the question above, a square is drawn to be deformed with a sinusoidal pattern as it is compressed and released from the center points of the top and bottom edges into its center. This leads a change of orientation for the top and bottom edges. Both edges are initially perpendicular to y axis. The top edge is specified with sliding wall boundary condition with a velocity, 0.002 m/s. The bottom edge is specified with a moving wall boundary condition with a velocity in the x direction, u=0.002 m/s.

The top and bottom channel walls are specified with open boundary conditions and the side walls of the channel and of the square at the center are specified with no slip boundary conditions.
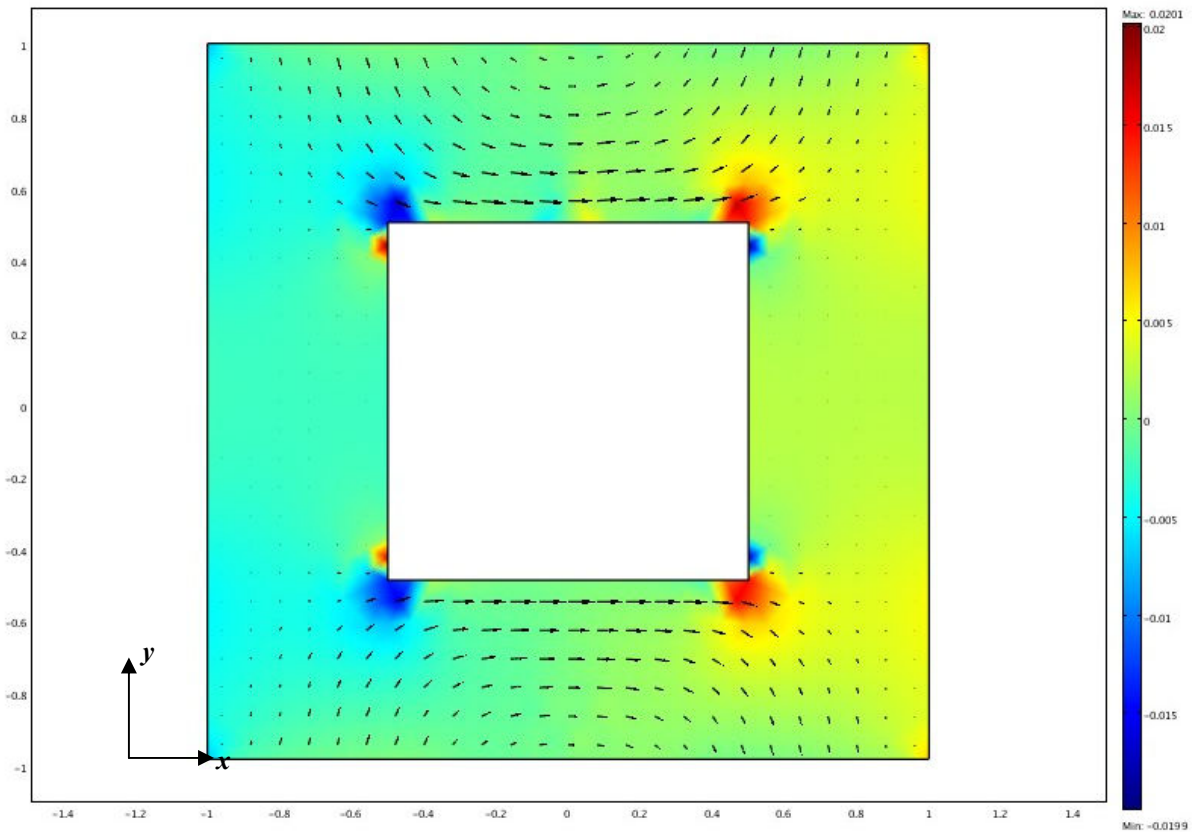
Figure 87: The original shape of the geometry and the initial flow field.

As in the Figures above and below, while there are no deformations, the fluid velocity vectors are tangent to both edges and parallel to each other. However, the deformed shape shows two different fluid velocity patterns. On the one hand, the top edge with the sliding wall boundary condition, keeps the tangential velocity vectors according to the current mesh deformation. On the other hand, the fluid velocity vectors on the bottom edge are directed in the x axis of the non-moving frame.
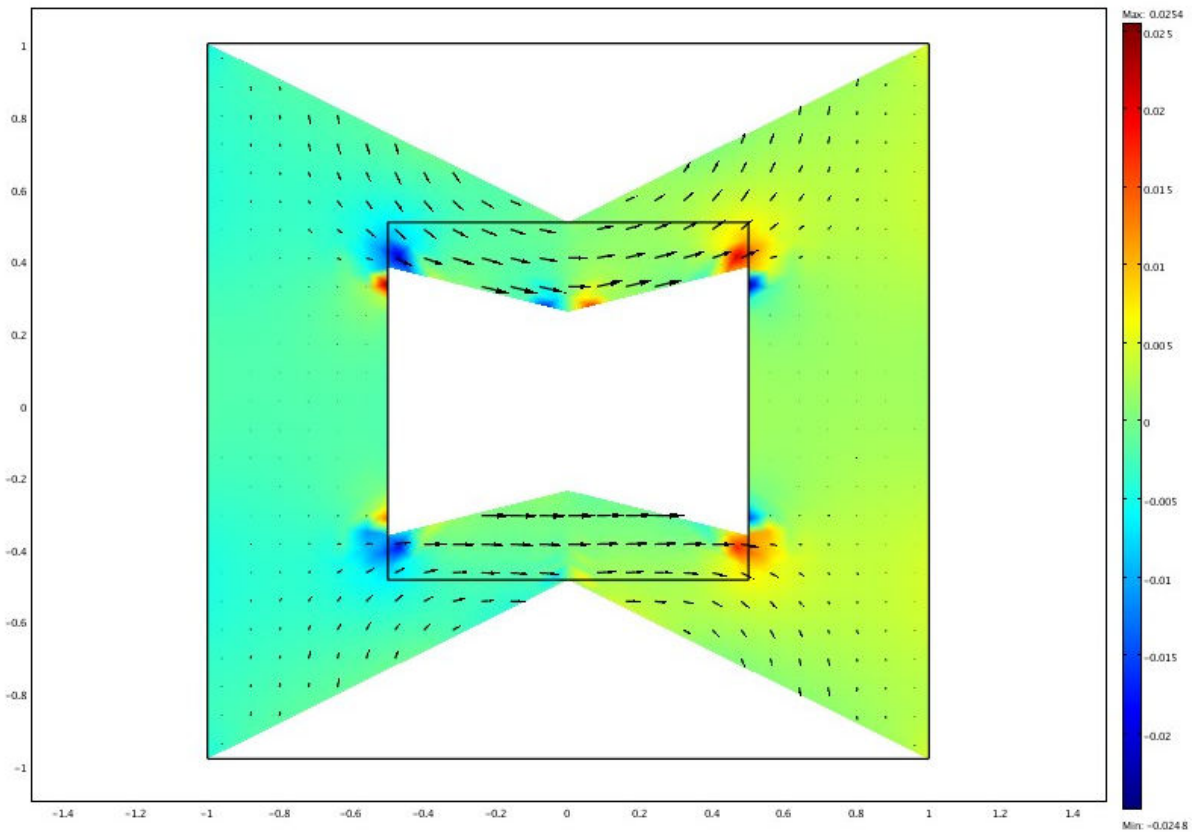
Figure 88: The deformed shape of the geometry and the differences in flow fields.

This test shows that velocities tangential to the deformed mesh surfaces can be specified with sliding wall boundary conditions. However, for the case of a microswimmer, which is the target of this work, there is also a need of specifying velocities perpendicular to deformed mesh surfaces. Another result of this test shows that the boundary velocity settings in Comsol are only valid for the non-moving or in other words, non-deforming frame. Therefore, in order to specify boundary velocities with respect to moving frames, there is a need for a transformation matrix which will map the boundary velocities in the moving frame to the non-moving frame.